

Understanding the relationship between nanoparticles and bacterial group behavior: autolysis and quorum sensing

Submitted in partial fulfillment of the requirements for the degree of

Doctor of Philosophy

in

Civil & Environmental Engineering

Eric McGivney

B.S., Civil & Environmental Engineering, University of Delaware

M.S., Environmental Engineering & Sustainable Infrastructure, KTH Royal Institute of
Technology

Carnegie Mellon University • Pittsburgh, PA

December, 2017

© Eric McGivney, 2018

All Rights Reserved

Acknowledgments

I'm grateful to so many people for helping me complete this project. The ideas and concepts presented here are the product of thousands of hours spent brainstorming, discussing, and arguing with some of the smartest people I've ever met. I could not have done this alone.

Foremost, I thank my advisors, Kelvin Gregory and Jeanne VanBriesen, whose advising techniques are diametrically opposed but equally insightful. I thank them for giving me the freedom and encouragement to explore science that I (sometimes alone) found interesting. In addition to their co-advising roles, they have both been important mentors to me. I came to them several times for life advice, and always left their office with a better perspective.

Greg Lowry was not my official advisor, but he was kind enough to let me work extensively within his group. Listening to Greg's enthusiastic discussions at his weekly meetings has been an incomparable educational experience. He's a unique thinker and his passion for science is contagious. I will miss our Maotai-fueled golf outings.

I also thank Aaron Mitchell who served a valuable role on my proposal and defense committee. As the lone non-Environmental Engineer, Aaron provided insight that often made me reconsider the angle at which I was viewing my research. His feedback significantly improved my research questions and interpretation of results.

The foundational research presented in this dissertation began before I arrived at Carnegie Mellon University in 2013. The previous work of former CMU student, Linchen Han, was instrumental in getting my research project off the ground.

Many thanks to my collaborators Astrid Avellan, Will Gao, Emma Liu, Kayleigh Jones, Ann Valentine, Bandrea Weber, Kiana Morse, and Sheel Kundu. Working with them

has taught me how to ask the right questions and develop a path to pursue them. It's been a pleasure learning from all of them.

I've also benefitted from conversations with colleagues who have helped to shape my thinking about research and life in general, including Clint, Adam, Nizette, Stacey, Joe, Alex, Aniela, Djuna, Kai, Lauren S., Lauren C. Kelly, Chelsea, Sara, Megan, Yuxin, John, Jon, Ke, Dan, Eleanor, Stephanie, Garrett, Meng, Brian, Kedar, and Ron. I hope my next office is half as interesting as ours has been!

I owe so much to the love and support of my family. My mom, dad, brother, and sister always encouraged me to pursue my interests, no matter how weird or foreign they seemed. Growing up with them instilled in me the values of curiosity, stubbornness, and creativity—three traits that I needed to complete this dissertation.

I want to give special thanks to the one whose support I leaned on most heavily—my wife, Emmy. After seven years together, Emmy and I married in 2016, towards the end of my Ph.D. candidacy. Our wedding coincided with several immigration interviews, international paper work, visa applications, job searches, state-by-state nursing board decisions, permission slips to leave the country, and a raw-sewage flood in our apartment. At times, I felt completely overwhelmed, disoriented, and unsure about myself. Emmy was *always* there to help me get my bearings. Thank you for helping me through this.

I also acknowledge the NSF and EPA funding under NSF Cooperative Agreement EF-1266252, Center for the Environmental Implications of NanoTechnology (CEINT), the Integrative Graduate Education and Research Traineeship in Nanotechnology Environmental Effects and Policy fellowship program under grant no. DGE0966227, and the Bertucci Fellowship granted by the College of Engineering at Carnegie Mellon University.

Nano-sized materials are being used to address some of humanities greatest challenges—cancer therapy, food and water security, and environmental remediation. While extremely promising for these applications, the production, use, and disposal of nanomaterials have resulted in their release into environmental compartments. One major concern of any novel contaminant is how it interacts with bacteria. Bacteria play essential roles in human health, engineered systems, and ecological functioning. Bacteria are capable of macro-scale influence because they have evolved communication systems that enable coordinated behaviors. Communication among cells involves chemical signals that enter the environment, where they are subjected to its biogeochemistry, which now includes novel nanomaterials. The overall goal of this thesis was to improve understanding of the relationship between nanoparticles and cell-to-cell signaling behavior in bacteria focusing on two population-level behaviors: **autolysis** and **quorum sensing**. Specifically, this project sought to: (1) improve our understanding of how metal-oxide nanoparticles affect the autolytic process in *Bacillus subtilis*, by elucidating the biological response of the interactions between titanium dioxide nanoparticles and biomolecules; (2) reveal the interactions between quorum sensing signaling molecules and metal cations commonly used in antimicrobial nanomaterials, silver and copper; and (3) demonstrate the potential of quorum sensing-regulated cyanide production to affect oxidation and dissolution of gold nanoparticles in an environmentally relevant system. By addressing these objectives, the work demonstrated that:

1. TiO₂ nanoparticles disrupt the autolytic process by delaying the onset of autolysis, and intercepting released autolytic enzymes, preventing the enzymes from degrading peptidoglycan in neighboring cells.

2. Quorum sensing signaling molecules form complexes with Ag^+ and Cu^{2+} , removing the most bioavailable form (free HHL, Ag^+ , and Cu^{2+}) from the cells' environment.
3. Quorum sensing-regulated cyanide production induces oxidative dissolution in Au nanoparticles, which were previously assumed to be inert in environmental systems.

Taken together, this body of work highlights the relationship between nanoparticles and population-level behavior in bacteria. The presence of nanoparticles can have significant effects on population-level behaviors, and the activity of population-level behaviors can have significant effects on nanoparticles behavior. This inter-connected relationship, where the nanoparticles are both acted on and act upon their environment, must be considered in nanoparticle-based studies and applications.

Acknowledgments	iii
Abstract	v
Contents	vii
List of Tables	ix
List of Figures	x

Chapter

1	Introduction	1
	Quorum sensing	3
	Autolysis	6
	Objectives and structure of dissertation	8
2	Disruption of autolysis in <i>Bacillus subtilis</i> using TiO₂ nanoparticles	11
	Abstract	11
	Introduction	12
	Methods	14
	Results and Discussion	23
	Conclusions	33
3	Quorum sensing signals form complexes with cations	35
	Abstract	35
	Introduction	35
	Methods	37
	Results and Discussion	45
	Conclusions	52
4	The of susceptibility of gold nanoparticles to bio-dissolution by a cyanogenic bacterium	55
	Abstract	55
	Introduction	55
	Methods	58

Results and Discussion 63

Conclusions 68

5 Implications and remaining questions 70

Appendix A: Additional nanoparticle–bacteria interactions 74

MWCNTs had a higher absorption capacity for HHL compared to TiO₂ NPs 75

MWCNTs *increased* QS-regulated violacein production in *C. violaceum* 79

FeCl₃ induced violaceum synthesis in CV026 80

Appendix B: CuO nanoparticle dissolution by a siderophore-emitting bacteria and a cyanogenic bacteria 83

Pseudomonas fluorescens 83

Chromobacterium violaceum 86

References 89

Table

- 1-1** Bacteria, AHL names, chemical structures, Log K_{ow} , and QS response. Under the *Structure* column, you can see the conserved lactone ring moiety on the left-hand side of the molecule, and the varying R groups on the right. ¹Log K_{ow} values are predictive values at pH 7 and 25°C, taken from SciFinder. 6
- 2-1** Gene specific primer and probe sequences used for RT-qPCR. 22
- 3-1** LC-MS conditions used to detect metal-HHL complexation. 38
- 3-2** Visual MINTEQ simulation of chemical speciation of silver and copper(II) nitrate solutions in ammonium acetate buffer. 43
- 3-3** LC-MS conditions used to detect the loss of HHL as a function of Ag^+ and Cu^{2+} concentration. 50
- 3-4** Statistical analysis of the relationship between HHL hydrolysis and Ag or Cu concentrations shown in Figure 3-2. 50
- 3-5** Lengths (Å) of cation-oxygen bonds in compounds 1, 2, 3, and 4 of Figure 3-5E-H. 48
- 3-6** XYZ coordinates used to generate compounds 1, 2, 3, and 4 of Figure 3-5E-H 49
- 3-7** Best fit values (IC_{50} , mM) and profile likelihood from modeling the Gompertz equation (shown in Figure 3-8B). 54
- 4-1** Simulated species distribution of 100 μM NaCN in water at pH 7 and 7.5. 60
- 4-2** Au NP dissolution experimental matrix. 63
- 4-3** The best fit values [average (standard errors)], and R-square values used to describe Au dissolution in the presence of *C. violaceum* at pH 7 and pH 7.5 are presented. The Abiotic control and CV026 presented in Figure 4-1a were not modeled. 65
- A-1** Best fit parameters describing Figure A-1. 76

Figure

- 1-1** Quorum sensing in a gram-negative bacteria population with a LuxIR signaling circuit. The top portion of the schematic, labeled *Low cell density*, shows a population at relatively low cell density where a quorum has not yet been reached. The left-hand portion of the figure represents an overview of a cell in media. The right-hand side of the figure represents a cross-section of a cell wall under low (top) and high (bottom) cell density. Under Low cell density, AHL production occurs through the LuxI-AHL synthase, but the extracellular AHL concentration is not sufficiently high enough to diffuse back through the cell wall and complex with the LuxR receptor protein, and thus target gene expression is muted (as indicated by the white arrow). The bottom portion of the schematic shows a population at high cell density in which a quorum has been reached through significant accumulation of AHL in the extracellular environment. At high AHL concentrations, the LuxR receptor is complexed by AHL, in turn regulating the expression of target genes (as indicated by the red arrow). 5
- 1-2** Autolysis in a Gram-positive cell. (a) Under nutrient-rich conditions, a cell is able to maintain its proton-motive force (PMF) which allows protons to associate with teichoic acids embedded in the cell wall that keep the autolysins in their inactive form. (b) Autolysis: When nutrients are limited and the cells metabolism is unable to maintain the PMF, teichoic acids undergo a conformational change leading to an activation of autolysins which degrades the surrounding peptidoglycan ultimately resulting in turgor pressure rupturing the cell membrane and releasing intercellular matter. 8
- 2-1** Recorded temperatures, T , normalized to initial temperatures, T_0 , over time. The linear fit equation was used to calculate the delivered power of the sonicator, which was used to suspend TiO₂ nanoparticles into buffer. 15
- 2-2** TEM imaged of *B. subtilis* incubated with 50 mg/L TiO₂ NPs for 8 hour. (Left) Inset shows a close contact between TiO₂ NPs aggregates and cell wall. (Right) Some cells are lysing with lower electronic density due to a loss of intracellular substances. 16
- 2-3** Unmapped (a-c) and mapped (d-f) images of *B. subtilis* (10⁶ cells/mL), TiO₂ nanoparticles suspended (100 ppm) in buffer, and 5 mM bicarbonate buffer. All red pixels have spectral signatures identical to those in the spectral library (g). The red profile in (g) highlights the average spectral profile of the TiO₂ NP library. (h) Shows a shift in cell wall spectral profile; as more TiO₂ is present in the sample, the more the cell wall spectral profile shifts to the left, towards the average spectral profile of the TiO₂ NP library. 20

- 2-4** Colony Forming Unit (C) over time normalized to the initial Colony Forming Unit of each series (C_0) of *B. subtilis* in 5 mM NaHCO₃ buffer (pH 7.7) with exposure to various concentrations of TiO₂ NPs, and a no TiO₂ NP control in the absence of light. Each point represents the mean ($n=3$) with error bars representing the 95% confidence interval. 24
- 2-5** Fluorometry assay of DiSC₃₍₅₎ stained *B. subtilis* cultures in 5 mM NaHCO₃ in the presence of 50 ppm TiO₂ NPs and absence of TiO₂ NPs in the dark. Depolarization of *B. subtilis* membrane was monitored by measuring the fluorescence intensity at an excitation and emission wavelength of 643 nm and 666 nm, respectively, for 1 hour. Apparent equilibrium DiSC₃₍₅₎ between the cell membrane and the media, as indicated by a flat-line in fluorescence, took 40 minutes. 25
- 2-6** Unmapped (a1-g1) and TiO₂ mapped (a2-g2) images of *B. subtilis* (10^7 cells/mL) exposed to 0 (a, b), 1 ppm (c, d), and 100 ppm (e-g) TiO₂ NPs suspended in bicarbonate buffer (5 mM). Red pixels have spectral signatures identical to those in the TiO₂ NP spectral library. Figures with the same alphabetical identifier, e.g. a1 and a2, are identical images, however, a2 is mapped to identify TiO₂ location, whereas a1 is left unmapped. 26
- 2-7** Colony Forming Unit (C) over time normalized to the initial Colony Forming Unit of each series (C_0) of *B. subtilis* in 5 mM NaHCO₃ buffer (pH 7.7) with the addition of 50 ppm TiO₂ NPs at time points of 0 hour, 0.5 hour, and 1 hour in the absence of light. Each point represents the mean ($n=3$ or 2) with error bars representing the standard deviation. 27
- 2-8** (a) Adsorption isotherm of autolysins on TiO₂ NPs (pH 7.7 and 25°C) with the surface area concentration, Γ , plotted against the concentration of free enzyme in solution, C_w . (b) Relative change in in peptidoglycan over time after incubation with autolysins. Prior to exposure to peptidoglycan, autolysins were incubated with varying concentrations of TiO₂ NPs. The *Negative control* peptidoglycan was not exposed to any cell wall associated enzymes. The *Positive control* peptidoglycan was exposed to autolysins that were not incubated with TiO₂ NPs. 29
- 2-9** Proposed mechanisms for disruption of autolysis in *B. subtilis* in the presence of TiO₂ NPs. (a) TiO₂ NPs associate with the region of cell wall teichoic acids that make up the point of contact between the cell and NPs, altering autolysin activity and maintaining the PMF under nutrient limited conditions. (b) Once a cell has undergone autolysis, the released autolysins are adsorbed by TiO₂ NPs, which diminishes the peptidoglycan-degrading functionality, limiting enzymatic attack of peptidoglycan of other population members. 30
- 2-10** (a) *B. subtilis* growth (CFU/mL) and released double-stranded DNA (dsDNA) in minimal Davis media (blue) and 5 mM NaHCO₃ (red) over time. (b) L-alanine concentration measured in the supernatant of *B. subtilis* suspended in 5 mM

NaHCO₃. Each point represents the mean ($n=3$) and error bars represent standard deviation. 32

- 2-11** Expression (fold change relative to *rpoB*) of RNA encoding for *lytC*, *sdpC*, and *skfA* in cultures of *B. subtilis* after 1 hour of suspension in 5 mM NaHCO₃ in the presence or absence of TiO₂ NPs. Individual data points are plotted; thick bars represent the mean ($n=3$) and error bars represent the standard deviation. 33
- 3-1** Positive ion MS/MS spectra of (a) 10 mM HHL control, (b) 10 mM AgNO₃ control, (c) 10 mM Cu(NO₃)₂ control, and (d) 3:1 molar ratio HHL:Fe. 40
- 3-2** Hydrolyzed HHL as a function of increasing added Ag or Cu. 42
- 3-3** LC-MS spectra monitoring HHL hydrolysis product over time in the presence of Ag (a) and Cu (b). 43
- 3-4** Absorbance (OD₅₈₀) of violaceum in the presence of Ag, Cu, or a no-metal control. 45
- 3-5** Positive ion MS/MS spectra of (a) HHL:Ag and (b) HHL:Cu. ATR-FTIR spectra of (c) HHL:Ag and (d) HHL:Cu mixture minus cation-free HHL spectra on KBr tablet. Optimized structure of (e) **1** HHL(Ag⁺), (f) **2** HHL₂(Ag⁺), (g) **3** HHL(Cu²⁺), and (h) **4** HHL₂(Cu²⁺) using B3LYP 3-21G(d) and 6-31G(d) for silver and copper complexes, respectively. 46
- 3-6** Untreated ATR-FTIR scans of HHL, HHL + AgNO₃, and HHL + Cu(NO₃)₂ mixtures. 48
- 3-7** Violacein production by *C. violaceum* CV026 after 24 hours of growth (LB, 200 rpm, 30°C) as a function of HHL concentration. Orange dotted line indicates HHL concentration chosen to perform dose-response experiments presented in Figure 3-8a–b). 51
- 3-8** (a) Violacein production (OD₅₈₀) normalized to cell growth (OD₆₀₀) of *C. violaceum* CV026 exposed to AgNO₃ or Cu(NO₃)₂. (b) Dose-response curves fit using the Gompertz equation.¹⁴⁷ The X-axis of (a) and (b) represent the log molar concentration of added AgNO₃ or Cu(NO₃)₂. (c) Loss of free HHL as a function of relative molar concentrations of Ag or Cu. On all graphs, symbols represent the average, error bars represent the standard error of the mean (SEM), and significance asterisks are the results of unpaired t-tests versus the CV026 + HHL Control: * $P < 0.05$, ** $P < 0.01$, *** $P < 0.001$. 53
- 4-1** (a) pH of and (b) CFU in soil used in the Au NP dissolution experiments over time. Symbols represent the average ($n=3$), error bars represent the standard error of the mean. 61
- 4-2** (a) Dissolution kinetics of Au NPs in sterile soil, soil supplemented with *C. violaceum*, and soil supplemented with CV026. (b) Dissolution kinetics of Au NPs

in initially sterile soil that was supplemented with 2.5% (by weight) soil containing *C. violaceum*. The Y-axis is the same for both (a) and (b), representing the percentage of gold dissolved from a total concentration of 1.9 parts per million. 65

- 4-3** (a) Dissolution of Au NP after 24 hours in sterile LB media, early-stationary phase cultures of *C. violaceum* that had been washed in LB media, or the supernatant of an early-stationary stage culture of *C. violaceum*. Y-axis represents the percentage of gold dissolved from a total concentration of 1.9 parts per million. (b) Detection of dicyanogold, $\text{Au}(\text{CN})_2^-$ using an ESI-MS/MS procedure by monitoring the cyanide product ion, m/z 26, of the dicyanogold parent ion, m/z 249. 66
- 4-4** (a) Au NP dissolution (%) and cyanide production over time with an inlay that plots Au dissolution versus CN^- . (b) Au dissolution (%) and cell growth over time with an inlay that plots Au dissolution versus OD_{600} . The values in the inlay represent the R^2 and Spearman's rho (ρ). 67
- 4-5** (a) Dissolution of Au NP after 24 hours in sterile buffer or NaCN solution. (b) Detection of dicyanogold, $\text{Au}(\text{CN})_2^-$. Y-axis for (a) represent the percentage of gold dissolved from a total concentration of 1.9 parts per million. 68
- 4-6** Au NP dissolution (%) over time in a sterile buffer (Control, pH 7) and a cyanide solution (9.8 ppm, pH 7). 68
- A-1** (A) Adsorption isotherms of HHL to MWCNTs and TiO_2 . (B) Suspensions of MWCNTs 10 minutes after sonication with HHL (C1) and without HHL (C5). (C) Proposed interaction between HHL and MWCNTs. 76
- A-2** Difference in hydrodynamic radius of TiO_2 NP suspensions after sonication with and without ODDHL. 76
- A-3** HHL reporter plate assay. LB agar plates inoculated with CV026 turn purple around the added sample if HHL is present. 77
- A-4** HHL reporter plate assay. A purple ring indicates that HHL is present in the well. This is a semi-quantitative way to determine relative HHL concentrations and their biological activity. 78
- A-5** (a) Growth inhibition of *C. violaceum* wild-type after being incubated for 24 hours in the presence of various NPs (100 ppm), relative to a no-NP control (dotted-line). Violacein production in of *C. violaceum* wild-type after being incubated for 24 hours in the presence of various NPs (100 ppm), relative to a no-NP control (dotted-line). 79
- A-6** Violaceum production is measured via fluorescence at $\text{nm}=585$. To verify that the increase in violacein production presented in Figure A-5, was not due to MWCNTs

interference with fluorescence, we added 100 ppm of MWCNTs to extracted violaceum. 80

- A-7** Well diffuse assay demonstrating that FeCl₃ induced violacein synthesis in the QS-mutant CV026. 81
- A-8** Colony Forming Unit (C) over time normalized to the initial Colony Forming Unit of each series (C₀) of *B. subtilis* in 5 mM NaHCO₃ buffer (pH 7.7) with exposure to 50 ppm CeO₂ containing various coatings. 82
- B-1** Two different extraction methods were used to quantify Cu dissolution from CuO NPs in sterile soil (Abiotic, copper circle), soil supplemented with a 5-day culture of *Pseudomonas fluorescens* (green triangle), and soil supplemented with a washed 5-day culture of *P. fluorescens* (beige square). (a) Extractable Cu using 0.005 M diethylenetriaminepentaacetic acid (DTPA). (b) Extractable Cu using 0.01 M CaCl₂. The Y-axis is the same for both (a) and (b), representing the percentage of Cu dissolved from a total concentration of 11 parts per million as CuO NPs. The soil moisture content was maintained at 16% across all treatments. 85
- B-2** Extractable Al, Mn, and Fe from soil after inoculation with *P. fluorescens*. 86
- B-3** CuO NP dissolution (%) over time exposed to a culture of *C. violaceum* (green triangles), the supernatant of a culture of *C. violaceum* (beige squares), or in LB media (control, red circles). 87
- B-4** CuO NP dissolution (%) over time in an abiotic buffer containing HHL (beige squares), NaCN (green triangles), or a control (red circles). 88

1. Introduction

Nano-sized materials are being used to address some of humanities greatest challenges—cancer therapy¹, food and water security², and environmental remediation.³ While extremely promising for these applications, the production, use, and disposal of novel nanomaterials has resulted in their release into environmental compartments.^{4,5} A recent publication focusing on engineered nanomaterial emissions in the European Union estimates that by 2020, 20,000 metric tonnes of nano-sized titanium dioxide (TiO₂) will be released annually into surface waters, and an additional 20,000 metric tonnes will be released to soils.⁶ Similarly, nano-sized silver (Ag) emissions to surface waters are projected to reach 15 metric tonnes per year within the next few years.⁶ And carbon nanotube (CNT) emissions are expected to reach 40 metric tonnes annually by 2026.⁶

Due to the increase in production, the general public, and their governments, are concerned about the introduction of these novel materials into the environment.⁷⁻¹⁰ A major environmental concern of any new contaminant is its interaction with microorganisms. Prokaryotic organisms, such as bacteria, are found in every environmental compartment: soil, sediment, air, and water. Bacteria play fundamental roles in ecological function and productivity (e.g., nutrient cycling and decomposition of organic matter). Bacteria are also essential in engineered systems (e.g. in the removal of contaminants in wastewater treatment plants¹¹ and bioremediation processes) and in human health (e.g., digesting food and fighting disease¹²). Understanding the interactions between novel engineered nanomaterials and bacteria is critical to maximize utility and minimize unintended consequences.

Early nanoparticle* (NP) toxicity research focused on isolated microorganisms in simple systems. These studies reported different organisms have different sensitivities¹³, NP concentration matters¹⁴, NP size matters¹⁵, and modes of toxicity vary (e.g., some compromise of cell wall integrity¹⁶, some altered macromolecule and enzyme functionality¹⁵, some NPs disrupt cell growth¹⁷, while others alter gene expression¹⁸ or damage DNA¹⁹). Following these early studies on specific phenomena, researchers have explored environmental nanotoxicity from an ecological perspective by studying NP transformations in the environment and shifts in microbial communities.^{20–22} And significant progress has been made. For example, NP transformations such as oxidation and sulfidation greatly reduce NP toxicity²³; soil microbial communities are more sensitive to inorganic NPs than organic NPs²¹; and microbial communities can recover from acute doses of copper and silver NPs.²² Despite the important advancements in organismal and community studies, little attention has been paid to the effects of NPs on population-level bacterial behavior.

Bacteria participate in coordinated, population-level behaviors to enhance survival. In many population-wide activities, communication and coordination of behavior occurs through a range of chemical signals that are emitted into the extracellular environment. Collective behaviors include quorum sensing^{24,25}, autolysis^{26–28}, cannibalism^{29,30}, and programmed cell death^{31,32}. Population-level behaviors in bacteria are important for their survival and can have profound impacts on their environment. For example, autolysis in *Bacillus subtilis* increases DNA transformation³³, and quorum sensing controls nitrogen cycling in rhizosphere proteobacteria.³⁴ Given the current and anticipated future releases of nanomaterials into the environment, their potential to affect population-level behavior requires attention. The present

*A sensible definition for an *engineered nanomaterial* is a topic of international debate.²²⁶ In this dissertation we use the EPA's definition: "an ingredient that contains particles that have been intentionally produced to have at least one dimension that measures between approximately 1 and 100 nanometers". We also use *nanomaterial* and *nanoparticle* interchangeably and use the abbreviation *NP*.

work examines the effects of different NPs, and their released ions, on two population-level systems: **quorum sensing** and **autolysis**.

Quorum sensing

The coordinated behavior enabled by quorum sensing (QS) is responsible for a wide range of microbial activities, including: virulence^{35,36}, bioluminescence³⁷, antibiotic and antioxidant synthesis³⁸, autolysis²⁸, nitrogen fixation³⁹, biofilm formation^{35,40}, cyanide production^{38,41}, siderophore production⁴², and CRISPR-Cas adaptive immunology.⁴³ QS is a critical component of microbial behavior in environmental engineering, agriculture, and human health systems. For example, QS systems can regulate nutrient cycling³⁴ and fungicidal activity⁴⁴ on plant root nodules in rhizosphere soils. In engineered systems, QS-regulated biofilms are problematic for industrial pipe networks⁴⁵, water treatment membranes⁴⁶, and medical devices.⁴⁷ Furthermore, QS-regulated virulence factors are active in multiple infectious organisms: *Staphylococcus aureus* is a leading cause of hospital infections⁴⁸; *Vibrio cholera* is a water borne pathogen that causes the eponymous cholera disease⁴⁰; and *Pseudomonas aeruginosa* toxins and cyanide formation can be lethal to cystic fibrosis patients.^{49,50} Thus, understanding the potential effects of NPs on QS would have significant impacts on a number of fields.

During QS, populations of bacteria are able to sense their local cell density and coordinate gene expression through the secretion and detection of small organic molecules, known as autoinducers (AI). Bacteria constitutively produce and release AIs. AIs are recognized by neighboring cells' transmembrane (Gram-positive) or intercellular (Gram-negative) receptors. A receptor–protein complex activates gene expression when the extracellular concentration of AIs exceeds a threshold. Gene expression induced by AIs is diverse and varies among species. By managing gene expression via cell density, cell

populations are able to control energetically expensive processes that are only effective when acting as a group (e.g., bioluminescence, biofilm formation, and the secretion of virulence factors).⁵¹

The best-studied class of AI in gram-negative bacterial species are acyl-homoserine lactones (AHL).^{38,52-56} Different AHLs are produced by hundreds of different gram-negative bacterial species.⁵⁷ AHLs are produced in the cell by an AHL synthases (LuxI-type). Once synthesized, AHLs diffuse freely between the cell and external environment (**Figure 1-1**). AHL signals are detected via cytoplasmic transcription factors receptors (LuxR-type), and are highly specific. The LuxR protein dimerizes with its specific cognate AHL, which then binds to DNA sequences upstream of target genes, controlling their expression.⁵⁸⁻⁶⁰ AHL-LuxR dimerization is concentration dependent, so QS-regulated gene expression occurs only when a certain concentration of the appropriate AHL is present in the microenvironment. The AHL activation concentration is generally in the nanomolar range.^{38,61}

The chemical structure of AHL has a conserved lactone-ring with differing, species-specific, hydrocarbon -R group side chains (**Table 1-1**). The -R groups affect stability and signaling dynamics.⁶² The amphipathic nature of AHLs is presumably necessary to enable them to diffuse across the gram-negative cell membrane to reach the intracellular receptor.⁵² AHL-LuxR binding specificity depends on the -R side chains of AHLs and the amino acid variation in the LuxR binding pocket.⁵⁶

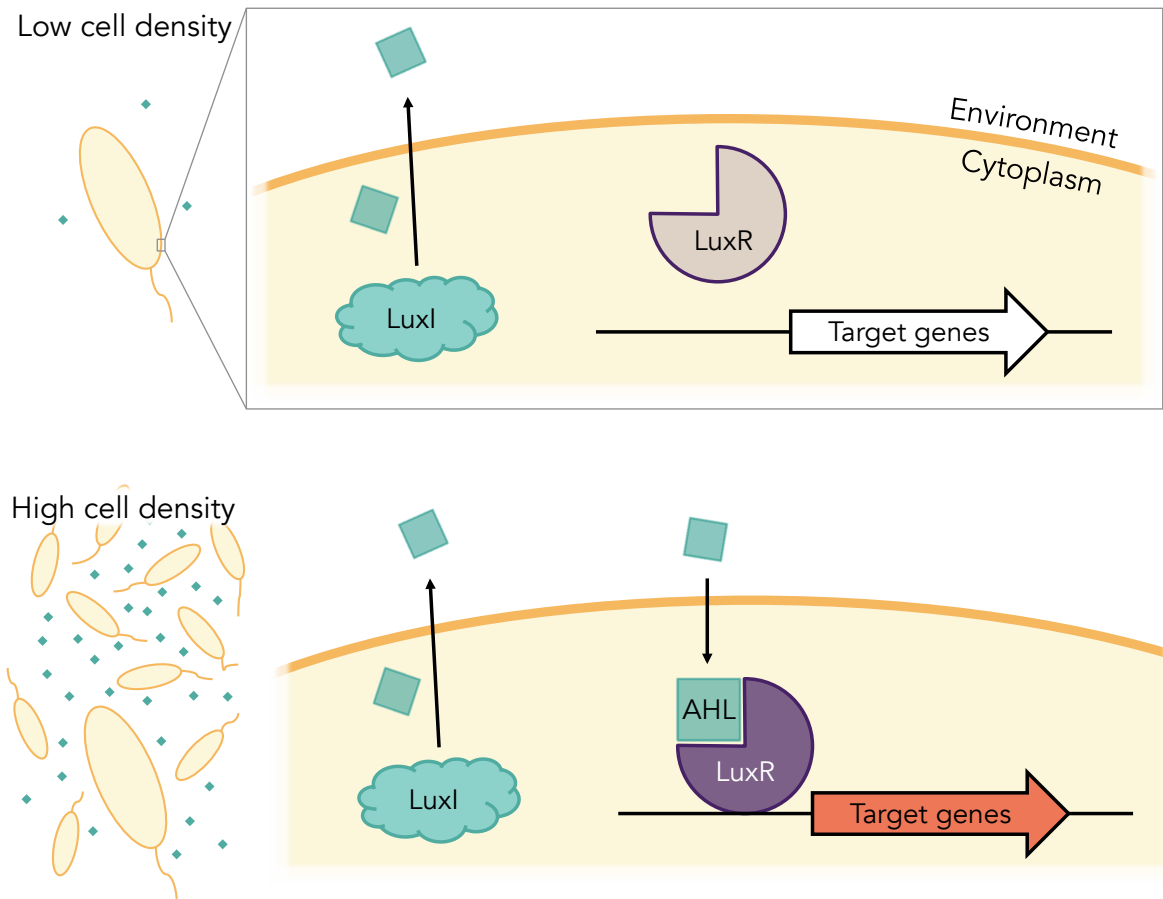
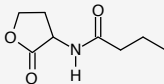
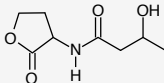
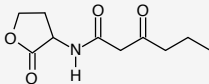
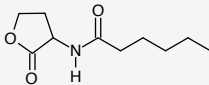
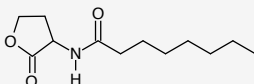
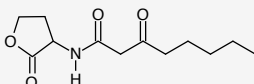
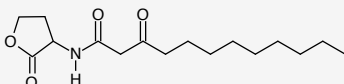
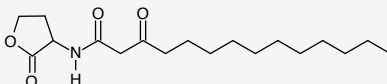


Figure 1-1. Quorum sensing in a gram-negative bacteria population with a LuxIR signaling circuit. The top portion of the schematic, labeled *Low cell density*, shows a population at relatively low cell density where a quorum has not yet been reached. The left-hand portion of the figure represents an overview of a cell in media. The right-hand side of the figure represents a cross-section of a cell wall under low (top) and high (bottom) cell density. Under *Low cell density*, AHL production occurs through the LuxI-AHL synthase, but the extracellular AHL concentration is not sufficiently high enough to diffuse back through the cell wall and complex with the LuxR receptor protein, and thus target gene expression is muted (as indicated by the white arrow). The bottom portion of the schematic shows a population at high cell density in which a quorum has been reached through significant accumulation of AHL in the extracellular environment. At high AHL concentrations, the LuxR receptor is complexed by AHL, in turn regulating the expression of target genes (as indicated by the red arrow).

Table 1-1. Bacteria, AHL names, chemical structures, Log K_{ow} , and QS response. Under the *Structure* column, you can see the conserved lactone ring moiety on the left-hand side of the molecule, and the varying R groups on the right. $^1\text{Log } K_{ow}$ values are predictive values at pH 7 and 25°C, taken from SciFinder.

Bacteria AHL name (abbreviation)	Structure	$^1\text{Log } K_{ow}$	Response
<i>Pseudomonas aeruginosa</i> N-Butanoyl-L-HL (BHL)		-0.82	Virulence
<i>Vibrio harveyi</i> N-Hydroxybutyryl-L-HL (hBHL)		-2.21	Luminescence
<i>Erwinia carotovora</i> N-3-Oxohexanoyl-L-HL (OHHL)		-0.83	Antibiotic
<i>Chromobacterium violaceum</i> N-Hexanoyl-L-HL (HHL)		0.20	Antioxidant
<i>Ralsonia solanacearum</i> N-Octanoyl-L-HL (OHL)		1.22	Biofilm
<i>Agrobacterium tumefaciens</i> N-3-oxooctanoyl-L-HL (OOHL)		0.19	Conjugation
<i>Pseudomonas aeruginosa</i> N-3-Oxododecanoyl-L-HL (OdDHL)		2.23	Virulence
<i>Rhizobium leguminosarum</i> N-Oxotetradecanoyl-L-HL (OtDHL)		3.25	Root nodulation

Autolysis

Autolysis is another form of population-level behavior in bacteria and is the topic of the research presented in Chapter 2. Autolysis is characterized by the self-digestion of the cell wall, resulting in complete cellular lysis. The population benefits of autolysis are thought to include the provision of nutrients to other cells and the transfer of genetic material.^{28,32} Autolysis is also involved in the final step of spore formation when the mother cell is lysed, releasing the spore.³² In some species, autolysis has been linked directly to quorum sensing.³⁵ In systems where biomass growth is critical (e.g., industrial bioprocesses), controlling autolysis will alter biomass yield and production of target products.⁶³ In the environment, the prevention of autolysis is responsible for the fossilization of some bacteria.⁶⁴

The autolytic process is a response to limited nutrient availability or cell density^{32,35,65,66}, and results in the release of cellular debris following the enzymatic degradation on the cell wall (**Figure 1-2**). In gram-positive bacteria many environmental responses (e.g., antibiotic adaptation, surface attachment, metal adsorption, and autolysis) are executed in or on the cell-wall.^{67,68} The cell-wall is comprised of a matrix of peptidoglycan, teichoic acids, and autolysins that confer structural integrity and enable the maintenance of a proton gradient.^{69,70} The aggregation of teichoic acids and electronegative peptidoglycan layers give rise to the negatively charged cell wall, where protons can accumulate as the proton-motive force (PMF).⁷¹ While it is generally agreed upon that teichoic acids are responsible for limiting autolysin activity, there is no consensus on the mechanism of action. It has been proposed that the dispersal and subsequent protonation states of D-alanyl esters throughout the cell wall matrix could provide a unique network to systematically determine the activity of autolysins, which require unique ionic microenvironments.^{71,72} A dissipation of the PMF results in a chain-reaction-like collapse where the orderly cell wall proton and charge distribution is lost. This could lead to the uncontrolled conformation of teichoic acids, giving rise to unlimited autolytic activity. Although certain key components have been identified, the signal and response of cell death mechanisms, such as autolysis, remain mostly unknown.

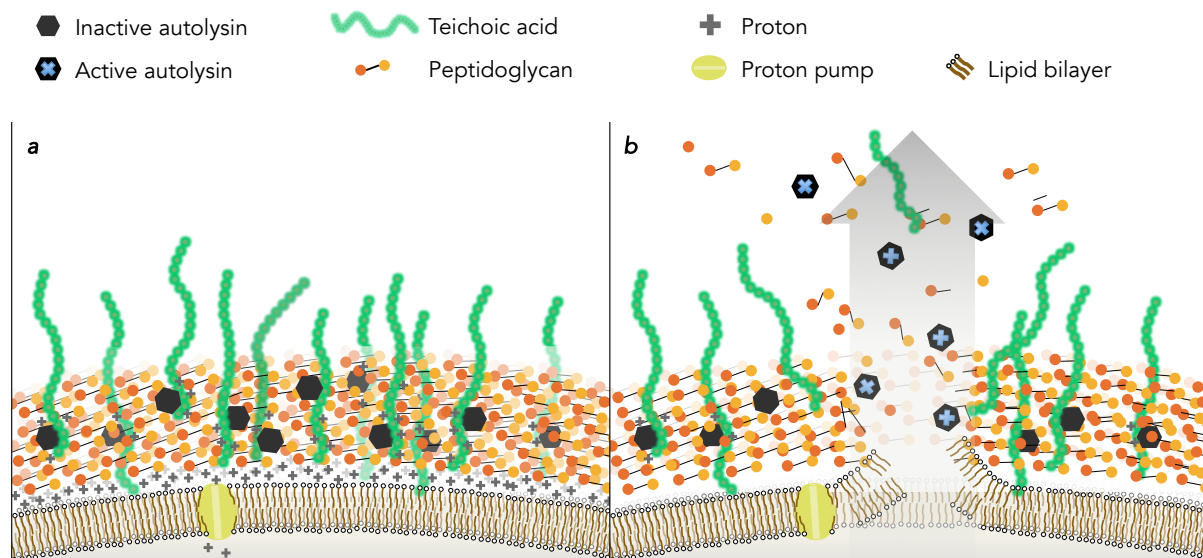


Figure 1-2. Autolysis in a Gram-positive cell. (a) Under nutrient-rich conditions, a cell is able to maintain its proton-motive force (PMF) which allows protons to associate with teichoic acids embedded in the cell wall that keep the autolysins in their inactive form. (b) Autolysis: When nutrients are limited and the cell's metabolism is unable to maintain the PMF, teichoic acids undergo a conformational change leading to an activation of autolysins which degrades the surrounding peptidoglycan ultimately resulting in turgor pressure rupturing the cell membrane and releasing intercellular matter.

Objectives and structure of dissertation

The overarching goal of this thesis is to improve understanding of the interactions between NPs and population-level behaviors in bacteria, specifically, in quorum sensing and autolysis. This goal is accomplished by linking physiochemical interactions between different classes of NPs and biological molecules with biological effects in the autolytic process (Chapter 2) and quorum sensing (Chapters 3 and 4).

This dissertation begins with a look at how one of the most produced, used, and released NPs⁶, TiO₂, affects autolysis in a gram-positive bacterium, *Bacillus subtilis* (Chapter 2). The work presented in Chapter 2 aimed to determine if TiO₂ NPs interfere with the autolytic process in *B. subtilis*, with a sub-objective of informing a mechanism of TiO₂ NP interference with the autolytic process. We hypothesized that TiO₂ NP surfaces would deposit on and adsorb biomolecules that regulate autolysis, limiting their functionality. There is a

small body of work demonstrating the interactions between TiO₂ surfaces and individual components of the autolytic process⁷³ and lytic enzymes.⁷⁴ These studies revealed protein adsorption and deformation *in vitro*, but did not test *in vivo* implications. Our results demonstrate that TiO₂ NPs deposit on the cell wall of *B. subtilis*, where teichoic acids and the PMF regulate the onset of autolysis, and that released autolysins adsorb to TiO₂ surfaces reducing their peptidoglycan-degrading ability. The results from Chapter 2 are the first to present the effect of any NP on autolysis *in vivo*, and are published in *Scientific Reports*.⁷⁵

In Chapters 3 and 4, the concept of a mutually important interaction between QS and NPs is discussed. The main objective of Chapter 3 was to investigate the interaction between a QS signaling molecule (*N*-hexanoyl homoserine lactone, HHL) and two commonly released cations used in antimicrobial NPs, silver (Ag⁺) and copper (Cu²⁺). We hypothesized that HHL, which are similar to biogenic organic chelants⁷⁶, could complex these metal cations. We further hypothesized that complexation between free HHL and Ag⁺ or Cu²⁺ would limit the bioavailability of each constituent, reducing metal toxicity and decreasing the concentration of free signaling molecule. We observed that QS signaling molecules formed complexes with Ag⁺ and Cu²⁺. The chemical interactions between cations and HHL were revealed using experimental and computational chemistry techniques. The bioavailability of the complexes was then tested in a model QS organism, *Chromobacterium violaceum*. We observed decreased QS activity and metal toxicity (in the case of Ag⁺). The contents of Chapter 3 are currently (12/6/2017) under peer-review for publication in *ACS Chemical Biology*.

The main objective of Chapter 4 was to investigate the potential for QS-regulated cyanide to oxidize and dissolve gold NPs in an environmentally-relevant system. We tested the ability of a cyanogenic soil bacterium, *C. violaceum*, to oxidize and solubilize Au NPs in soil. Since cyanide production in *C. violaceum* is regulated by QS, we hypothesized that a

mutant strain, incapable of synthesizing HHL (*C. violaceum* CV026), would not dissolve Au NPs. In addition, we hypothesized that slight pH changes in the soil would result in different dissolution values due to changes in the speciation of cyanide. Moreover, we investigated Au NP oxidation in pure cultures and abiotic cyanide solutions. This research demonstrated that Au NPs can be oxidized and solubilized to $\text{Au}(\text{CN})_2^-$ by *C. violaceum* in soil, and that Au NP dissolution is limited by QS-regulated HCN production and speciation. Au NPs are frequently assumed to be inert under environmental conditions. Results from our work cast doubt on that assumption. Chapter 4 is currently being prepared for submission.

Our concluding remarks and thoughts on future research in this area are discussed in Chapter 5.

Finally, there are two appendices, which contain supplemental information and interesting findings that did not directly fit into Chapters 1–5. Specifically, Appendix A: Additional nanoparticle–bacteria interactions explains what led us from the results in Chapter 2: that NP surfaces can adsorb and alter the activity of compounds as they travel from one cell to another—to the topic of Chapter 3: released cations complex QS signals. Appendix A: Additional nanoparticle–bacteria interactions presents the adsorptive properties between QS signaling molecules and NP surfaces (TiO_2 and multi-walled carbon nanotubes), as well as an interesting observation that FeCl_3 appeared to induce a QS activity in *C. violaceum* CV026, the HHL-negative mutant. Appendix B presents how CuO NP dissolution can be influenced by a cyanogenic bacterium (*C. violaceum*), and a siderophore-emitting bacterium (*Pseudomonas fluorescens*).

2. Disruption of autolysis in *Bacillus subtilis* using TiO₂ nanoparticles[†]

Abstract

In contrast to many nanotoxicity studies where nanoparticles (NPs) are toxic or reduce viable cells in a population of bacteria, we observed that increasing concentration of TiO₂ NPs increased the cell survival of *Bacillus subtilis* in an autolysis-inducing buffer by 0.5 to 5 orders of magnitude over an 8-hour exposure. Molecular investigations revealed that TiO₂ NPs prevent or delay cell autolysis, an important survival and growth-regulating process in bacterial populations. Overall, the results suggest two potential mechanisms for the disruption of autolysis by TiO₂ NPs in a concentration dependent manner: (1) directly, through TiO₂ NP deposition on the cell wall, delaying the collapse of the proton-motive force and preventing the onset of autolysis; and (2) indirectly, through adsorption of autolysins on TiO₂ NP surfaces, limiting the activity of released autolysins and preventing further lytic activity. Enhanced darkfield microscopy coupled to hyperspectral analysis was used to map TiO₂ deposition on *B. subtilis* cell walls and released enzymes, supporting both mechanisms of autolysis interference. The disruption of autolysis in *B. subtilis* cultures by TiO₂ NPs suggests the mechanisms and kinetics of cell death may be complicated in natural systems where metal oxide surfaces are abundant.

[†] This chapter has been published as: McGivney, E., Han, L., Avellan, A., VanBriesen, J., & Gregory, K. B. "Disruption of Autolysis in *Bacillus subtilis* using TiO₂ Nanoparticles." *Scientific Reports* 7 (2017).⁷⁵

Introduction

Nutrient availability is often the critical factor limiting growth and controlling a bacteria population's behavior.^{32,65,66} In response to changing environmental conditions, bacteria participate in population-level behavior such as autolysis, cannibalism, and programmed cell death.^{25-27,29-32} Autolysis, the self-digestion of the cell wall, is associated with several essential cell functions in bacteria, including spore formation, providing nutrients for persisting cells, and the transfer of genetic material to the remaining population.^{31,32} Cannibalism is a precursor to sporulation in which non-sporulating sister cells produce toxins to collapse the proton-motive force and induce autolysis in neighboring cells of the same population.^{29,30} Autolysis and cannibalism have also been linked to biofilm maintenance and growth, and the secretion of lytic proteins.²⁹⁻³¹ Most recently, autolysis has been directly linked to quorum sensing and biofilm formation in *Pseudomonas aeruginosa*.³⁵

In gram-positive bacteria, such as *Bacillus subtilis*, the autolytic process occurs in the cell wall, which is comprised of a matrix of peptidoglycan, teichoic acids, autolysins, and a proton gradient. The aggregation of acidic polymers, such as teichoic acids, and electronegative peptidoglycan layers give rise to the negatively charged cell wall, where protons can accumulate as the proton-motive force (PMF). A balance of protons and counter ion binding sites associated with teichoic acids maintains the structural integrity and functionality of the cell wall matrix.^{69,70} Jolliffe et al. (1981) demonstrated that when deprived of a carbon source, the PMF of *B. subtilis* collapses, leading to autolysis, characterized by the self-digestion of the cellular envelope and subsequent release of cytoplasmic materials to the surrounding environment (**Figure 1-2**). It has been suggested that the released cellular matter may be used as substrate for the remaining population to persist.^{30,32} Under more favorable cell growth conditions, where nutrients are abundant, autolysins are spatiotemporally

activated within the peptidoglycan matrix in a controlled process where they mediate essential tasks such as peptidoglycan turnover, cellular division, and sporulation.

It has been estimated that 50% of wall-associated teichoic acids extend beyond the cell wall creating what could be imagined as “fluffy” region⁷⁸⁻⁸⁰, which would be the point of contact between a cell and a surface in the environment. While it is generally agreed upon that teichoic acids are responsible for limiting the activity of autolysins, there is no consensus on the mechanism of control. It has been proposed that the dispersal and subsequent protonation states of D-alanyl esters throughout the cell wall matrix could provide a unique network to systematically determine the activity of autolysins, which require unique ionic microenvironments.⁷¹ Since the local environment determines the packing density of protons, and thus counter-ion binding sites, the activity of autolysins is concomitantly related.⁷² A dissipation of the PMF results in a chain-reaction-like collapse where the orderly cell wall proton and charge distribution is lost, which could lead to the uncontrolled confirmation of teichoic acids, giving rise to unlimited autolytic activity.

The interaction between wall-associated teichoic acids and materials with high specific surface areas, such as nanoparticles, has been highlighted by Jiang et al. (2010), who demonstrated that metal oxide NPs (Al_2O_3 , TiO_2 , and ZnO) adsorbed and altered the structure of cell wall biomolecules, including teichoic acids *in vivo*.⁷³ It was suggested that the resulting teichoic acid structural changes that occur when gram-positive bacterium and metal-oxide nanomaterials interact might be responsible for bacterial toxicity.⁷³ Through solid-state NMR studies, Wickman & Rice, further concluded that, when lipoteichoic acids were simultaneously adhered to peptidoglycan, the positively charged alanine group binds to the surface of negatively charged TiO_2 .⁸¹ This suggests that metal oxide NPs may also play a role in the modification of cellular processes that are mediated through structural changes in cell-wall proteins, such as autolysis. However, to the best of our knowledge, no research has

highlighted the influence of metal oxide surfaces on autolysis. We chose TiO₂ NPs as a model nanomaterial for its high production rate, consumer and industrial usage, and projected release into environmental compartments.^{4-6,82} Furthermore, while TiO₂ NPs are a semiconducting material that generate reactive oxygen species when irradiated with ultraviolet light^{83,84}, in the absence of a UV source TiO₂ NPs are not known to be particularly toxic to microorganisms.⁸⁴⁻⁸⁶ Using *Bacillus subtilis* as a model, the concentration dependence and kinetics of autolytic disruption, the impact of TiO₂ NPs on the PMF and activity of released lytic enzymes, and the hyperspectral mapping of TiO₂ deposition on the cell wall are described.

Methods

TiO₂ nanoparticle preparation and characterization. Degussa P-25 TiO₂ (70% anatase/30% rutile) NPs were suspended (0.3% wt.) in 15 mL of sterile lysis buffer (5 mM NaHCO₃ buffer pH 7.0), via probe sonication (550 Sonic Dismembrator, Fischer Scientific) with an acoustic power input of 4.11 W (determined using calorimetric method described by Taurozzi et al., **Figure 2-1**) for 10 minutes in a glass beaker. To serve as a stock solution, the suspension was further diluted to 3 g/L and stored at room temperature in a glass bottle wrapped in aluminum foil. Prior to experimentation, the stock solution was diluted in the lysis buffer to 1000 ppm and probe sonicated (under the same power level as described above) for 10 min and then diluted to the desired TiO₂ NP concentration.

Dynamic light scattering (DLS) measurements were collected on an ALV CGS-3 goniometer with ALV/LSE-5004 Light Scattering Electronics and Multiple Tau Digital Correlator. All samples were prepared in 5 mM NaHCO₃ and adjusted to pH 7.7 using HCl or NaOH. Two-minute duration measurements were taken in triplicate on 1 mL of 10 ppm TiO₂ NPs. Analysis of the autocorrelation function was performed using a constrained

regularization algorithm in the ALV-7004 Correlator Software. Diffusion coefficients, D , were converted to hydrodynamic radius, d_H values using the Stokes-Einstein Equation:

Equation 2-1

$$d_H = kT/3\pi\eta D$$

where k is the Boltzmann constant, T is the absolute temperature, and η is the viscosity of the solution. The electrophoretic mobility of TiO₂ NPs was measured using a Malvern nano ZS Zetasizer (Conductivity: 0.557 mS.cm; Temperature: 24.9°C; Count Rate: 172.8 kcps) and converted to zeta potential using the Smoluchowski relationship.⁸⁸ The intensity-averaged hydrodynamic diameter of the TiO₂ NPs, as determined by DLS, was centered around 250 nm (standard deviation: 8 nm) and the zeta potential was found to be -41.3 mV (standard deviation: 5 mV).

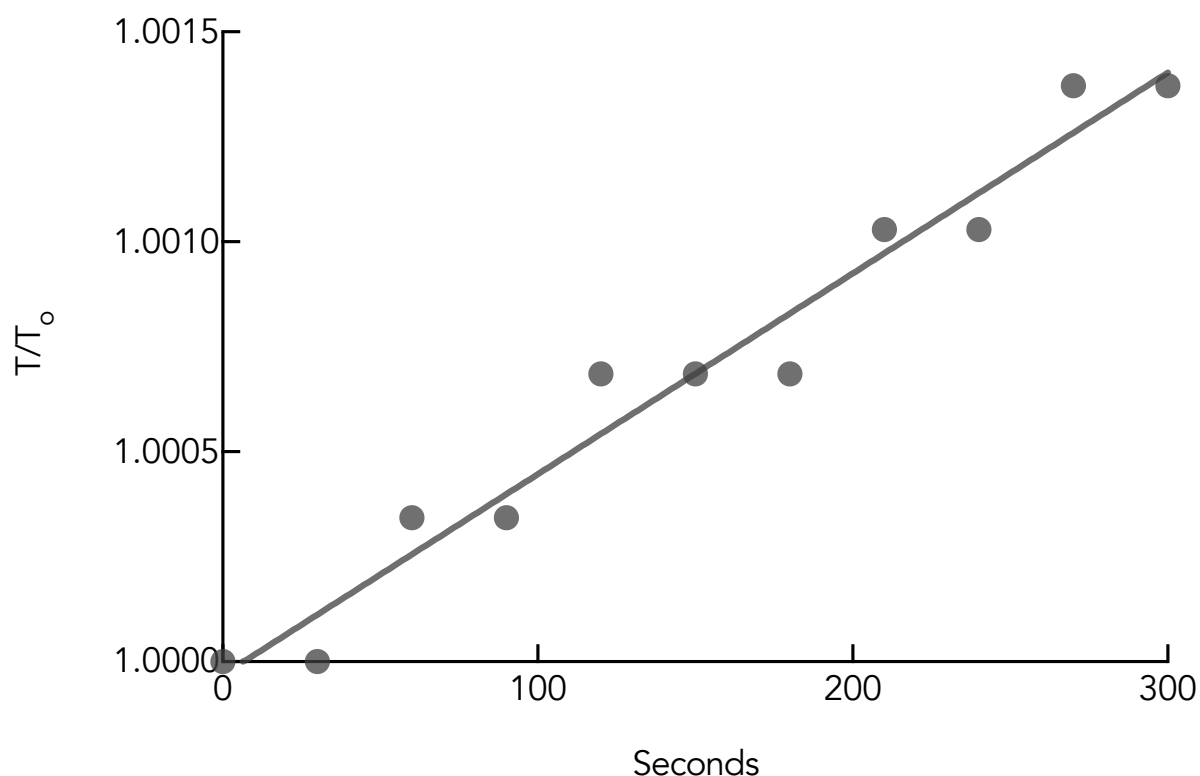


Figure 2-1. Recorded temperatures, T , normalized to initial temperatures, T_0 , over time. The linear fit equation was used to calculate the delivered power of the sonicator, which was used to suspend TiO₂ nanoparticles into buffer.

Transmission electron microscopy (TEM) imaging was used to observe the primary and aggregate TiO₂ NPs size distribution. All TEM images were produced after *B. subtilis* cells were exposed to TiO₂ NPs. TEM samples were fixed with 1% formaldehyde and 1% glutaraldehyde in 5 mM NaHCO₃ for 24 hours at 4°C. An aliquot of 1 μL was then placed on a carbon coated copper grid for examination. TEM images showed that TiO₂ NPs were visible aggregates consisting of primary particles ~20 nm in diameter and distinct from cell components with higher electronic density (**Figure 2-2**). Some TiO₂ NPs appeared to be closely associated with the cell wall of *B. subtilis*.

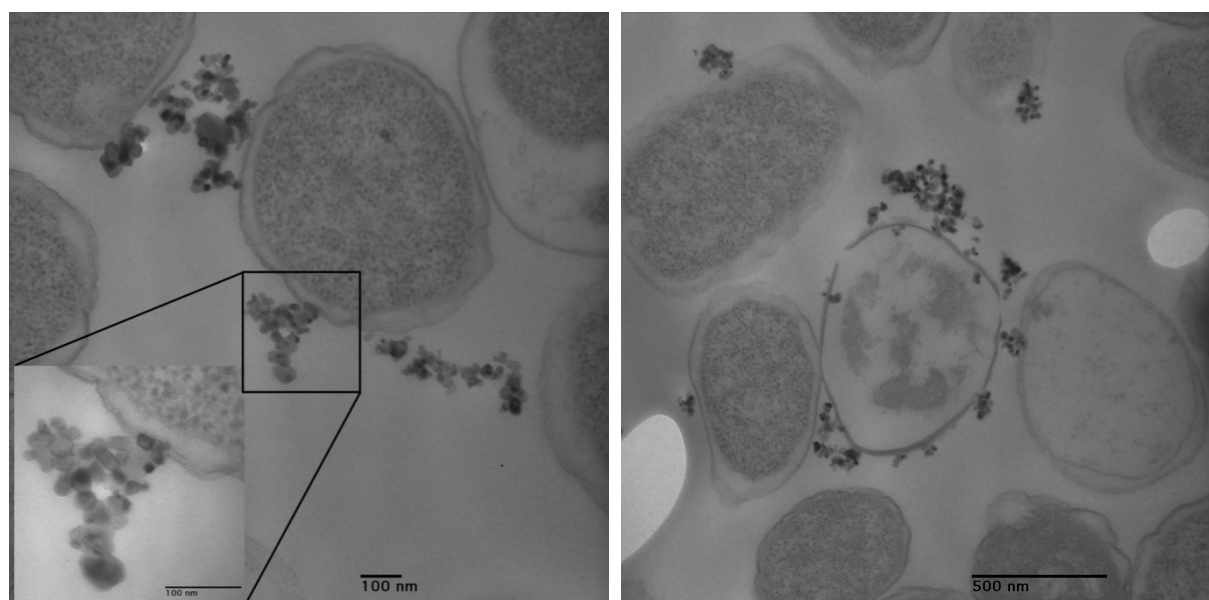


Figure 2-2. TEM imaged of *B. subtilis* incubated with 50 mg/L TiO₂ NPs for 8 hour. (Left) Inset shows a close contact between TiO₂ NPs aggregates and cell wall. (Right) Some cells are lysing with lower electronic density due to a loss of intracellular substances.

Cell culture selection. *Bacillus subtilis* ATCC 6051 is a well-studied model organism for autolysis research.^{77,89-91} It is ubiquitous in the environment and known to have several survival strategies, e.g., biofilm formation, spore formation, and motility.^{92,93} It is a robust bacterium used in biotech applications, such as enzyme production⁹⁴, and laboratory toxicity studies as a model gram-positive organism.¹⁴

Preparation of cell cultures. Experimental cultures of *B. subtilis* were grown in 20 ml of LB broth at 37°C, aerobically on a shaker plate, for 10 hours, to reach a concentration of 10⁸

CFU/mL. Cells were harvested via centrifugation (4,000g, for 7 minutes at 4°C) followed by resuspension of the pellet in lysis buffer to rapidly deplete the culture of a nutrient source. Washing was repeated twice.

***B. subtilis*—nanoparticle exposures.** The effect of TiO₂ NPs on *B. subtilis* in a bicarbonate lysing buffer (5 mM NaHCO₃, pH 7.7) was studied under five different NP exposure conditions: 0, 1, 10, 50, and 100 ppm. All trials were done in the dark to prevent reactive oxygen species generation. A volume of 1 mL washed *B. subtilis* culture (10⁸ CFU/mL) was added to 9 mL of TiO₂ NP suspension to reach desired TiO₂ NP concentrations. The exposed *B. subtilis* were incubated at 25°C in 20 mL glass culture tubes while being shaken. After 1, 2, 4, and 8 h of incubation, 0.3 mL of each suspension was removed for analysis. Viable cell concentrations were determined by plating and counting colony-forming units (CFU) on LB agar (1.5%). Each treatment was performed in triplicate.

Subsequently, using the same conditions described above, TiO₂ NPs were added at three different time points after *B. subtilis* was washed and suspended in lysing buffer. First, 1 mL of washed *B. subtilis* culture (10⁸ CFU/mL) was added to three different reactors containing 9 mL of lysing buffer with no TiO₂ NPs. Next, TiO₂ NPs were added to the 3 independent culture tubes (final concentration of 50 ppm TiO₂) at 0, 30, and 60 minutes, respectively. Aliquots of 0.3 mL were sampled and viable cell concentrations were determined via CFU plating as described above. Each treatment was performed in triplicate.

Membrane potential ($\Delta\Psi$) and proton gradient (ΔpH). The membrane potential ($\Delta\Psi$) and proton gradient (ΔpH) of *B. subtilis* cells was determined by the distribution of 3,3'-dipropylthiadicarbocyanine iodide (DiSC₃(5)) between cells and the suspending medium as described earlier.⁹⁵ Due to the compensatory interaction between the transmembrane ΔpH and $\Delta\Psi$, a decrease in fluorescence is an indication of ΔpH dissipation.⁹⁶ The interaction between $\Delta\Psi$ and ΔpH that governs the PMF is described as:

Equation 2-2

$$PMF = \Delta\Psi - \frac{2.3RT}{F} \Delta\text{pH}$$

where R is the gas constant, F is the Faraday constant, and T is temperature.

An overnight culture of *B. subtilis* was grown and harvested as described above being resuspended in 30 mL of lysing buffer with either 0 or 50 ppm of TiO₂ NPs. Immediately after the final resuspension, 3 mL of cell suspension was added to a quartz cuvette. 1 μL of 3 mM DiSC₃(5) dissolved in DMSO was added to the cuvette, capped, and shaken by hand. The suspension was then monitored for fluorescence (Horiba Fluoromax-4 using FluorEssence software) at excitation wavelength 643 nm, slit width 4 nm, and emission wavelength 666 nm, slit width 4 nm. The fluorescence was monitored for 1 hour at intervals of 0.5 seconds with an integration time of 0.1 seconds. The emission signal from the photomultiplier tube was corrected by dividing by the reference signal from photodiode detector, which measures the output of the xenon lamp. Counts were kept below 2 million counts per second, as the detector is not linear over this count rate (Personal communication with Horiba technicians).

Hyperspectral microscopy. The NP interactions with *B. subtilis* were assessed using an enhanced resolution dark-field microscope system (BX51, Olympus, USA) equipped with CytoViva Hyperspectral Imaging System (HSI, Auburn, AL). 20 μL of sample was deposited on a clean glass slide and covered with a coverslip for imaging. Hyperspectral images were acquired using 100% light source intensity and 0.6 s acquisition time per line. Each pixel of the hyperspectral image contains a light reflectance spectrum, ranging from 400 to 1000 nm with a spectral step of 1.5 nm. Each pixel thus has a spectral signature modulated by the nature of the material it contains.⁹⁷

A spectral pre-library of TiO₂ NPs was build using hyperspectral images of TiO₂ NPs in lysing buffer (100 ppm). The pixels comprising endmembers hyperspectral signal were identified and grouped into the *TiO₂ NPs pre-library*, following steps previously described by

Badireddy and collaborators.⁹⁷ The specificity of the pre-library was assessed by mapping it on negative control images (abiotic lysing buffer and non-exposed cells in lysing buffer). Spectra in the pre-library that matched spectra of pixels in the negative control hyperspectral images were considered as unspecific false positives and removed from the pre-library. The remaining spectra built the final *TiO₂ NP library*, containing specific hyperspectral *TiO₂ NP* signature (**Figure 2-3**). This NP library was mapped on hyperspectral images (*B. subtilis* exposed to 0, 1 or 100 ppm during 1 hour in lysing buffer as described in the *Preparation of cell cultures* section above) to assess NPs–cells interactions. The mappings of the NPs pre-library and library was processed using a Spectral Angular Mapping algorithm (SAM, ENVI 5.2 software, in short, an algorithm comparing angles between vectors), whereby two vectors (*i.e.* spectra bands) with angles ≤ 0.09 rad were considered as similar. Pixels containing the NPs spectral signature were labeled with a chosen color of red. This method has already been tested and validated for bacteria–NP interaction.⁹⁸

Preparation of autolytic cell wall extracts. Cell wall associated autolysins and associated enzymes were extracted according to the method developed by Brown.⁹⁹ Briefly, *B. subtilis* strain was inoculated and maintained in LB Miller medium overnight before 2 liters of fresh LB medium was added and incubated for 12 hours until the cell concentration reached 10^8 CFU/ml. The cell suspension was further concentrated by centrifuging at 6000g for 10 min to a final concentration of 5% (wet weight) in 0.75% NaCl. The concentrated cell suspension was centrifuged once more at 6000g for 10 min. The supernatant was discarded and the pellet was resuspended in 2 L of 2 M LiCl solution. After one-hour of incubation at 4°C, the suspension was centrifuged at 16,000g for 15 min and the pellet was discarded. The cell-associated autolysin extracts were resuspended in the supernatant and stored at 4°C for further experimentation.

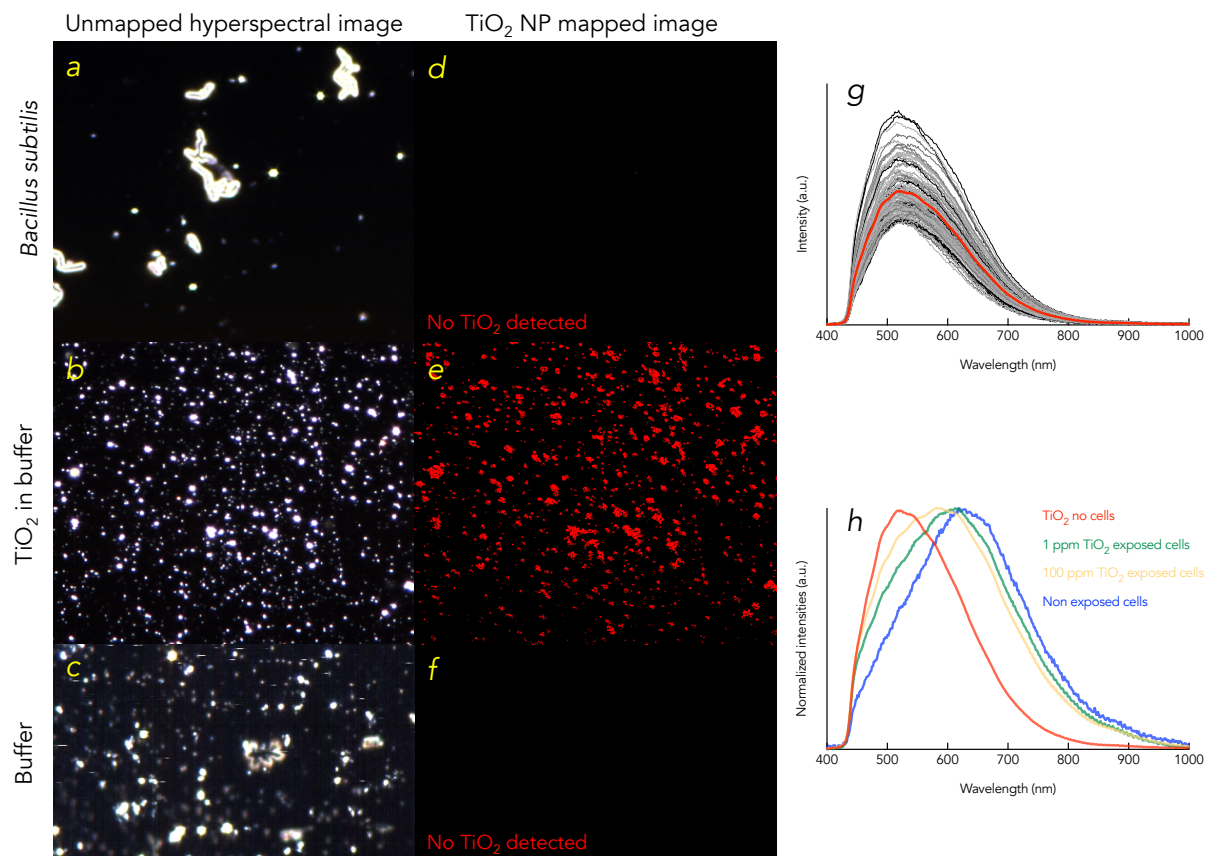


Figure 2-3. Unmapped (a-c) and mapped (d-f) images of *B. subtilis* (10^6 cells/mL), TiO₂ nanoparticles suspended (100 ppm) in buffer, and 5 mM bicarbonate buffer. All red pixels have spectral signatures identical to those in the spectral library (g). The red profile in (g) highlights the average spectral profile of the TiO₂ NP library. (h) Shows a shift in cell wall spectral profile; as more TiO₂ is present in the sample, the more the cell wall spectral profile shifts to the left, towards the average spectral profile of the TiO₂ NP library.

Adsorption of autolysins and peptidoglycan degradation. An autolysin extract isotherm on TiO₂ NPs was measured by the solution depletion method, in which any protein concentration change, ΔC_w , in the bulk solution prior to and after exposure to TiO₂ NPs was attributed to adsorption to the surface:

Equation 2-3

$$\Gamma = \Delta C_w V / A$$

where Γ is the mass of protein adsorbed per surface area unit, V is the volume of the bulk solution, and A is the TiO₂ NP surface area available for adsorption, calculated using the hydrodynamic radius and assumed spherical shape.¹⁰⁰

1 mL reactors were prepared by adding varying concentrations of TiO₂ NPs in the range of 0–10,000 ppm to 55 mg/L of autolysin extract in lysing buffer. The suspensions were

immediately capped and rotated for 24 hours in the dark at 25°C. The samples were then centrifuged at 16,000g for 15 min to remove TiO₂ NPs and any TiO₂-adsorbed protein from the bulk solution. A portion of the supernatant was pipetted off and analyzed for protein concentration using the Pierce BCA assay Kit with BSA as the protein standard. The remaining portion of the supernatant (0.5 mL) was incubated with 1.5 mL of purified *B. subtilis* peptidoglycan (purchased from Sigma-Aldrich) to study the digestion process of peptidoglycan. The change in peptidoglycan concentration was monitored by measuring absorbance at 450 nm over time via a Cary 300 Bio UV-Visible Spectrometer/Cary WinUV software at room temperature.

DNA and L-alanine concentration. Extracellular double-stranded DNA (dsDNA) was monitored using a PicoGreen dsDNA Kit (Molecular Probes, Invitrogen) coupled with a fluorometer (VersaFluor Fluorometer, Bio-Rad) following the suppliers' protocol. Two *B. subtilis* growth conditions were used to create standard curves: a positive control using liquid minimal Davis (MD) medium, and a negative control using lysing buffer. Cells were grown in MD medium because of its ability to keep *B. subtilis* cells vegetative. 0.2-0.3 mL samples were taken from each reactor at 0, 1, 2, 4, 8, and 12 hrs. Each sample point was diluted, with a portion being plated for CFUs, and 0.1 mL was used to determine dsDNA concentration. Cell suspensions were diluted to within the detection concentration of the PicoGreen dsDNA Kit (25 pg to 1 µg of dsDNA/mL). 0.1 mL of the kit reagent was added to 0.1 mL diluted sample and incubated in a glass cuvette at 25°C for 3–4 min before being placed in a fluorescence reader with excitation at 480 nm and emission at 520 nm. L-alanine was monitored using an abcam L-Alanine Assay Kit according to the manufacturers protocol.

Gene expression. To capture the influence of TiO₂ NPs on *B. subtilis* gene expression, reverse transcription quantitative polymerase chain reaction (RT-qPCR) was used to detect RNA fold changes. Three genes were chosen for analysis: *skfA*, *sdpC*, and *lytC*; *rpoB* was

used as an internal reference for normalization. Cells were grown, washed, and exposed as described in the *Preparation of cell cultures* section above. The washed cells were then exposed to either 100 ppm TiO₂ NPs or no TiO₂ NPs. Samples for RNA extraction were taken both right before exposure, $t=0$, and one hour after exposure, $t=1$ hr.

Total cellular RNA was extracted using a Qiagen RNeasy Mini Kit according to the manufacturer's instructions. Purified RNA was verified by quantification using a Qubit 2.0 Fluorometer according to the Qubit RNA HS Assay Kit manufacturer protocol. Extracted RNA was then used as a template to synthesize first-strand complimentary DNA (cDNA) using an iScript cDNA Synthesis Kit according to the manufacturer's instructions and using a (BIO RAD MyCycler) thermal cycler set at 25°C for 5 minutes, 42°C for 30 minutes, 85°C for 5 minutes, and a holding temperature of 4°C. Real-time PCR amplification of the cDNA was done using a Applied Biosystems 7500 Real Time PCR System. Primers used for PCR were designed using Integrated DNA Technologies PrimerQuest (

Table 2-1). Each 20 μ L PCR mixture contained H₂O (6.5 μ L), forward primer (1 μ L), reverse primer (1 μ L), probe (0.5 μ L), Taqman master mix (10 μ L), and DNA sample (1 μ L). The amplification program was set to 50°C for 2 minutes (1 rep.), 95°C for 10 minutes (1 rep.), 95°C for 15 seconds (40 reps.), and 56°C for 1 minute. The *rpoB* gene was used as a reference for data normalization. All the samples were analyzed in triplicate.

Table 2-1. Gene specific primer and probe sequences used for RT-qPCR.

Gene	Forward	Reverse	Probe
<i>skfA</i>	CGATTGTGAAAGCTGCTG	ACACGTGTCATAGCAATACT	/56-FAM/ATGGGCTGT/ZEN/TGG GCCTCGAA/3IABkFQ/
<i>sdpC</i>	AACGCAGTTGCATTACAAA	AGC AGC CGC TTC TAA AT	/56-FAM/TGC AGT TGT /ZEN/TAC TGC GGC AGC /3IABkFQ/
<i>lytC</i>	CAGCTACCCTGACTCTATTG	TAC GGG CTC CTG TAG ATA A	/56-FAM/CAG GAG CTA /ZEN/CAC TGG CAG CT/3IABkFQ/
<i>rpoB</i>	CCAAGGTACGTGCTACAA	AGT TCA CCA AGC TCC ATA G	/56-FAM/AGC GTC CGA /ZEN/TCG TAA GTG TCG G/3IABkFQ/

Results and Discussion

Exposure of *Bacillus subtilis* to TiO₂ NPs in bicarbonate lysing buffer, under dark conditions, resulted in a negative correlation between NP concentration and loss of viable cell counts over time (**Figure 2-4**). In the absence of NPs, the number of viable cells decreased by over 2.5 orders of magnitude in the first hour followed by 3 orders of magnitude loss over the next 7 hours (over a 5-log drop over the 8 hours monitored). A similar loss in cell viability was observed in the presence of 1 ppm of TiO₂ NP. However, in the presence of 10 ppm TiO₂ NPs, total viable cell counts decreased by less than 2 orders of magnitude over 8 hours. Viable cell counts further increased after exposure to TiO₂ NPs at 50 and 100 ppm. The difference between 50 ppm and 100 ppm exposures is significant at the 8-hour time point and might be explained by a biphasic response common in toxicity response curves, where the 50 ppm range would be in the hormetic zone. Overall, exposure of *B. subtilis* to a nutrient-limited buffer of bicarbonate induced autolysis of cells, and that cell lysis was blocked by the presence of TiO₂ NP in a dose-dependent manner.

The observation of cell lysis in nutrient-limited buffer agrees with previous findings that such solutions cause the onset of autolysis in *B. subtilis*.⁷⁷ Under nutrient poor conditions, a collapse of the proton-motive force (PMF) in *B. subtilis* leads to a conformational change in associated teichoic acids and thus an activation of autolytic enzymes that digest the surrounding peptidoglycan.^{77,101,102} For this reason, the membrane potential ($\Delta\Psi$) and proton gradient (ΔpH) of *B. subtilis* in lysing buffer were monitored using DiSC₃(5) fluorescence. Apparent equilibration of the fluorescence signal between cells and the buffer, as indicated by a flat line in the fluorescence profile, took approximately 40 minutes. Ten minutes after fluorescence stability was reached (50 minutes after suspension in lysing buffer in the absence of TiO₂ NPs), the fluorescence signal decreased before increasing 60 fold (**Figure 2-5**). The slight decline and then sharp rise in fluorescence in the no TiO₂ control indicates the collapse

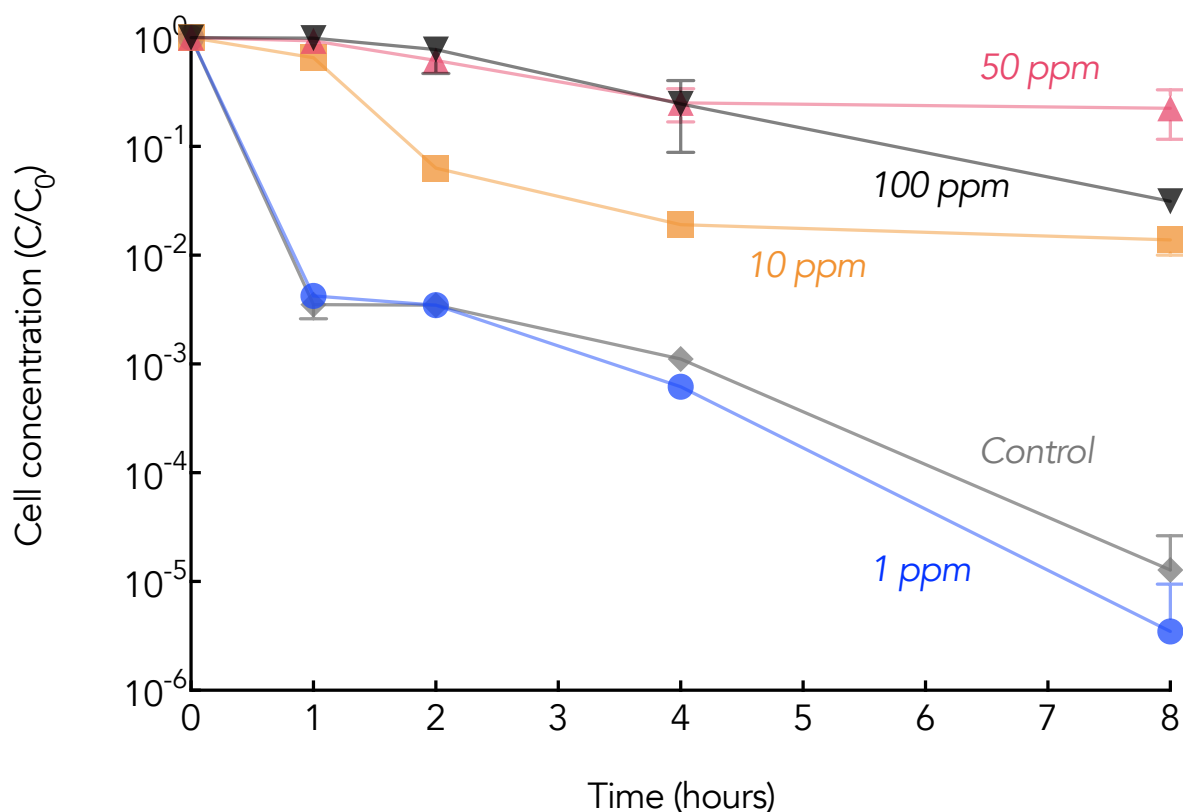


Figure 2-4. Colony Forming Unit (C) over time normalized to the initial Colony Forming Unit of each series (C_0) of *B. subtilis* in 5 mM NaHCO₃ buffer (pH 7.7) with exposure to various concentrations of TiO₂ NPs, and a no TiO₂ NP control in the absence of light. Each point represents the mean ($n=3$) with error bars representing the 95% confidence interval.

of the membrane potential. The dip in $\Delta\Psi$ in the no TiO₂ control is an indication of an increase in the membrane potential, which is likely the result of the dissipation of the membrane pH gradient due to the compensatory relationship between membrane pH and membrane potential (**Equation 2-2**).⁹⁵ When *B. subtilis* cells were suspended in lysing buffer in the presence of 50 ppm TiO₂ NPs, minimal change in $\Delta\Psi$ occurred over the same time period, indicating that the membrane potential, and pH gradient, remains intact. It is possible that the mode of prevention arises from the direct interaction between TiO₂ NPs and the outer layer of wall teichoic acids that make up the bacteria-nanoparticle interface.

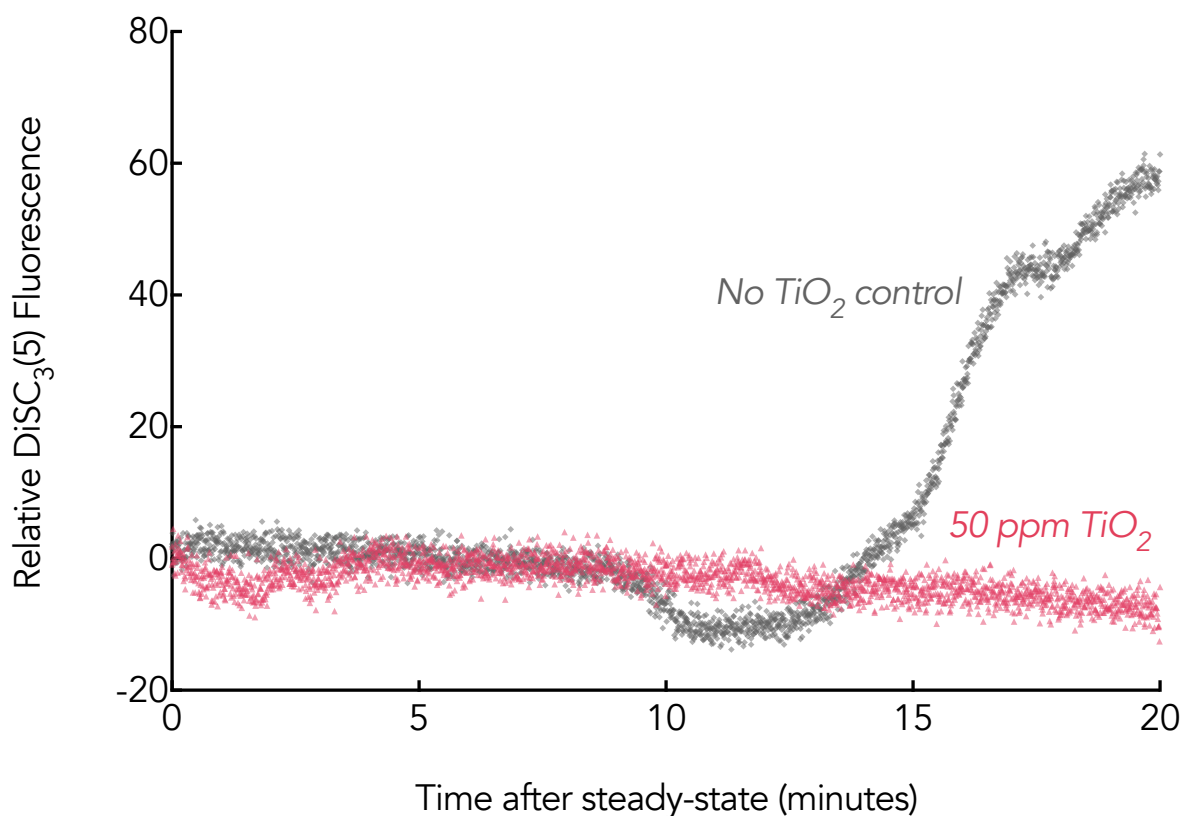


Figure 2-5. Fluorometry assay of DiSC₃(5) stained *B. subtilis* cultures in 5 mM NaHCO₃ in the presence of 50 ppm TiO₂ NPs and absence of TiO₂ NPs in the dark. Depolarization of *B. subtilis* membrane was monitored by measuring the fluorescence intensity at an excitation and emission wavelength of 643 nm and 666 nm, respectively, for 1 hour. Apparent equilibrium DiSC₃(5) between the cell membrane and the media, as indicated by a flat-line in fluorescence, took 40 minutes.

Hyperspectral imaging (HSI) was performed on cultures of *B. subtilis* exposed to TiO₂ NPs to visualize TiO₂ NPs–cell interactions (**Figure 2-6**). HSI confirmed that at higher concentrations of TiO₂ (100 ppm), the TiO₂ spectral signature was consistently found to be associated with the surface of individual cells (**Figure 2-6e2,f2,g2**) and bright dots we suspect to be TiO₂ aggregates. Moreover, at 100 ppm TiO₂ exposure, cells existed exclusively as individual, or short chained, planktonic cells (**Figure 2-6e1,f1,g1**). These *in vivo* visualizations of TiO₂ deposition on *B. subtilis* cell walls support previous *in vitro* findings which teichoic acids attached to TiO₂ surfaces.^{73,81} At the experimental pH of 7.7, the surface of TiO₂ is negatively charged (-41.3 mV), which would support electrostatic interactions between NP surface and positively charged alanine groups, as reported previously.⁸¹ It is possible that the protons on the surface of metal oxide NPs may change the microenvironment

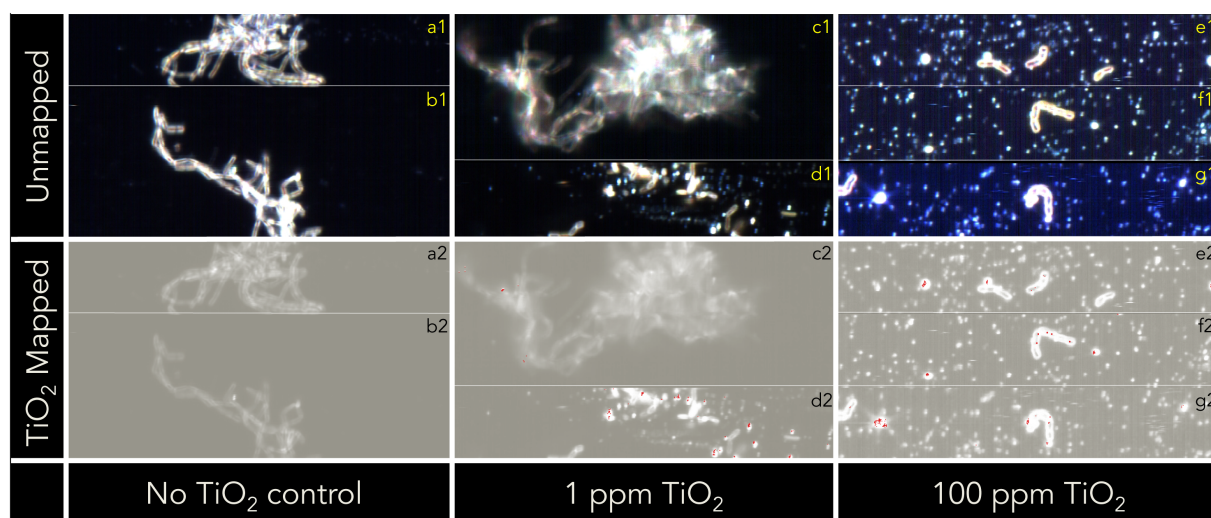


Figure 2-6. Unmapped (a1-g1) and TiO₂ mapped (a2-g2) images of *B. subtilis* (10⁷ cells/mL) exposed to 0 (a, b), 1 ppm (c, d), and 100 ppm (e-g) TiO₂ NPs suspended in bicarbonate buffer (5 mM). Red pixels have spectral signatures identical to those in the TiO₂ NP spectral library. Figures with the same alphabetical identifier, e.g. a1 and a2, are identical images, however, a2 is mapped to identify TiO₂ location, whereas a1 is left unmapped.

of the D-alanyl ester and teichoic acid interaction, affecting the activation of autolysin considering it has been demonstrated that the adsorption of a metal oxide surfaces influence the D-alanyl ester and teichoic acid interaction.⁷³ Therefore, a potential hypothesis for the disruption of autolysis by TiO₂ NP is that association between NP surfaces and cell surface proteins gives rise to a conformational change in the surface proteins that regulate autolytic activity.

A kinetic assessment of cell lysis was performed in which NPs were added before and after the apparent PMF collapse. 50 ppm of TiO₂ NPs was dosed into cultures at 0, 30 and 60 minutes after the cells were suspended in lysing buffer (**Figure 2-7**). Adding TiO₂ NPs immediately (t=0) after exposure of cells to lysing buffer led to a ~0.5-log decrease in cell counts after 8 hours. Adding TiO₂ NPs 30 minutes after exposing cells to lysis buffer stabilized cell viability for the following 7.5 hours. When dosed at 60 minutes, after the observed PMF collapse, the following 7 hours saw a log drop in cell viability.

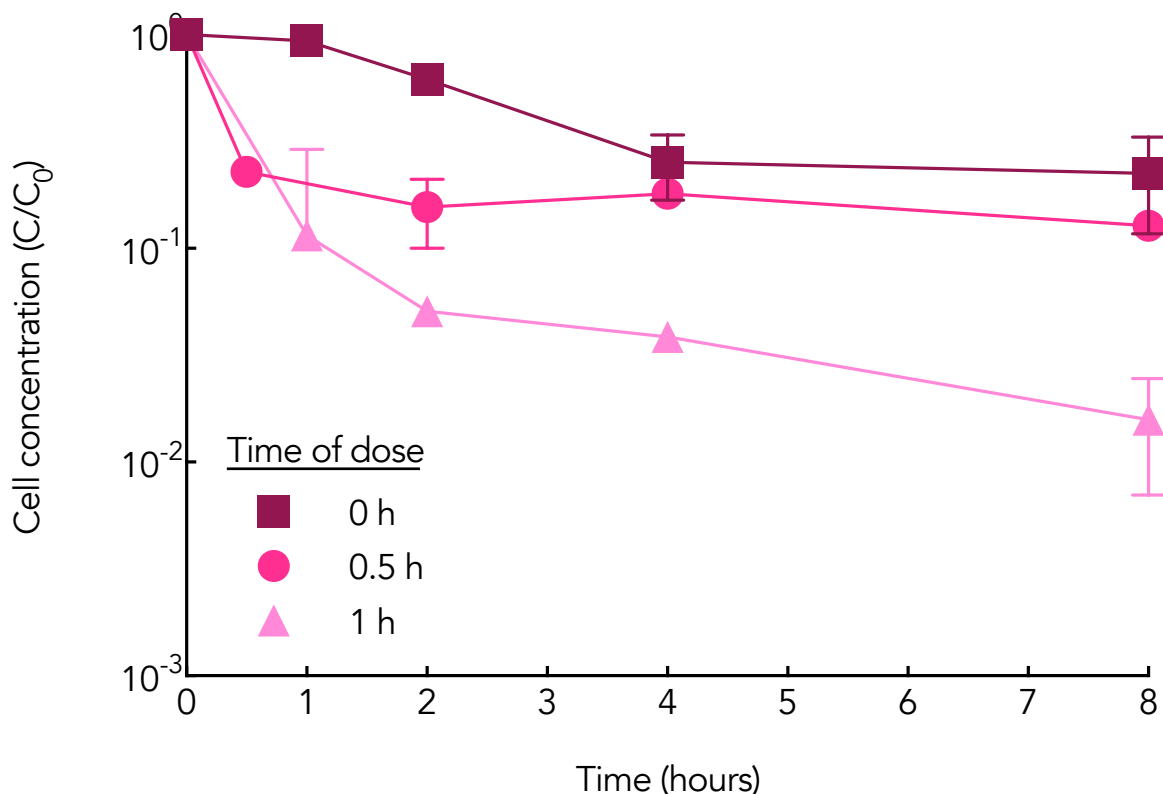


Figure 2-7. Colony Forming Unit (C) over time normalized to the initial Colony Forming Unit of each series (C_0) of *B. subtilis* in 5 mM NaHCO_3 buffer (pH 7.7) with the addition of 50 ppm TiO_2 NPs at time points of 0 hour, 0.5 hour, and 1 hour in the absence of light. Each point represents the mean ($n=3$ or 2) with error bars representing the standard deviation.

The observation that cell viability was maintained with higher efficiency when TiO_2 was added before the PMF dissipation suggests that the release of active autolysins from cells that have already undergone autolysis may contribute to lysis of neighboring cells, and led us to consider another potential mechanism by which TiO_2 NPs may interfere with a population undergoing autolysis: by adsorbing released autolysins from cells that have already lysed, limiting cell lysis proliferation. To test this, an adsorption isotherm was first produced for autolysins on TiO_2 NPs (pH 7.7 and 25°C, **Figure 2-8a**). The autolysin extracts showed a binding affinity to TiO_2 NPs, reaching a surface concentration of 1 mg/m² (or 0.18 mg/mg TiO_2). In a follow-up experiment to assess the functional activity of lytic enzymes after incubation with TiO_2 NPs, autolysin extracts were exposed to varying concentrations of TiO_2 NPs before being assayed for their ability to degrade peptidoglycan, the natural substrate of

autolysins (**Figure 2-8b**). Peptidoglycan degradation was inversely related to the concentration of TiO₂ NPs present. After 5 hours, concentrations of peptidoglycan decreased by 29% and 57% when autolysins were incubated with 50 and 100 ppm TiO₂ NPs, respectively. In the negative control (no autolysin), peptidoglycan decreased by 0.3 mg/L over 5 hours, whereas in the positive control (autolysins without TiO₂ NP incubation), peptidoglycan was degraded by more than 1.2 mg/L over the same time period.

Generally, the degree of protein adsorption to NPs, and subsequent functionality, depends on both the NP surface and the protein's folding structure, charge, and polydispersity.¹⁰³ Protein adsorption to, and unfolding on, NPs can occur rapidly, within minutes of incubation.¹⁰⁴⁻¹⁰⁶ The adsorption capacity of cell wall autolysin extracts to TiO₂ NPs (**Figure 2-8a**), and subsequent loss of peptidoglycan-degrading ability (**Figure 2-8b**), could contribute to the hydrophobicity of the autolysin extracts. It has been suggested that extracted autolysins may be linked to other membrane bound lipids of acids, implying hydrophobic properties.¹⁰⁷ Although protein structure analysis was not part of this work, and thus coming to a conclusion on the forces governing adsorption was not appropriate, the loss of functionality to digest peptidoglycan was correlated to the concentration of TiO₂ incubated with the autolysins. These results are similar to a previous study by Xu et al. (2010) which demonstrated a change in structure and loss of functionality in lysozymes after incubation with TiO₂ NPs.⁷⁴

Supplementing the adsorption and peptidoglycan digestion assay results was the observation that the detectable TiO₂ deposition at 1 ppm TiO₂ exposure was associated with the large sticky aggregations of extracellular matter (**Figure 2-6c1-d2**), where it is reasonable to believe starved cells are exuding general stress proteins and cytoplasmic material due to autolysis, leading to an accumulation of autolysins. At lower concentrations of NP exposure (1 ppm TiO₂) there was no observable TiO₂ deposition on cell walls (**Figure 2-6c2,d2**). Of the

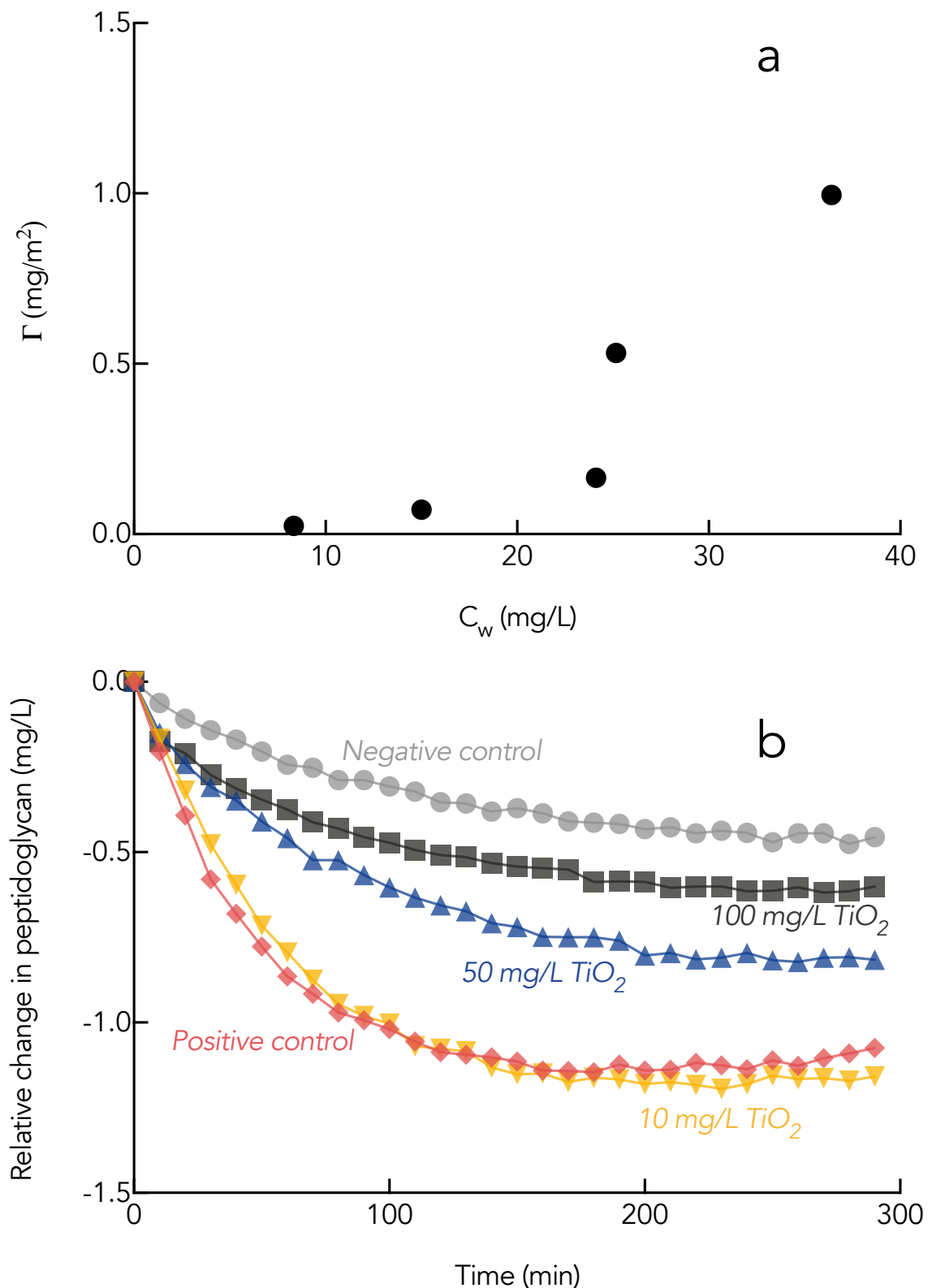


Figure 2-8. (a) Adsorption isotherm of autolysins on TiO_2 NPs (pH 7.7 and 25°C) with the surface area concentration, Γ , plotted against the concentration of free enzyme in solution, C_w . (b) Relative change in in peptidoglycan over time after incubation with autolysins. Prior to exposure to peptidoglycan, autolysins were incubated with varying concentrations of TiO_2 NPs. The *Negative control* peptidoglycan was not exposed to any cell wall associated enzymes. The *Positive control* peptidoglycan was exposed to autolysins that were not incubated with TiO_2 NPs.

very few individual planktonic cells in the 1 ppm TiO₂ exposure, TiO₂ was not mapped on any of them (contrary to HIS visualizations at 100 ppm TiO₂).

Overall, the results suggest two potential mechanisms for the disruption of autolysis by TiO₂ NP in a concentration dependent manner: (1) directly, through TiO₂ NP deposition on the cell wall, delaying the collapse of the PMF and preventing the onset of autolysis (Depicted in **Figure 2-9a**); and (2) indirectly, through adsorption of autolysins on TiO₂ NP, limiting the activity of released autolysins and preventing further lytic activity (Depicted in **Figure 2-9b**).

Finally, as *B. subtilis* may form spores, it was also important to consider that the loss of viable cell counts could be due to cannibalism and spore formation, rather than, or in addition to, autolysis. Aliquots of *B. subtilis* cultures, 12 hours after suspension in lysing buffer, were removed and inoculated to fresh LB media where endospore germination could occur.¹⁰⁸ No growth was observed. *B. subtilis* are not known to form endospores when rapidly deprived of essential nutrients from the system³², as was done in this work. Additionally, spore formation takes 8 hours to complete¹⁰⁹, at which time DNA is released by the mother

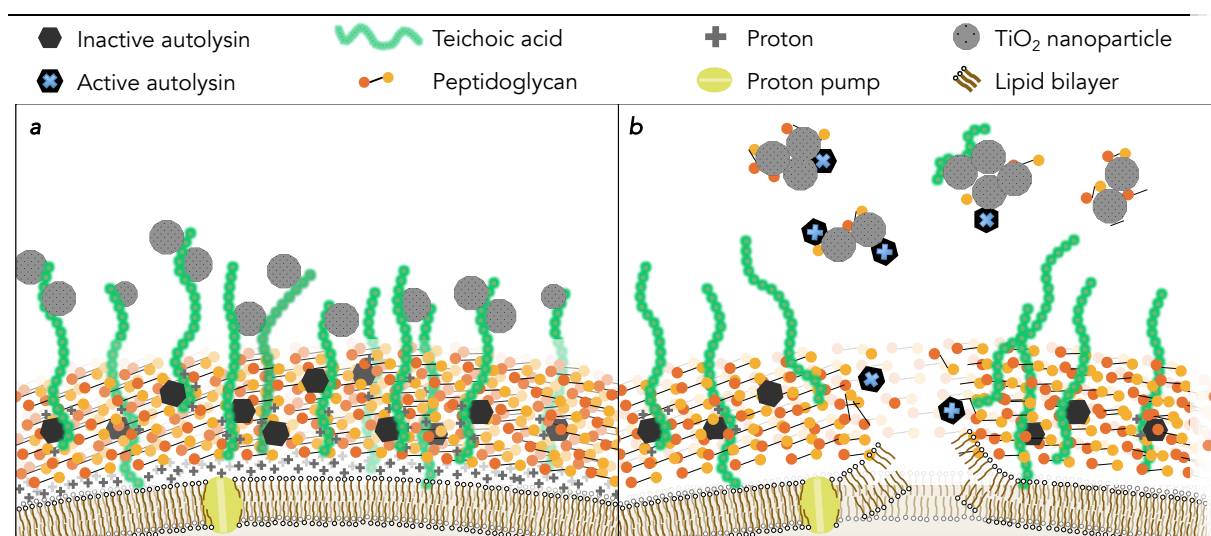


Figure 2-9. Proposed mechanisms for disruption of autolysis in *B. subtilis* in the presence of TiO₂ NPs. (a) TiO₂ NPs associate with the region of cell wall teichoic acids that make up the point of contact between the cell and NPs, altering autolysin activity and maintaining the PMF under nutrient limited conditions. (b) Once a cell has undergone autolysis, the released autolysins are adsorbed by TiO₂ NPs, which diminishes the peptidoglycan-degrading functionality, limiting enzymatic attack of peptidoglycan of other population members.

cell. After 4 hours in the lysing buffer, the supernatant dsDNA concentration was over an order of magnitude higher than that in the maintenance medium (**Figure 2-10a**). There was an inverse relationship between dsDNA concentration and CFUs. CFUs in the MD media had less than a 5% variation over the 12-hour monitored time period. In addition to dsDNA concentration, the release of L-alanine, one of the major components of peptidoglycan, was also monitored (**Figure 2-10b**). L-alanine is released into the extracellular environment when *B. subtilis* undergo autolysis.¹¹⁰ L-alanine concentrations increased by a factor of three after 24 hours of suspension in lysing buffer. Cultures exposed to the lysing buffer were also examined in TEM micrographs and HSI; spores were not present. Furthermore, spore formation in *B. subtilis* is preceded by cannibalism, which is preceded by the expression of two main operons, sporulation killing factor (*skf*) and sporulation delay factor (*sdp*), in a process dubbed cannibalism.^{29,111} Within these operons, there are two genes, *skfA* and *sdpC*, that are known to express lytic peptides responsible for lysing nonsporulating sister cells. The expression of these genes was monitored to determine if cannibalistic protein production was responsible for the loss of cell viability in cells suspended in lysing buffer, and to identify if TiO₂ NPs had an influence on the genes expressed during cannibalism. After one hour of suspension in lysing buffer, there was less than a 1.5 fold increase of *skfA* and *sdpC* (**Figure 2-11**). Furthermore, there was no significant difference in *skfA* or *sdpC* gene expression between cultures suspended in lysing buffer in the presence (50 ppm) or absence of TiO₂ NPs. In addition to *skfA* and *sdpC*, the expression of *lytC* was also monitored. The *lytC* gene is responsible for producing a major autolysin, LytC, and is located throughout the vegetative cell wall.¹¹² As with the cannibalistic genes, there was no significant difference in *lytC* expression between *B. subtilis* suspended in lysing buffer in either the presence or absence of TiO₂ NPs, revealing that TiO₂ NP were not interfering with expression of autolytic genes. Based upon these analyses, complete loss of cell viability was attributed to autolysis.

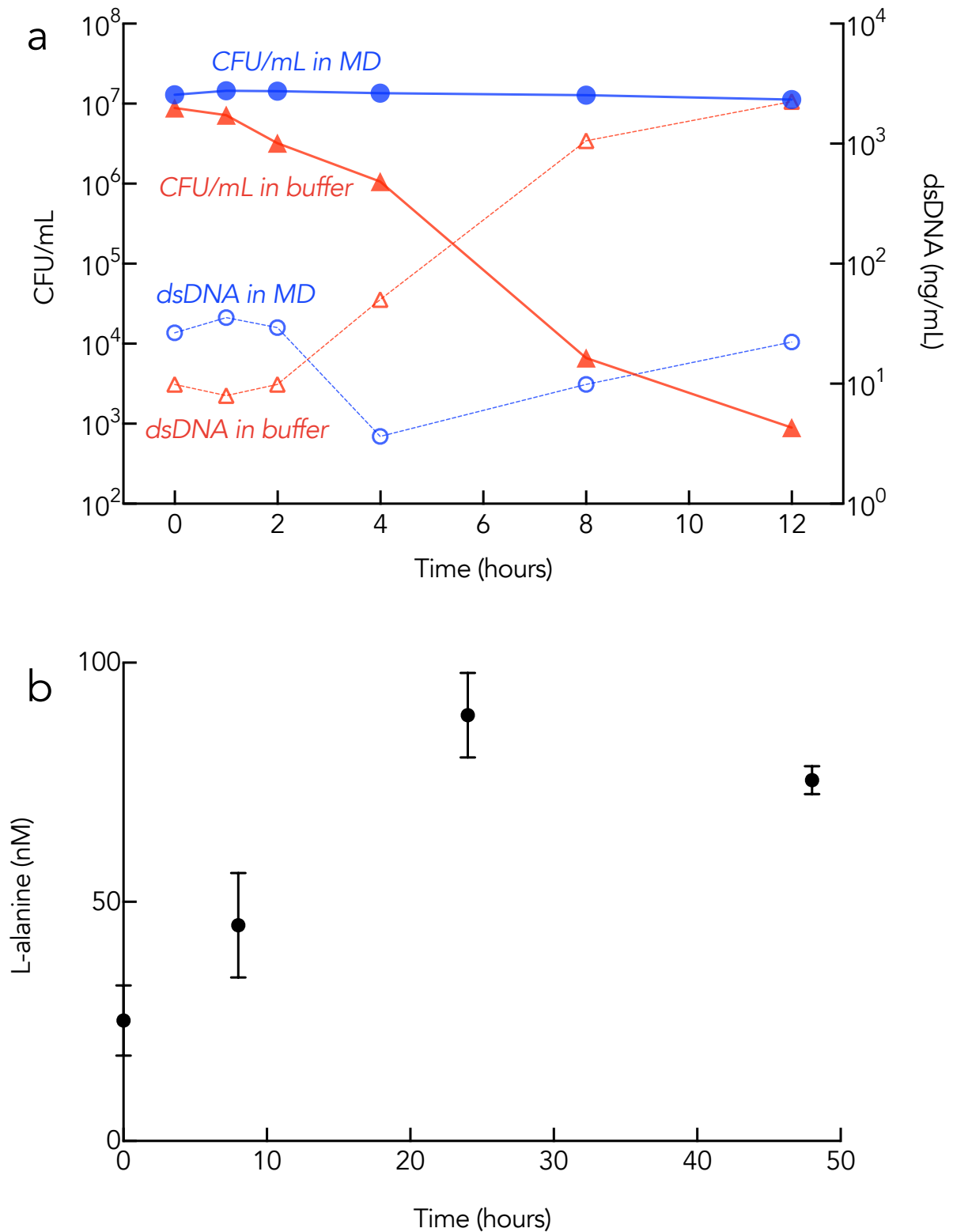


Figure 2-10. (a) *B. subtilis* growth (CFU/mL) and released double-stranded DNA (dsDNA) in minimal Davis media (blue) and 5 mM NaHCO₃ (red) over time. (b) L-alanine concentration measured in the supernatant of *B. subtilis* suspended in 5 mM NaHCO₃. Each point represents the mean ($n=3$) and error bars represent standard deviation.

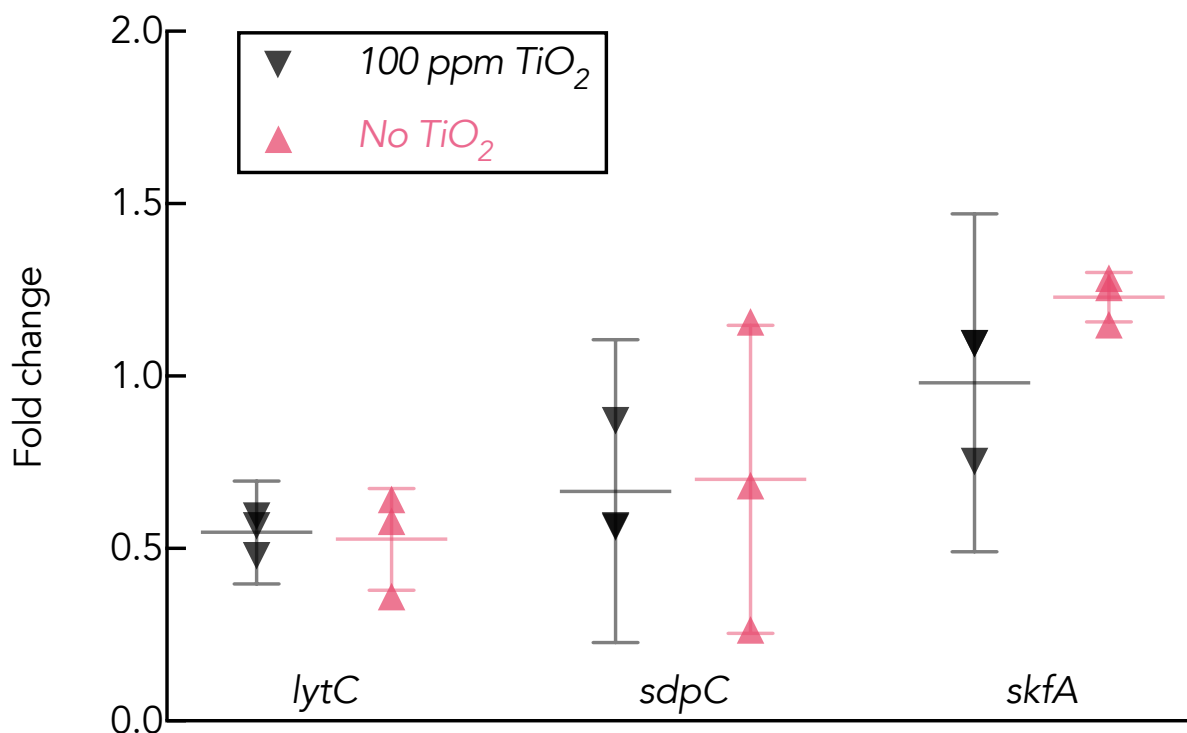


Figure 2-11. Expression (fold change relative to *rpoB*) of RNA encoding for *lytC*, *sdpC*, and *skfA* in cultures of *B. subtilis* after 1 hour of suspension in 5 mM NaHCO₃ in the presence or absence of TiO₂ NPs. Individual data points are plotted; thick bars represent the mean ($n=3$) and error bars represent the standard deviation.

Conclusions

Exposure of *B. subtilis* to a nutrient-limited buffer of bicarbonate induced autolysis in the population. Exposure of nutrient-limited cultures of *B. subtilis* to TiO₂ NPs appeared to prevent the propagation of autolysis in the population and enabled the cultures to survive nutrient stress that otherwise results in a decline of population numbers. TiO₂ NPs prevented, or at least delayed, the dissipation of the PMF. It is possible that the mode of prevention arises from the direct interaction between TiO₂ NPs and the outer layer of wall teichoic acids that make up the bacteria-nanoparticle interface. Hyperspectral imaging supported this hypothesis by revealing that high concentrations of TiO₂ NPs (100 ppm) was correlated with a decrease in cell aggregation and an increase in TiO₂ deposition on the cell wall. Additionally, results indicated that released autolysins might lose peptidoglycan-degrading functionality after adsorption to TiO₂ NP surfaces. Overall, the results suggest two potential mechanisms for the

disruption of autolysis and cell death by TiO₂ NP in a concentration dependent manner: (1) directly, through TiO₂ NP deposition on the cell wall, delaying the collapse of the PMF and preventing the onset of autolysis; and (2) indirectly, through adsorption of autolysins on TiO₂ NP, limiting the activity of released autolysins and preventing further lytic activity.

The disruption of autolysis in *B. subtilis* cultures by TiO₂ NPs, suggests the mechanisms and kinetics of cell death may be complicated by metal-oxide surfaces, which are abundant in nature. Furthermore, the association of nanoparticles to *B. subtilis* and autolytic enzymes may not be confined to metal oxides, but rather be linked to surface chemistry of the particle, such as surface charge (See Appendix A: Additional nanoparticle–bacteria interactions, **Figure A-8**).²⁰ Therefore, a variety of materials and surfaces may influence autolysis, especially in natural systems such as groundwater where surfaces are abundant. If metal-oxide NPs delay autolysis through cell-wall associated protein interactions and/or limit the proliferation of autolysins via adsorption, as suggested with the results of the this study, the potential for NP to interfere with other cell-wall mediated interactions and extracellular signaling molecules should be explored. For example, disruption of autolytic activity may have an impact on growth-phase activity as autolysins in *B. subtilis* are involved in more controlled processes such as cell-wall turnover, cellular division, sporulation, cannibalism, and biofilm formation.¹¹³ The ability to fine-tune the interactions between cells and nanoparticles through coatings that alter the electrosteric and electrostatic properties of particles suggests that the interference of cellular process using colloidal principals and engineered nanomaterials may also be fine-tuned.

3. Quorum sensing signals form complexes with cations[‡]

Abstract

Quorum sensing (QS) regulates important bacterial behaviors such as virulent protein production and biofilm formation. QS requires that molecular signals are exchanged between cells, where extracellular environmental conditions influence signal stability. In this work, we present a novel complexation between metal cations (Ag^+ and Cu^{2+}) and a QS autoinducer signal (*N*-hexanoyl homoserine lactone, HHL). The molecular interactions were investigated using mass spectrometry, attenuated total reflectance-Fourier transform infrared spectroscopy, and computational simulations. Results show that HHL forms predominantly 1:1 complexes with Ag^+ ($K_d = 3.71 \times 10^{-4}$ M) or Cu^{2+} ($K_d = 1.78 \times 10^{-5}$ M), with the coordination chemistry occurring on the oxygen moieties. *In vivo* experiments with *Chromobacterium violaceum* CV026 show that sublethal concentrations of Ag^+ and Cu^{2+} decreased HHL-regulated QS activity. Furthermore, when Ag^+ was preincubated with HHL, Ag^+ toxicity to CV026 decreased by an order of magnitude, suggesting HHL:metal complexation alters the bioavailability of the individual constituents.

Introduction

Quorum sensing (QS) in bacteria is responsible for the regulation of a remarkably wide range of coordinated behavior including biofilm formation, pathogenicity, and CRISPR-Cas adaptive immunology.^{40,43,114} During QS, individual bacterial cells detect their local population density and coordinate gene expression in response to endogenously synthesized

[‡]This chapter is currently under peer-review for publication as: McGivney, E., Jones, K., Weber, B., Valentine, A., VanBriesen, J. M., Gregory, K. B., “Quorum sensing signals form complexes with Ag^+ and Cu^{2+} cations.” in *ACS Chemical Biology* (as of 1/9/2018).

chemical signals known as autoinducers. A commonly studied class of autoinducers in gram-negative bacteria are acyl-homoserine lactones (AHL).¹¹⁵ AHLs are synthesized internally via a member of the LuxI protein family, and diffuse between the cytoplasm and external environment. Once a threshold concentration of AHL is reached in a cell's local microenvironment, a LuxR receptor-protein complex, activated by AHL binding, regulates gene expression (**Figure 1-1**). Thus, activities regulated by QS are directly dependent upon the concentration and structure of AHLs outside of the cell, and understanding environmental conditions that affect AHL stability is important in natural, engineered, and human health systems.

Several studies have identified environmental factors that influence the stability of AHLs (reviewed by ^{116,117}): the pH of a system can predict the hydrolysis of AHLs¹¹⁸; common soil minerals adsorb AHLs¹¹⁹; various organisms produce lactonases which can degrade AHLs¹²⁰; and reactive oxygen species can oxidize AHLs.^{121,122} One environmental factor on AHL stability that remains unexamined is the presence of metals. Bacteria often exist in metal-rich environments (e.g., soils, water distribution systems, hospital surfaces).^{123–}

125

Recently, metal-based NPs have been used to reduce QS in bacteria, in an effort known as *quorum quenching*.^{126–131} Silver has garnered the most attention. Naik, et al., found that AgCl coated TiO₂ NPs inhibited QS by interfering with AHL activity and inhibited the production of antioxidant pigments in *C. violaceum*.¹²⁹ Singh, et al., showed that mycogenic Ag NPs reduced violacein synthesis in *C. violaceum* and attenuated biofilm formation and virulence factors in *Pseudomonas aeruginosa* via a down regulation of transcriptional activity of AHL synthase and receptor enzymes.¹²⁸ Mohanty, et al., found reduced levels of AHL in cultures of *Pseudomonas syringae* when exposed to Ag NPs.¹²⁷ The evidence of using metals, especially Ag, to inhibit QS is strong, but none of the studies, that we are aware of, have

considered the interaction between released ions and AHLs. Elucidating a mechanism for metallic NP–QS interactions requires separating the effect of a NP due to its physical properties (e.g., size, crystalline structure, specific surface area, conductivity, etc.) from the effect of the solubilized ions released from the particle. Distinguishing between metal-ion effects and NP effects is of particular concern in QS-inhibition studies because previous research has identified that AHL degradation products or synthetic precursors have metal chelation potential and thus may alter soluble metal concentrations.^{76,132} However, the potential for unhydrolyzed native AHLs to participate in metal complexation reactions has not, to the best of our knowledge, been considered. Understanding these interactions is crucial, as cations occur naturally in the environment, and are purposefully utilized in healthcare and engineering systems for their antibacterial and quorum quenching properties, e.g., copper and silver.^{124,133}

The purpose of this work was to reveal the interaction between a QS signaling molecule, *N*-hexanoyl-L-homoserine lactone (HHL) and two commonly released cations used in antimicrobial applications, silver (Ag^+) and copper (Cu^{2+}). We hypothesized that HHL and cations could form complexes, as similarly structure organic molecules have been demonstrated to previously.⁷⁶ We further hypothesized that complexation between free AHL and free Ag^+ or Cu^{2+} could limit the bioavailability of each constituent, diminishing signal reception and metal toxicity.

Methods

Materials. Chemicals and reagents used include *N*-hexanoyl-L-homoserine lactone (HHL, >95%, Cayman Chemicals, Ann Arbor, MI), Silver nitrate (Acros Organics), Copper(II) nitrate (Acros Organics), ferric chloride (>99%, Sigma-Aldrich), ammonium acetate (Fischer Scientific), acetonitrile (HPLC grade, EMD), water (Millipore, 18 M Ω cm Milli-Q), formic

acid (Alfa Aesar), Luria-Bertani Broth (Miller, LB Difco BD), kanamycin sulfate (Amresco), Dimethyl sulfoxide (>99.9%, Alpha Aesar). *Chromobacterium violaceum* CV026 was acquired through the Colección Española de Cultivos Tipo (CECT 5999). Instruments used include Thermo Scientific Spectronic 2000; Agilent Technologies Cary Series UV-Vis-NIR Spectrophotometer; and Agilent 6430 Triple Quad LC/MS, Agilent 1100 Series.

HHL–metal complexation studies. Stock solutions of silver nitrate (10 mM), copper(II) nitrate (10 mM), ferric chloride (10 mM), and HHL (10 mM) were prepared in ammonium acetate buffer (20 mM, pH 7). None of the stock solutions contained any precipitates. Stock solutions were diluted to 5 mM to create 1:1 molar ratios of HHL:Ag and HHL:Cu separately. In an attempt to detect HHL:Fe complexes, 1:1, 2:1, and 3:1 ratios were tested. The mixtures were immediately vortexed and analyzed on liquid chromatography–mass spectrometry (LC-MS, **Table 3-1**, **Figure 3-1**). Speciation simulations were carried out using Visual MINTEQ (**Table 3.2**).¹³⁴ Stock solutions prior to mixing were also analyzed by LC-MS (**Table 3-3**).

Table 3-1. LC-MS conditions used to detect metal–HHL complexation

Injection volume	5.00 µL, injection with needle wash in DI H ₂ O
Mobile phase A	H ₂ O, 0.1% formic acid
Mobile phase B	Acetonitrile, 0.1% formic acid
Solvent run type	Isocratic, 1:1 mixture of mobile phase A:B
Flow rate	0.500 mL/min
Ion source	ESI
Scan type	MS2 Scan
Start mass	20 u
End Mass	800 u
Scan time	500 ms
Fragmentor voltage	135 V
Cell accelerator voltage	7 V
Polarity	Positive
Scan step size	0.1 u
Gas temperature	300°C
Gas flow	10.0 L/min
Nebulizer	15.0 psi
Chromatogram type	Total ion count

Table 3-2. Visual MINTEQ simulation of chemical speciation of AgNO₃ and Cu(NO₃)₂ solutions in ammonium acetate buffer.

Component	% of total concentration	Species
AgNO₃ stock		
Ag ⁺¹	71.39	Ag ⁺¹
	5.55	Ag-Acetate (aq)
	0.08	Ag-(Acetate) ₂ ⁻
	13.22	AgNH ₃ ⁺
	9.53	Ag(NH ₃) ₂ ⁺
	0.20	AgNO ₃ (aq)
Acetate ⁻¹	98.08	Acetate ⁻¹
	1.38	Ag-Acetate (aq)
	0.04	Ag-(Acetate) ₂ ⁻
	0.48	H-Acetate (aq)
NH ₄ ⁺¹	91.48	NH ₄ ⁺¹
	0.44	NH ₃ (aq)
	3.30	AgNH ₃ ⁺
	4.76	Ag(NH ₃) ₂ ⁺
NO ₃ ⁻¹	99.79	NO ₃ ⁻¹
	0.20	AgNO ₃ (aq)
Cu(NO₃)₂		
NO ₃ ⁻¹	99.91	NO ₃ ⁻¹
	0.08	CuNO ₃ ⁺
Acetate ⁻¹	93.47	Acetate ⁻¹
	1.75	Cu-(Acetate) ₂ (aq)
	0.17	Cu-(Acetate) ₃ ⁻
	0.45	H-Acetate (aq)
	4.14	Cu-Acetate ⁺
NH ₄ ⁺¹	95.80	NH ₄ ⁺¹
	0.10	Cu(NH ₃) ₃ ⁺²
	1.11	Cu(NH ₃) ₂ ⁺²
	0.46	NH ₃ (aq)
	2.51	CuNH ₃ ⁺²
Cu ⁺²	10.16	Cu ⁺²
	3.50	Cu-(Acetate) ₂ (aq)
	0.22	Cu-(Acetate) ₃ ⁻
	2.03	CuOH ⁺
	0.02	Cu ₂ OH ⁺³
	0.03	Cu(OH) ₂ (aq)
	17.81	Cu ₂ (OH) ₂ ⁺²
	37.09	Cu ₃ (OH) ₄ ⁺²
	0.13	Cu(NH ₃) ₃ ⁺²
	2.22	Cu(NH ₃) ₂ ⁺²
	10.05	CuNH ₃ ⁺²
	0.08	CuNO ₃ ⁺
	16.59	Cu-Acetate ⁺

Table 3-3. LC-MS conditions used to detect the loss of HHL as a function of Ag⁺ and Cu²⁺ concentration.

Injection volume	2.00 µL, injection with needle wash in DI H ₂ O
Mobile phase A	H ₂ O, 0.1% formic acid
Mobile phase B	Acetonitrile, 0.1% formic acid
Solvent run type	Isocratic, 1:1 mixture of mobile phase A:B
Flow rate	0.500 mL/min
LC column	Agilent Eclipse XBD-C18, 5 µM, 4.6 x 150 mm
Column temperature	22.0 °C
Ion source	ESI
Scan type	MRM
HHL	
Precursor ion	200.1 u
Product ions (Frag., CE. energies)	102.1 u (85 V, 4 V) 99.1 u (85 V, 8 V) 71.1 u (85 V, 12 V)
HHL hydrolysis product	
Precursor ion	218.2
Product ions (Frag., CE. energies)	139.9 (100 V, 12 V)
Fragmentor voltage	135 V
Cell accelerator voltage	4 V
Polarity	Positive
Gas temperature	300 °C
Gas flow	11.0 L/min
Nebulizer	15.0 psi
Chromatogram type	Total ion count

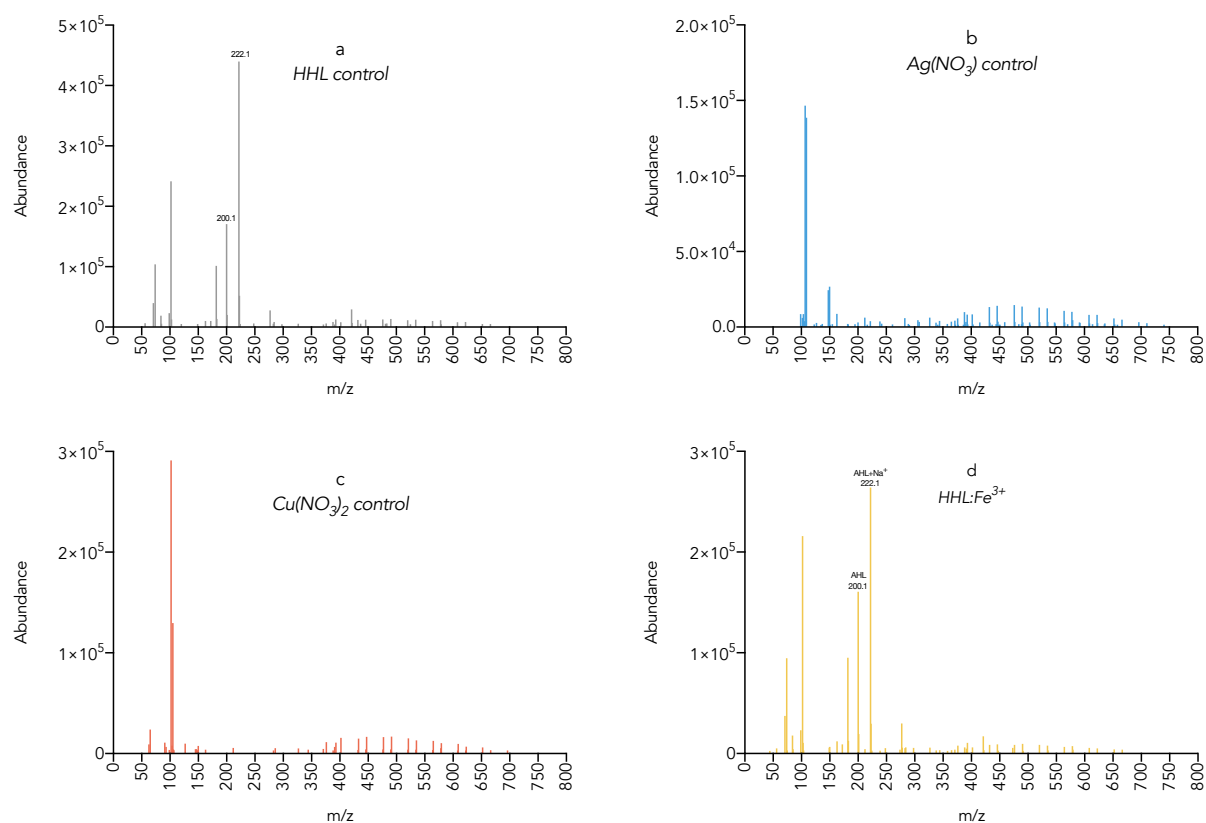


Figure 3-1. Positive ion MS/MS spectra of (a) 10 mM HHL control, (b) 10 mM AgNO₃ control, (c) 10 mM Cu(NO₃)₂ control, and (d) 3:1 molar ratio HHL:Fe.

Mixtures were then analyzed using attenuated total reflection Fourier transform infrared spectroscopy (ATR-FTIR). ATR-FTIR spectra were obtained using a PerkinElmer Frontier FT-IR spectrometer equipped with a germanium ATR crystal. Scans were performed from 4000 cm^{-1} to 700 cm^{-1} at a rate of 0.2 cm/s . The traces are the average of 4 scans with a 4 cm^{-1} resolution. Spectra were generated using PerkinElmer Spectrum software. The source was an MIR and the detector was an MIR TGS ($1500\text{-}370\text{ cm}^{-1}$) with a OptKBr beamsplitter.

To further assess the structure of the formed complexes, gas-phase calculations were performed at the density functional theory (DFT) level using Gaussian 03 through the server WebMO.¹³⁵ Geometry optimization was performed using the hybrid B3LYP gradient corrected correlation function, and two different basis sets were employed. The basis set of 6-31G(d) was used on all the atoms for HHL(Cu^{2+}) and HHL₂(Cu^{2+}). The silver complexes were a bit more complicated—the basis set used for these complexes was 3-21G(d) due to the limitations of the server with calculations of heavier metal ions. However, structures could be calculated for HHL(Ag^+) and HHL₂(Ag^+) complexes.

Stock solutions of silver nitrate, copper(II) nitrate, and HHL (10 mM) were prepared in ammonium acetate buffer (20 mM, pH 7). Stock solutions were diluted to create 1:100, 1:50, 1:5, and 1:1 molar ratios of HHL: Ag^+ and HHL: Cu^{2+} separately. The mixtures were immediately vortexed and analyzed by liquid chromatography-MS to monitor HHL m/z 200 $[\text{MW}+\text{H}]^+$ and the degradation product, hydrolyzed HHL m/z 218 $[\text{MW}+\text{H}_2\text{O}+\text{H}]^+$ (**Figure 3-2, Table 3-4**). The total abundance counts for the hydrolyzed HHL were too low to quantify differences compared to controls. Abundance counts of hydrolyzed HHL were <100 , compared to $>10^5$ counts for unhydrolyzed HHL (**Figure 3-3**). Thus, loss of HHL due to hydrolysis was not considered to be a significant factor.

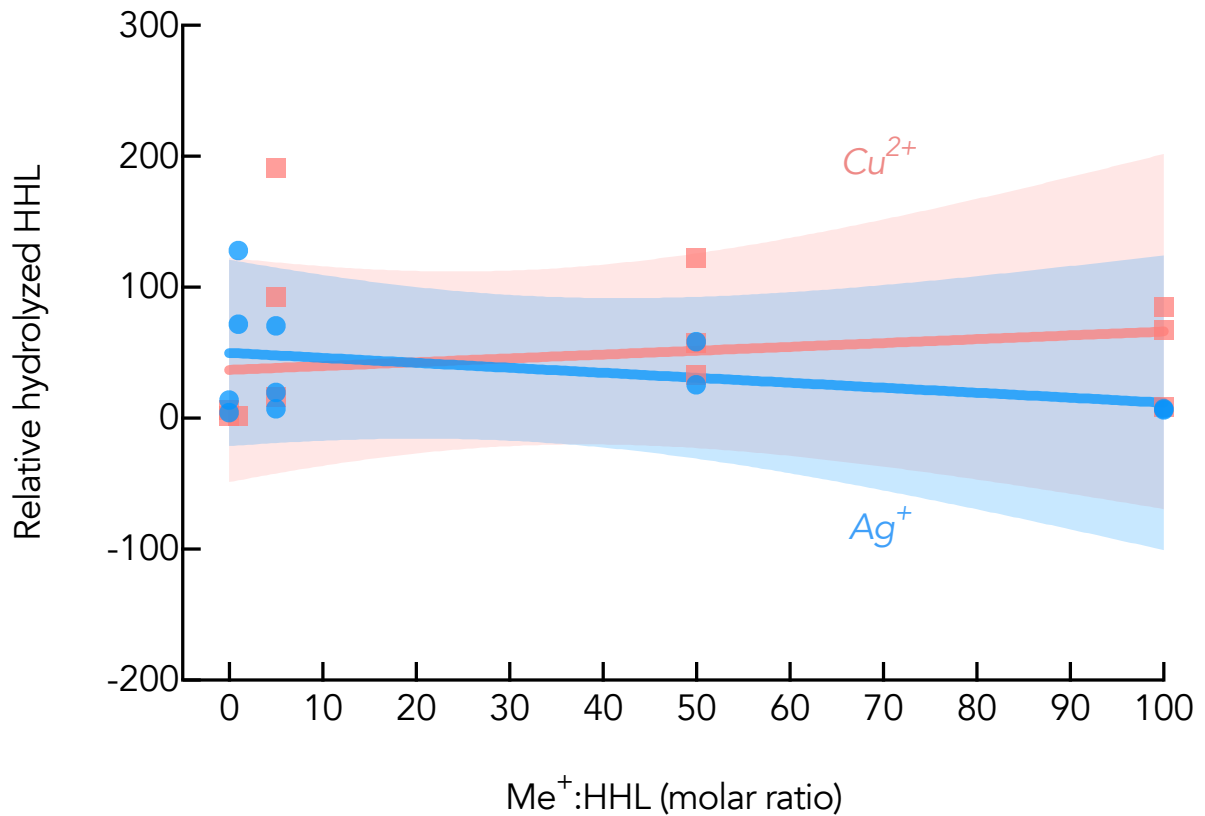


Figure 3-2. Hydrolyzed HHL as a function of increasing added Ag or Cu.

Table 3-4. Statistical analysis of the relationship between HHL hydrolysis and Ag or Cu concentrations shown in **Figure 3-2**.

	Ag	Cu
Best-fit values \pm SE		
Slope	-0.04167 ± 0.04898	0.07367 ± 0.1354
Y-intercept	5.477 ± 2.452	9.313 ± 6.778
X-intercept	131.4	-126.4
1/slope	-24	13.57
95% Confidence Intervals		
Slope	-0.1975 to 0.1142	-0.3573 to 0.5046
Y-intercept	-2.325 to 13.28	-12.26 to 30.88
X-intercept	-infinity to +infinity	-infinity to +infinity
Goodness of Fit		
R square	0.1944	0.0898
Sy.x	4.286	11.85

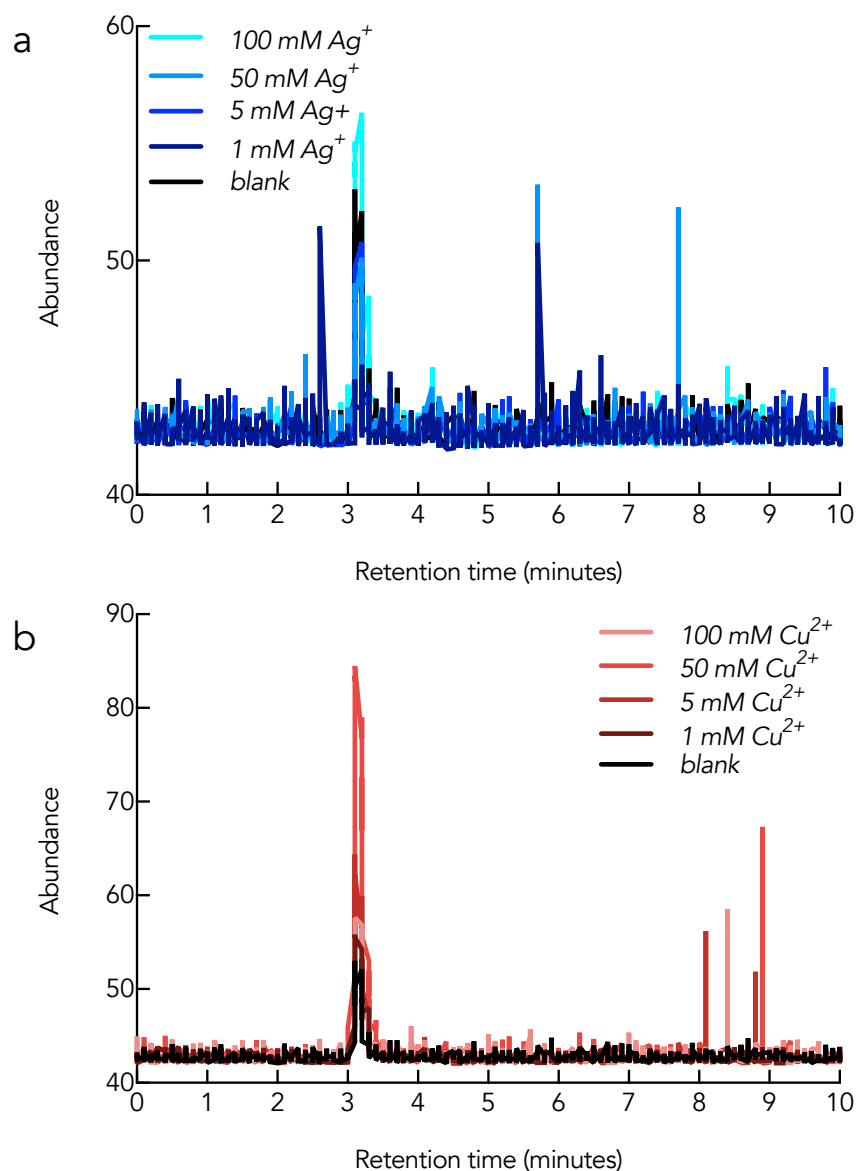


Figure 3-3. LC-MS spectra monitoring HHL hydrolysis product over time in the presence of Ag (a) and Cu (b).

***Chromobacterium violaceum* biological assay.** Freezer stock cultures of *Chromobacterium violaceum* CV026 (CECT 5999) were inoculated in LB broth supplemented with 50 µg/mL kanamycin and were grown overnight aerobically (200 rpm, 30°C, pH 7). Cultures were then diluted to OD₆₀₀=0.001 before experimentation. 96-well plates were used to monitor cell growth and violacein production at various Ag and Cu exposure concentrations, delivered as Ag(NO₃) or Cu(NO₃)₂, respectively. Individual wells contained 190 µL of LB broth (50 µg/mL kanamycin, pH 7). Experimental wells contained a fixed amount of 0.75 µM HHL and

were incubated with various concentrations of either $\text{Ag}(\text{NO}_3)$ or $\text{Cu}(\text{NO}_3)_2$ before being inoculated with 10 μL of CV026 culture. As suggested by the name, No-HHL control wells did not contain any HHL. The 96-well plates were then scanned on a multi-well plate reader to gather an initial OD_{600} measurement. Plates were then wrapped in aluminum foil and placed on an orbital plate shaker at 200 rpm for 24 hours at 30°C. The plates were then scanned again at OD_{600} to determine growth, which was normalized to the initial OD_{600} reading.

Violacein production after 24 hours of growth was determined as described previously.¹³⁶ The 96-well plates were placed in an oven at 60°C without a cover until the well contents were completely evaporated (at least 6 hours). Once dry, 200 μL of DMSO was added to each well. The plates were then covered, wrapped in aluminum foil, and placed on an orbital shaker at 200 rpm overnight at 30°C to dissolve the violacein. Violacein production was then detected by measuring OD_{580} on a multi-well plate reader. To test if the presence of Ag or Cu would shift the absorbance of violacein, cultures of CV026 + HHL (without Ag^+ or Cu^{2+} supplementation) were grown as described above for 24 hours and violacein was extracted using DMSO supplemented with either 0.1 mM of $\text{Ag}(\text{NO}_3)$ or 1.0 mM $\text{Cu}(\text{NO}_3)_2$. No peak shift was detected (**Figure 3-4**).

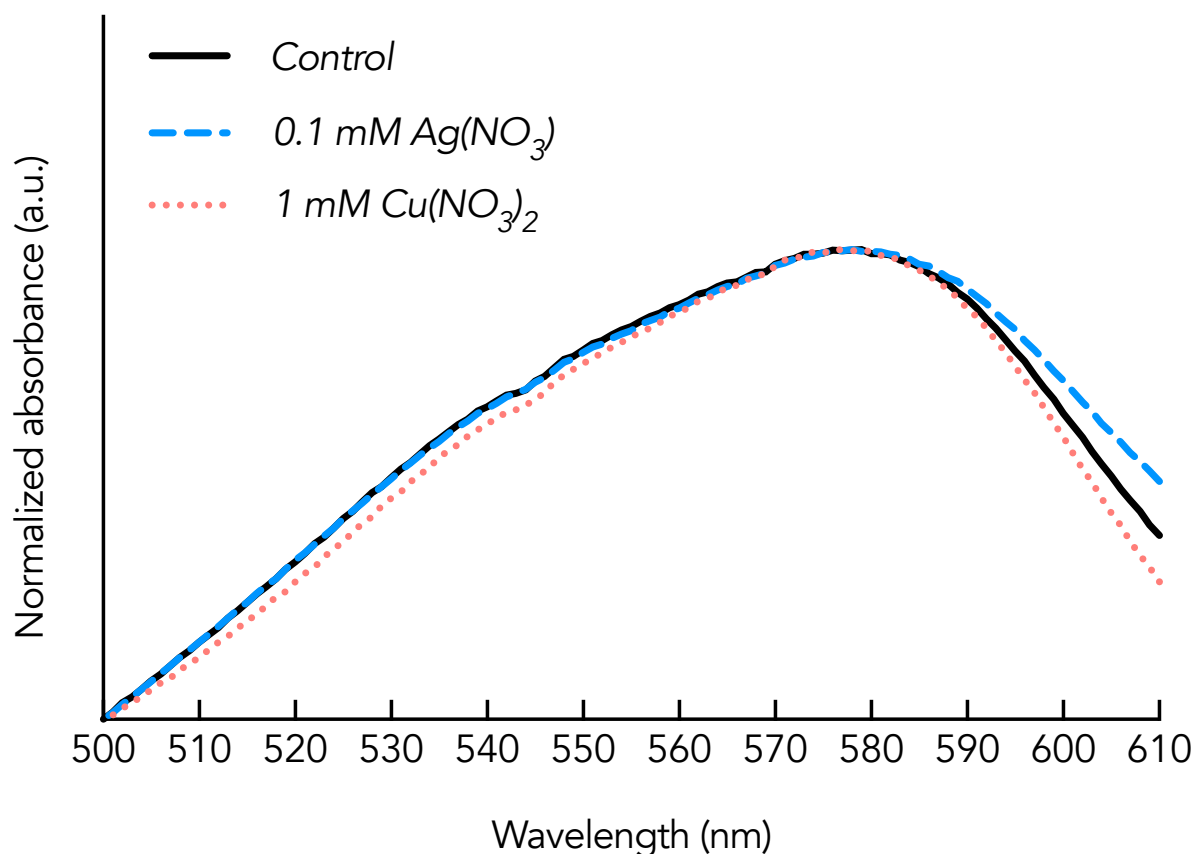


Figure 3-4. Absorbance (OD₅₈₀) of violaceum in the presence of Ag, Cu, or a no-metal control.

Results and Discussion

The interactions between a well-studied QS signaling molecule, *N*-hexanoyl-L-homoserine lactone (HHL), and two commonly used antibacterial metal ions, Ag⁺ and Cu²⁺, was examined first. Mixtures of 1:1 (molar ratio) of HHL:Ag and HHL:Cu were prepared in an aqueous buffer and analyzed on a tandem mass spectrometer to identify the mass-to-charge ratio (*m/z*) of the resulting compounds (**Figure 3-5a** and **b**). Free HHL (*m/z* 200 [MW+H]⁺) was identified in each sample. In the HHL:Ag mixture, a 1:1 and a 1:2 Ag:HHL complex were identified, herein referred to as **1** and **2**, respectively. **1** is identified by the *m/z* peaks at 306 and 308, arising from the natural isotopes of Ag: ¹⁰⁷Ag (51.83% natural abundance) and ¹⁰⁹Ag (48.16% natural abundance), respectively. **2** is identified by the *m/z* peaks at 505 and 507, which correspond to the additive molecular weight of two HHL molecules plus ¹⁰⁷Ag or

^{109}Ag , respectively. Of the total $\text{HHL}_x(\text{Ag}^+)$ complexes formed, 89.80% was **1** and 10.20% was **2**.

The mixtures of 1:1 HHL:Cu exhibited similar complexation behavior as silver, where an apparent 1:1 HHL:copper complex, herein **3**, is identified by the m/z peaks at 262 and 264, corresponding to the natural abundance of ^{63}Cu (69.2% natural abundance) and ^{65}Cu (30.8%

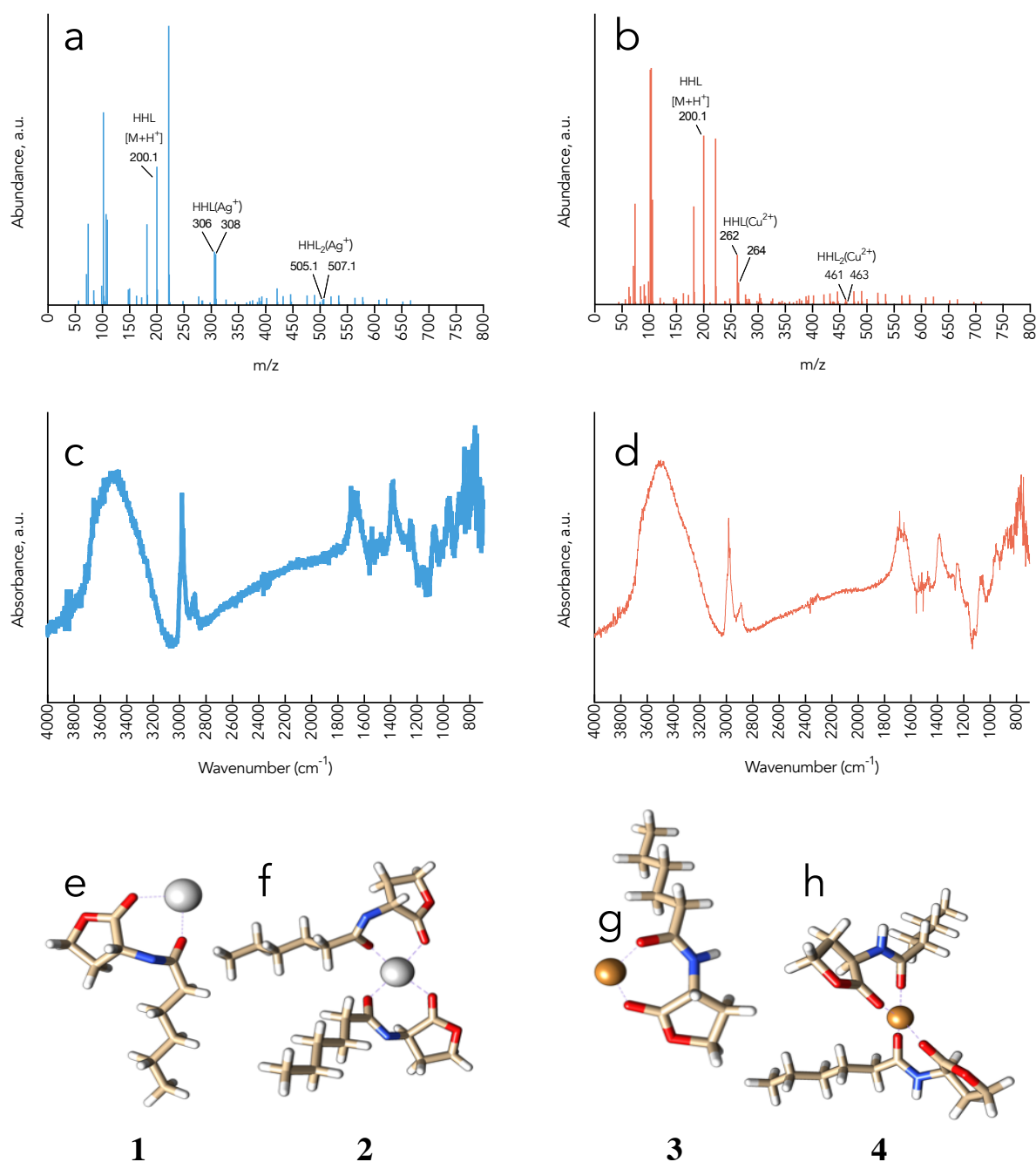


Figure 3-5. Positive ion MS/MS spectra of (a) HHL:Ag and (b) HHL:Cu. ATR-FTIR spectra of (c) HHL:Ag and (d) HHL:Cu mixture minus cation-free HHL spectra on KBr tablet. Optimized structure of (e) **1** HHL(Ag⁺), (f) **2** HHL₂(Ag⁺), (g) **3** HHL(Cu²⁺), and (h) **4** HHL₂(Cu²⁺) using B3LYP 3-21G(d) and 6-31G(d) for silver and copper complexes, respectively.

natural abundance), respectively. Similarly, a 2:1 HHL:Cu complex, herein **4**, is identified by the m/z peaks at 461 and 463. Interestingly, **3** and **4** were expected to carry an overall net charge of +2, which would result in an m/z of 131 and 231. The observed peaks at m/z = 262, 264, 461, and 463 suggest that Cu^{2+} has been reduced to Cu^+ . One explanation is that the ESI-MS ionization process induced a redox reaction of Cu^{2+} , as previous studies reported that Cu^{2+} reduction to Cu^+ can occur in ESI-MS ionization due to charge transfer between copper complexes and solvent molecules in the gas phase of the chamber or in an aqueous sample matrix.^{137–139} Of the total $\text{HHL}_x(\text{Cu}^{2+})$ complexes formed, 89.17% was **3** and 10.83% was **4**. None of the peaks attributed to **1**, **2**, **3**, or **4** were present in the MS/MS scan of HHL control, $\text{Ag}(\text{NO}_3)$ control, or $\text{Cu}(\text{NO}_3)_2$ control. Conversely, all unlabeled peaks in **Figure 3-5a** and **b** were present in the controls.

Kauffmann et al. originally revealed that tetramic acid, an AHL degradation product from *Pseudomonas aeruginosa*, complexed Fe^{3+} .⁷⁶ When we monitored HHL:Fe mixtures at 1:1, 2:1, and 3:1 (molar ratios) via MS/MS, we did not identify any peaks that were characteristic to the Fe isotope pattern in any of the samples. Other studies have found that AHL degradation products complex various metal ions, and Kauffmann et al. suggests that these degradation products may be “primordial siderophores”.^{76,140} However, to the best of our knowledge, this is the first report of metal complexation with an unhydrolyzed, condensed, AHL signaling molecule.

To elucidate the structure of the HHL:metal complexes, ATR-FTIR spectra were gathered in order to identify the shifts in HHL bond vibrations after association with Ag^+ or Cu^{2+} . The spectra of the aqueous HHL solution was used as a control and subtracted from the spectra of the experimental aqueous solutions, 1:1 mixtures of HHL:Ag or HHL:Cu, so that any shifts or changes were attributed to the complexation of HHL to Ag^+ or Cu^{2+} (**Figure 3-5c** and **d**; raw spectra for HHL, HHL: Ag^+ , and HHL: Cu^{2+} are presented in **Figure 3-6**). The

FTIR spectra for the 1:1 HHL:Ag and HHL:Cu mixtures are similar, exhibiting a broad peak at 3500 cm^{-1} , with sharper peaks at $2990\text{--}2890\text{ cm}^{-1}$ and 1690 cm^{-1} , which were assigned to the stretching vibrations of $\nu(\text{O-H})/\nu(\text{N-H})$, $-\nu(\text{C-H})$, and $-\nu(\text{C=O})$, respectively.

Simulated coordination complexation occurred with the carbonyl oxygen moieties of HHL (**Figure 3-5e-h**), which are believed to form hydrogen bonds with the LuxR-type cognate receptor, required for QS activated gene expression.¹⁴¹ The estimated bond lengths and bond angles for all four complexes are presented in **Table 3-5** and XYZ coordinates are presented in **Table 3-6**. While gas phase calculations do not account for aqueous behavior with neighboring solvents, the coordination with the oxygen moieties can be accounted for twofold: (1) the charge of the cations would favor and suggest binding to the carbonyl oxygen over the amine nitrogen; (2) computational modeling was attempted to minimize the geometry with preferential binding to the amine nitrogen, but the metal and a structure would not converge. While it is feasible that the binding in solution would be different than in the gas phase, previous reports^{76,140} suggest binding to these oxygen groups in the AHL degradation product, tetramic acid.

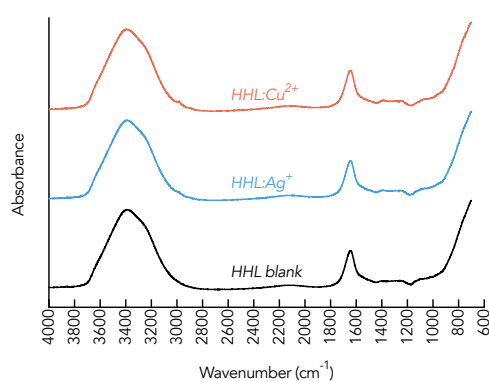


Figure 3-6. Untreated ATR-FTIR scans of HHL, HHL + AgNO_3 , and HHL + $\text{Cu}(\text{NO}_3)_2$ mixtures.

Table 3-5. Lengths (\AA) of cation–oxygen bonds in compounds **1**, **2**, **3**, and **4**.

Structure	Metal–Oxygen1	Metal–Oxygen2	Metal–Oxygen3	Metal–Oxygen4	Average
1:1 Ag:AHL	2.2453	2.245			2.24515
1:2 Ag:AHL	2.0636	2.151	2.0636	2.1483	2.106625
1:1 Cu:AHL	1.7445	1.7218			1.73315
1:2 Cu:AHL	1.8974	1.9223	1.8957	1.9219	1.909325

Table 3-6. XYZ coordinates used to generate compounds **1, 2, 3,** and **4.**

Ag ⁺				Cu ²⁺										
Figure 3-5			Figure 3-5			Figure 3-5			Figure 3-5					
X	Y	Z	X	Y	Z	X	Y	Z	X	Y	Z			
C	0.000	0.000	0.000	0.000	0.000	C	0.000	0.000	0.000	C	0.000	0.000		
C	-0.799	0.909	-0.979	C	-2.162	-2.134	-0.368	C	-0.731	-1.322	-0.376	H	0.282	0.438
H	-1.718	1.289	-0.534	O	-2.539	-3.410	-0.421	H	-0.964	-1.930	0.500	H	0.875	0.052
C	0.220	2.026	-1.270	C	-3.704	-3.578	-1.382	C	-2.017	-0.861	-1.099	C	-1.197	0.739
O	1.544	1.308	-1.259	C	-4.284	-2.158	-1.519	O	-1.624	0.522	-1.660	C	-1.629	0.156
C	1.458	0.141	-0.588	C	-3.095	-1.219	-1.213	C	-0.566	0.981	-1.068	C	-2.827	0.899
Ag	2.552	-2.818	-0.879	N	-3.539	-0.072	-0.427	O	-0.142	2.158	-1.312	H	-3.683	0.858
O	0.351	-2.883	-1.316	C	-2.745	0.963	-0.315	Cu	1.135	2.981	-0.456	C	-3.247	0.289
C	-0.649	-2.357	-0.738	C	-3.183	2.171	0.481	O	2.132	1.950	0.497	H	-2.406	0.322
C	-2.041	-2.921	-0.860	C	-4.641	2.109	0.971	C	2.425	0.680	0.371	C	-4.438	1.005
C	-3.161	-1.858	-0.783	H	-5.305	1.979	0.109	C	3.828	0.238	0.572	N	-4.236	1.861
C	-4.563	-2.500	-0.875	H	-4.770	1.229	1.610	C	4.757	0.785	-0.578	C	-5.194	2.840
H	-4.686	-3.220	-0.056	C	-5.037	3.385	1.745	C	6.218	0.329	-0.355	C	-6.399	2.228
H	-4.644	-3.058	-1.818	H	-4.377	3.505	2.616	H	6.265	-0.767	-0.347	O	-6.680	2.879
C	-5.693	-1.450	-0.807	H	-4.894	4.265	1.103	H	6.567	0.687	0.622	C	-5.781	4.029
H	-5.563	-0.725	-1.622	C	-6.505	3.344	2.225	C	7.152	0.871	-1.463	C	-4.591	3.754
C	-7.090	-2.099	-0.914	C	-6.893	4.618	3.005	H	7.108	1.968	-1.470	H	-4.164	4.673
H	-7.876	-1.339	-0.863	H	-7.936	4.572	3.334	C	8.611	0.414	-1.240	H	-3.807	3.220
H	-7.194	-2.636	-1.863	H	-6.260	4.737	3.891	H	9.257	0.808	-2.031	H	-6.356	4.918
H	-7.249	-2.811	-0.097	H	-6.773	5.508	2.375	H	8.990	0.775	-0.279	H	-5.533	4.057
H	-5.616	-0.898	0.139	H	-7.164	3.229	1.355	H	8.684	-0.679	-1.255	O	-7.095	1.271
H	-3.043	-1.139	-1.605	H	-6.650	2.463	2.864	H	6.802	0.517	-2.441	Cu	-7.313	0.464
H	-3.077	-1.309	0.164	H	-2.500	2.277	1.337	H	4.709	1.880	-0.574	O	-5.580	0.839
H	-2.082	-3.482	-1.799	H	-3.027	3.054	-0.152	H	4.400	0.414	-1.546	O	-8.510	-0.833
H	-2.172	-3.642	-0.038	O	-1.535	1.036	-0.922	H	4.183	0.667	1.518	C	-9.130	-1.766
N	-0.477	-1.347	0.171	H	-2.522	-0.921	-2.104	H	3.897	-0.851	0.628	C	-9.453	-1.957
O	2.417	-0.617	-0.457	H	-4.707	-1.984	-2.510	N	1.475	-0.195	0.018	C	-10.489	-3.096
H	0.123	2.482	-2.253	H	-5.042	-1.969	-0.756	H	1.778	-1.163	-0.114	H	-10.410	-3.773
H	0.256	2.783	-0.485	H	-3.277	-3.969	-2.306	H	-2.304	-1.455	-1.963	C	-10.189	-3.800
H	-1.028	0.353	-1.892	H	-4.370	-4.302	-0.918	H	-2.863	-0.664	-0.440	O	-9.556	-2.767
H	0.042	0.473	0.990	O	-1.163	-1.785	0.295	H	-0.111	-1.897	-1.071	H	-11.070	-4.141
				O	1.365	1.503	-0.369	H	-0.327	0.368	0.984	H	-9.467	-4.614
				C	1.360	2.401	0.654					H	-11.502	-2.679
				C	0.535	3.642	0.461					N	-9.961	-0.761
				C	1.137	4.528	-0.669					C	-9.268	0.357
				C	0.267	5.772	-0.942					C	-9.900	1.394
				H	0.182	6.369	-0.023					C	-10.140	2.736
				H	-0.747	5.452	-1.220					C	-10.749	3.792
				C	0.848	6.656	-2.069					H	-11.694	3.412
				H	0.935	6.058	-2.985					H	-10.078	3.946
				C	-0.028	7.897	-2.340					C	-11.004	5.133
				H	0.400	8.509	-3.141					H	-10.059	5.510
				H	-1.039	7.600	-2.640					C	-11.609	6.184
				H	-0.107	8.519	-1.440					H	-11.780	7.127
				H	1.861	6.974	-1.790					H	-10.946	6.390
				H	1.216	3.922	-1.579					H	-12.573	5.849
				H	2.147	4.842	-0.379					H	-11.675	4.973
				H	-0.471	3.335	0.154					H	-9.184	3.098
				H	0.491	4.195	1.401					H	-10.808	2.572
				N	2.060	2.222	1.743					H	-9.207	1.555
				C	2.954	1.092	1.905					H	-10.837	1.017
				C	4.420	1.441	1.488					O	-8.110	0.551
				H	4.885	2.127	2.195					H	-10.879	-0.841
				C	5.083	0.059	1.468					H	-8.521	-2.274
				O	3.972	-0.863	1.011					H	-5.594	3.421
				C	2.774	-0.279	1.180					H	-3.290	1.934
				O	1.746	-0.911	0.857					H	-3.525	-0.761
				H	5.883	-0.056	0.739					H	-2.576	1.959
				H	5.394	-0.284	2.456					H	-0.783	0.192
				H	4.403	1.882	0.488					H	-1.884	-0.906
				H	2.963	0.842	2.976					H	-2.046	0.701
												H	-0.949	1.802
												H	-0.229	-1.059
														-0.170

HHL is the endogenous signaling molecule produced by *C. violaceum* ATCC 31532. In response to HHL signals, *C. violaceum* 31532 produces a fluorescent pigment called violacein. *C. violaceum* CV026 is a QS-negative mutant strain of 31532 that is unable to produce its own HHL, however, CV026 can synthesize violacein in response to the exogenous addition of HHL.³⁸ We tested HHL–metal mixtures for their ability to induce QS in CV026. HHL (0.75 μ M, **Figure 3-7**) was incubated with sublethal concentrations of Ag or Cu before cultures of *C. violaceum* CV026 were inoculated into each well. After 24 hours of incubation at 30°C, violacein production was detected spectroscopically and normalized to cell concentration (**Figure 3-8a**). Over the initial metal exposure concentrations (6.0 x 10⁻⁸–1.0 x 10⁻³ mM Ag added and 8.5 x 10⁻⁵–1.0 mM Cu added), we did not observe a decrease in cell growth suggestive of toxicity, but there was a significant decrease in violacein production in a dose-dependent manner. When the dose response experiments were repeated in the absence of HHL, *C. violaceum* CV026 was more sensitive to Ag addition (**Figure 3-8b** and **Table 3-7**). However, the absence of HHL did not significantly alter the toxicity of Cu. Previously, Braud, et al., found that the extracellular binding of metals by siderophores reduced metal toxicity in *Pseudomonas aeruginosa*.¹⁴²

The formation of **1**, **2**, **3**, and **4**, which would result in a loss of both free HHL and free cation from solution, might explain the observed decrease in violacein production and the observed increase in IC₅₀ value for Ag addition when HHL is present. Previous cell-free studies revealed that copper had no impact on the metallo-enzymes that synthesize violacein (silver was not tested).¹⁴³ Other factors that are known to influence violacein production (i.e., temperature, agitation, pH, nutrients, and absorbance peak-shift due to metals^{143–145}) were controlled in the experimental system here. Recently, Glišić et al., studied the impacts of Cu²⁺ on QS systems and saw a reduction in violacein production in *Chromobacterium violaceum* CV026 and biofilm formation in *Pseudomonas aeruginosa* PAO1.¹⁴⁶ Their proposed mode of

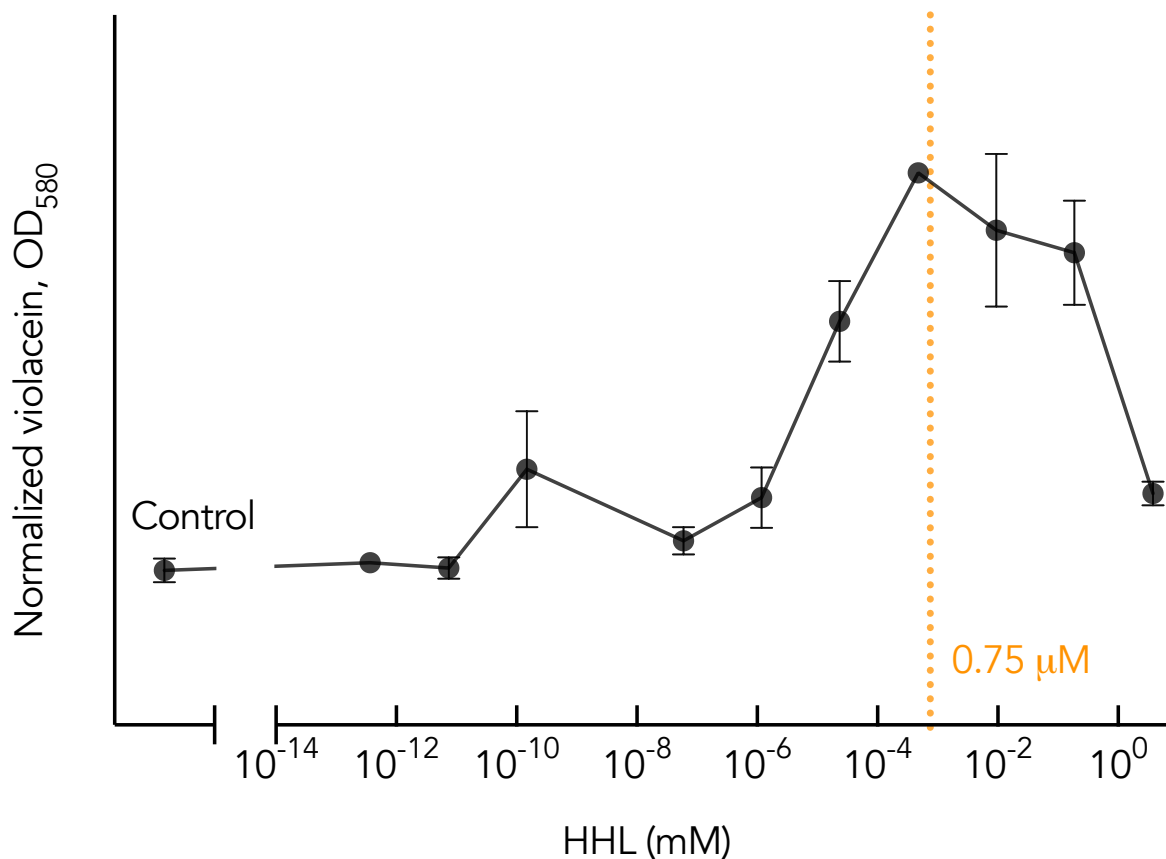


Figure 3-7. Violacein production by *C. violaceum* CV026 after 24 hours of growth (LB, 200 rpm, 30°C) as a function of HHL concentration. Orange dotted line indicates HHL concentration chosen to perform dose-response experiments presented in **Figure 3-8a-b**.

inhibition was modulation of AHL production, while AHL metal interactions were not discussed.

The removal of free HHL after incubation with increasing concentrations of Ag⁺ or Cu²⁺ was quantified by measuring HHL loss via liquid chromatography-MS/MS (**Figure 3-8c**). Using an initial HHL concentration of 1 mM, we observed a nearly 40% decrease in free HHL ligand after a 30-minute incubation with 100 mM Ag⁺ or Cu²⁺ compared to a no-metal control. The detected loss of free HHL from solution is assumed to occur due to metal complexation, as there was no correlation to an increase in the hydrolysis product (**Figure 3-2**). The measurement of an apparent dissociation constants, K_d , in ultra-pure 18 MΩcm water were estimated using:

Equation 3-1

$$f_{1:1} \frac{[HHL(Me^{n+})]}{[Me^{n+}][HHL]} + f_{2:1} \frac{[HHL_2(Me^{n+})]}{[Me^{n+}][HHL]} = \frac{1}{K_d} = K_{stability}$$

by using the known molar metal concentration, $[Me^{n+}]$, the fraction of 1:1, $f_{1:1}$, and 2:1, $f_{2:1}$, HHL: Me^{n+} complexes, the measured molar HHL concentration, $[HHL]$, and assuming all HHL loss was due to metal complexation in 1:1, $[HHL(Me^{n+})]$, and 2:1, $[HHL_2(Me^{n+})]$. Using these values, HHL was deduced to have a stronger affinity for Cu^{2+} ($K_d = 1.78 \times 10^{-5}$ M, or $\log K_{stability} = 10.93$) than Ag^+ ($K_d = 3.71 \times 10^{-4}$ M, or $\log K_{stability} = 7.90$).

Conclusions

The current work demonstrates that HHL, a QS autoinducer of the AHL-class, forms complexes with Ag^+ and Cu^{2+} cations, respectively. The coordination complex appears to occur at the carbonyl oxygen groups of the HHL molecule. Ag^+ toxicity was reduced in *C. violaceum* CV026 when HHL was added to the system, possibly due to HHL- Ag^+ complexation reducing free Ag^+ concentration. This suggests that QS signaling molecules may increase bacterial metal tolerance. Furthermore, when Ag^+ or Cu^{2+} was pre-incubated with HHL, QS-induced violacein production was limited. The mechanism of QS-induced violacein production involves many steps (from the synthesis of signaling molecules, to the synthesis of antioxidant pigment) where the addition of reactive metal ions may interfere. Thus, the nature of the interference was not conclusively determined in the present work. Furthermore, it is important to note here that the biological assays that tested metal toxicity and QS activity were tested in LB media, an undefined nutrient-rich media used to induce QS in CV026. Due to the complexity of LB media, the determination of metal speciation is difficult, and the Ag^+ or Cu^{2+} cations are competing for other organic ligands in addition to HHL. Previous modeling studies looking at copper speciation in complex growth media (pH 7–7.2) found that <5% would be free Cu^{2+} (silver was not studied).¹⁴⁷

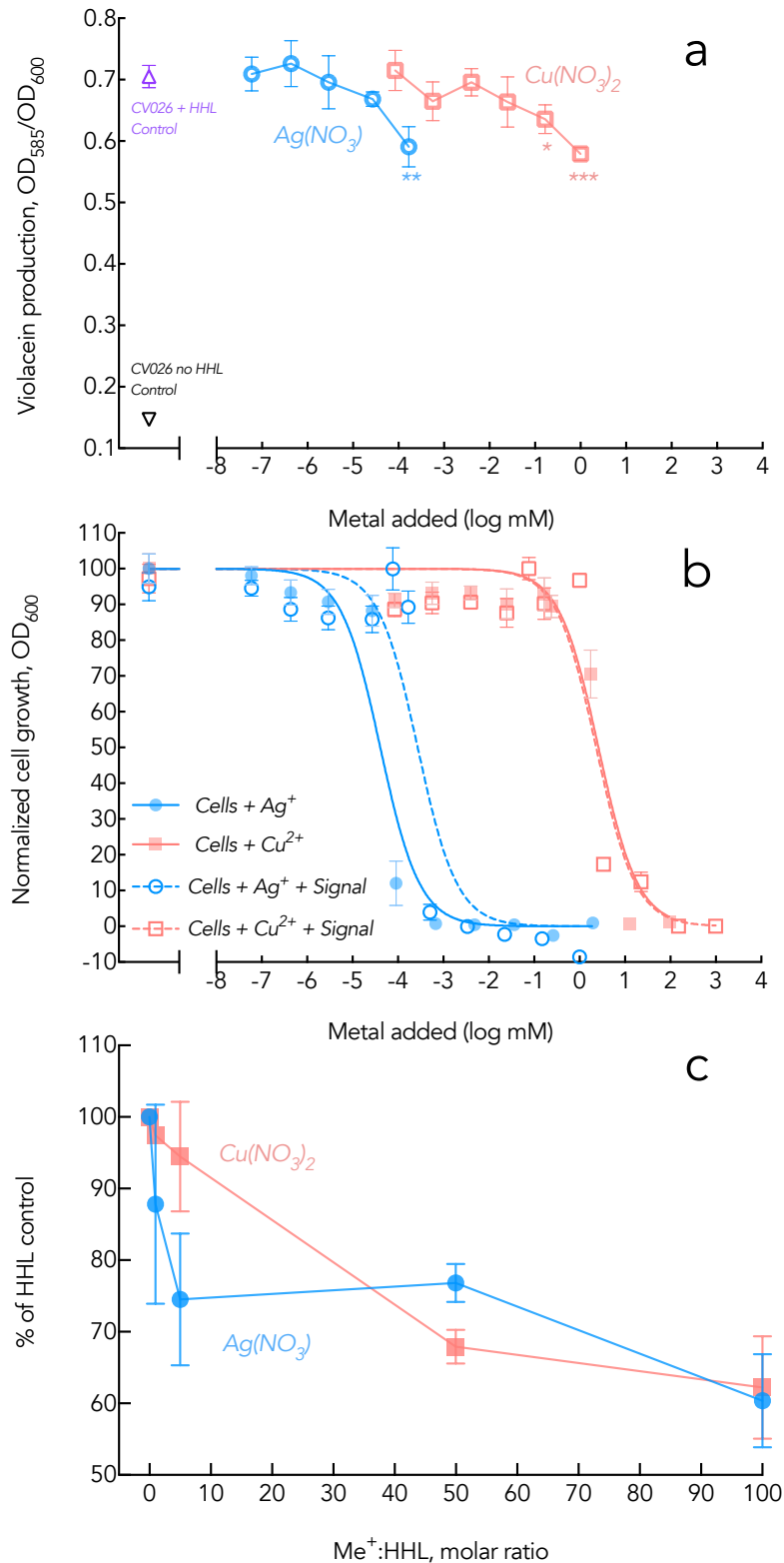


Figure 3-8. (a) Violacein production (OD_{580}) normalized to cell growth (OD_{600}) of *C. violaceum* CV026 exposed to $AgNO_3$ or $Cu(NO_3)_2$. (b) Dose-response curves fit using the Gompertz equation.¹⁴⁸ The X-axis of (a) and (b) represent the log molar concentration of added $AgNO_3$ or $Cu(NO_3)_2$. (c) Loss of free HHL as a function of relative molar concentrations of Ag or Cu. On all graphs, symbols represent the average, error bars represent the standard error of the mean (SEM), and significance asterisks are the results of unpaired t-tests versus the CV026 + HHL Control: * $P < 0.05$, ** $P < 0.01$, *** $P < 0.001$.

Table 3-7. Best fit values (IC_{50} , mM) and profile likelihood from modeling the Gompertz equation (shown in **Figure 3-8b**).

	CV026 + Ag	CV026+Ag+HHL	CV026+Cu	CV026+Cu+HHL
IC_{50}	4.09×10^{-5}	2.73×10^{-4}	2.61	2.32
95% CI	3.04×10^{-5} - 5.45×10^{-5}	2.001×10^{-4} - 3.73×10^{-4}	1.94-3.50	1.73-3.13

The research presented in this chapter was intended to understand the interaction between AHLs and metal ions that are commonly used in medical and engineering applications. However, AHL–metal complexes are likely to be relevant in many natural or contaminated systems where cations are abundant. Furthermore, studies that examine QS where metal ions are present should consider the potential for artifact introduced by the complexation of signaling molecules, as well as enhanced dissolution of metal surfaces due to AHLs chelation potential (See Appendix B: CuO nanoparticle dissolution by a siderophore-emitting bacteria and a cyanogenic bacteria , **Figure B-4**). The potential of extracellular AHL to increase bacterial metal tolerance and metal dissolution should be explored in the future.

4. The of susceptibility of gold nanoparticles to bio-dissolution by a cyanogenic bacterium[§]

Abstract

Gold (Au) NPs are often used to study the physiochemical behavior and distribution of nanomaterials in environmental and biological systems because they are assumed to be inert under ambient conditions. However, Au can be oxidized and dissolved by a common environmental chemical: cyanide. In this work, we used the cyanogenic bacterium *Chromobacterium violaceum*, to demonstrate that cyanide production can lead to a high range oxidative dissolution of Au NPs in soil (15% after 7 days at pH 7). It is known that quorum sensing regulates cyanogenesis in *C. violaceum*, which activation is cell-densities dependent. We assessed the impact of QS on Au NPs biodissolution using different cell density inoculation and the QS-mutant CV026 to demonstrate that Au NP oxidation was driven by QS. Furthermore, an increase of 0.5 unit of pH in soil significantly enhanced Au biodissolution due to changes in cyanide speciation (pKa of 9.21). As a comparison, no Au dissolution was observed in the control abiotic soil. Liquid media experiments confirmed that biogenic cyanide oxidized Au NPs to the soluble form $\text{Au}(\text{CN})_2^-$. These results highlight the conditions for which Au NP biodissolution can occur and how important biotransformations are in (nano)metallic phase-transformations and fate. It will require environmental nanotechnology researchers to reconsider the assumption that Au NPs are inert in all the compartments of the environment.

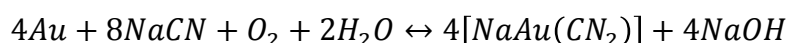
[§]This chapter is currently in preparation with the following co-authors: McGivney, E., Gao, X., Liu, Y., Lowry, G., Casman, E., Gregory, K., VanBriesen, J, Avellan, A.

Introduction

The dissolution of metal NPs modulates their fate, transport, and mode of action in the environment.^{2,20,149,150} Dissolution has been identified as one of the most important predictors of toxicity in Nano-Environmental Health and Safety¹⁵¹, and of behavior in environmental models.¹⁵² Gold nanoparticles (Au NP) are a unique class of nanomaterial because they are relatively stable against dissolution under most conditions. Au NPs are often used to study the physiochemical behavior and distribution of nanomaterials in environmental and biological systems because they are assumed to be inert under ambient conditions.^{153–160} Au NPs are modeled in EHS studies under assumptions of no dissolution or transformation.^{158,161}

The core element of Au NPs, metallic Au, can be oxidized^{162,163} and solubilized by a common environmental constituent¹⁶⁴, cyanide, following the reaction:

Equation 4-1



The mechanisms and kinetics of cyanide-oxidative dissolution of Au have been studied in laboratory settings, including with Au surfaces^{162,163}, colloidal Au¹⁶⁵, and Au nanorods.¹⁶⁶ Due to high specific surface area, nano- and colloidal-Au dissolution half-life kinetics in cyanide media are on the order of seconds.^{165,166}

Cyanide is ubiquitous in the environment due to its formation in natural processes.¹⁶⁴ Certain bacteria, fungi, algae, and plants produce cyanide compounds to deter pathogenic attacks and to regulate biochemical processes.^{164,167,168} In bacteria, cyanide is a secondary metabolite, commonly produced in soils by members of the *Pseudomonas*, *Chromobacterium*, *Rhizobium*, and *Serratia* genera.¹⁶⁹ Bacterially-produced cyanide plays an important ecological role in soils; altering plant growth¹⁶⁹, invertebrate toxicity¹⁷⁰, and fungal pathogenicity.¹⁷¹ Cyanogenic bacteria also have commercial appeal for Au recovery from sulfidic ores¹⁷² and e-waste^{162,173}, and have even been proposed as soil supplements to enhance crop yields.¹⁷⁴ Cyanide production in bacteria occurs at the end of exponential phase,

when populations are dense. In certain bacteria, such as *Pseudomonas aeruginosa*⁴¹ and *Chromobacterium violaceum*¹⁶⁹, cyanogenesis is regulated by quorum sensing (QS). Cyanide is generally produced in the μM range by planktonic bacteria¹⁶⁹, but in QS-regulated biofilms of the *Burkholderia cepia* complex, cyanide concentrations can reach the mM range.¹⁷⁵ Thus, the size and structure of the microbial population affects cyanide production, which may affect the potential for Au dissolution. Biofilms were identified as the most important sink for Au NP in an environmental tracer study¹⁵³, however, the mechanism of Au accumulation in the biofilm was not described. The speciation of Au in the biofilm was not characterized, nor was the biofilm community. In studies that made no distinction between dissolved and particulate Au^{153–160}, conclusions may overstate the persistence of the nanoparticulate form if cyanide-enabled dissolution occurred.

The physical-chemical characteristics of the system could also be a driver for Au NPs biodissolution. The pH of a system is also critical when considering cyanide and metals in the environment. Bacteria produce cyanide as HCN (pKa 9.21), and thus, pH controls the form of cyanide, which affects Au dissolution. Cyanide will only oxidize Au when it is deprotonated, in its free ion state, CN^- .

Despite the knowledge of cyanide oxidative dissolution of Au, and prevalence of cyanogenic bacteria in nature, there are no studies identifying the influence of cyanogenic bacteria on Au NP dissolution in the environment. In aqueous systems, the dissolution of NPs can be easily tracked by separating the dissolved ions from the particles using centrifugation, filtration or dialysis membranes.^{176–178} In soil systems, extraction methods, including pore water extraction or labile metal extraction, are often used to extract dissolved ions from the soil matrix.^{179,180} Oxidative dissolution of Au NPs has largely been ignored in environmental nanotechnology research, with a few exceptions that monitored dissolved Au^{181–183} or speculated about the possibility of dissolution.¹⁸⁴ None of this prior work included soils

containing cyanide or cyanogenic-bacteria. Ignoring the bacteria-assisted dissolution can lead to misunderstandings on NP uptake mechanisms and lead to inaccurate NP persistence estimates.

In the present work, we test the ability of a cyanogenic soil bacterium, *Chromobacterium violaceum*, to oxidize and solubilize Au NPs in soils. Cyanide production is regulated by QS in *C. violaceum*, which is commonly used as a model organism in QS^{38,53,169} and Au-recovery research.^{173,185} Since cyanide production in *C. violaceum* is regulated by QS, we hypothesized that a QS-negative mutant (CV026) would not dissolve Au NPs. In addition, we hypothesized that Au NP dissolution would be sensitive to small pH changes in the soil, due to the pH-dependent dissociation of HCN. Finally, we investigated the mechanism of Au NPs oxidation in pure growth cultures and abiotic cyanide solutions.

Methods

Materials. DTPA (99%, titration), ammonium acetate, and sodium cyanide were purchased from Sigma-Aldrich. Calcium chloride ($\geq 99.0\%$, ACS grade) was purchased from Fisher Scientific. 12 nm citrate-stabilized Au nanoparticles (Au NPs) were provided by the Center for the Environmental Implications of NanoTechnology (CEINT, Durham, NC, USA); they were synthesized as previously described.¹⁸⁶ Standard soil (2.1, sandy soil) was purchased from Lufa Speyer (Germany). *Chromobacterium violaceum* ATCC 31532 was purchased from ATCC. *Chromobacterium violaceum* CV026, a mini-Tn5 mutant³⁸, was acquired through the Colección Española de Cultivos Tipo (CECT 5999).

Nanoparticle characterization. The Au NPs used in this study were synthesized and characterized by the Center of Environmental Implications of NanoTechnology (CEINT, Duke University): a primary particle size of 11.8 ± 1.2 nm (SD, TEM based), a hydrodynamic

diameter of 11.9 ± 0.2 nm (SD), and a zeta potential of -14.1 ± 1 mV (SD) at pH 7 in 10^{-3} M of KCl.

Soil dissolution. Au NP dissolution in soil was measured in the presence and absence of *C. violaceum*, and at two different soil pH values (7 and 7.5). These pH values were chosen to simulate conditions with different relative concentrations of HCN and CN^- . HCN has a pKa value of 9.21. According to simulations in water (Visual MINTEQ¹³⁴), at pH 7, 0.61% of cyanide would exist as free CN^- . At pH 7.5 free CN^- concentrations triples to 1.91%. Air-dried soil was supplemented with a liquid medium (LB, 8 g/L glycine) containing Au NP (final concentration of 1.9 ppm in soil). Glycine was added because it is a metabolic precursor in biogenic cyanide production.¹⁸⁷ The Au NP amended soil was then mixed by hand. Then, *C. violaceum* was grown and washed (centrifuged, following pellet resuspension in equivalent volume of growth media). The initial cell concentration was 1.5×10^9 CFU/g soil, determined by plating. As an abiotic control, soil was supplemented with the growth medium. The total soil moisture content in all experiments was 19%. All samples were prepared, in triplicate, in sterile 50 mL tubes sealed with alcohol-sterilized parafilm, to allow for gas exchange while keeping the moisture content constant, and stored in a 30°C incubator.

Another experiment was run to link cyanide production with Au dissolution. We inoculated the soil with CV026. HCN production in *C. violaceum* is regulated by the *hcnABC* operon, and this operon is upregulated via QS receptor/promoter *cviR*, i.e., when a quorum is reached, *hcnABC* activity increases. The mutant strain CV026 has the *hcnABC* operon, but it lacks the functioning genes to produce QS signal *N*-hexanoyl homoserine lactone (*cviI*), meaning *hcnABC* is never over expressed, even when cell density increases.^{38,169,188}

Finally, we considered the role of bacterial growth on Au dissolution by evaluating induced Au dissolution in soil inoculated with low cell densities of *C. violaceum* culture.

Instead of inoculating the soil directly with a high cell density liquid culture of *C. violaceum* at early stationary phase growth (described above), we supplemented Au NP-containing soil with low-cell density, low-cyanide containing soil. Specifically, 1 gram of soil was taken from the '*C. violaceum*, pH 7' sample after 7 days (see **Table 4-2**) and mixed with 40 g of sterile, Au NP-containing soil. The mixed soil was then incubated at 30°C to promote growth, and Au dissolution was measured over 7 days.

Table 4-1. Simulated species distribution of 100 μM NaCN in water at pH 7 and 7.5.

Species	Percentage of total concentration	
	pH 7	pH 7.5
Na ⁺	100	100
CN ⁻	0.61	1.92
HCN (aq)	99.39	98.08

Soil preparation. Soil (Lufa 2.1) was air dried for 24 hours before adjusting the pH to 7 (adding 0.02 g CaO + 0.02 g CaCO₃ per 10 g of soil) or 7.5 (adding 0.025 g CaO + 0.03 g CaCO₃ per 10 g of soil). These pH values were chosen to produce conditions with different concentrations of CN⁻. The soil was then autoclaved three times and tested for sterility via plating (LB 1.5%, 30°C). The total organic carbon content was 0.56% \pm 0.02% (SD) and 0.53% \pm 0.02% (SD) before and after autoclaving, respectively (InnovOx Laboratory TOC Analyzer, GE Analytical Instruments).

Soil extraction. A DTPA extraction was used to measure the dissolved fraction of Au in soil.¹⁸⁰ DTPA extraction is often used to determine the phytoavailability of metals in soil.^{151,189,190} The extraction efficiency was 116.9% \pm 3.9% (SD), as determined by adding 2000 ppm of Au (delivered as HAuCl₄) and 50 mg of NaCN to 50 g of soil before extraction after 4 days.

For each extraction point, two grams of soil were air-dried and added to 4 ml of a mixture containing 0.01 M CaCl₂, 0.005 M diethylenetriaminepentaacetic acid (DTPA) and 0.1 M triethanolamine (TEA), pH 7.6. The samples were placed on a reciprocal shaker at 180

rpm for 2 hours. Next, the samples were centrifuged at 3000 rpm for 10 minutes. The supernatant of each sample was filtered through a 10 kDa centrifugal filter before being diluted with nitric acid (final nitric acid concentration= 2%) and analyzed via ICP-MS. Porewater pH was determined by placing 2 g of air-dried soil in 20 mL of 0.01 M CaCl₂, shaken (2 hours at 180 rpm), centrifuged (3000 rpm for 10 minutes), and measuring the pH of the supernatant (**Figure 4-1a**). Colony-forming units were determined by mixing .1 g of soil in 1 mL of sterile soil before plating on LB plates, 1.5% agar (**Figure 4-1b**).

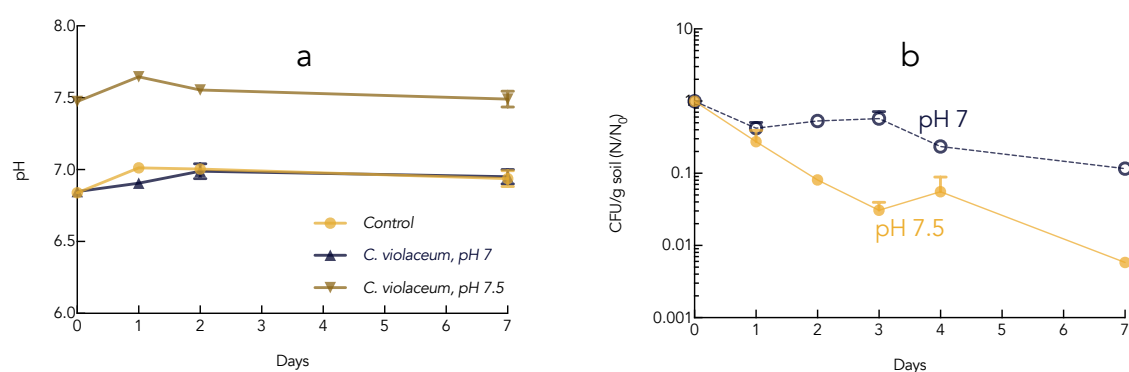


Figure 4-1. (a) pH of and (b) CFU in soil used in the Au NP dissolution experiments over time. Symbols represent the average ($n=3$), error bars represent the standard error of the mean.

Dissolution kinetics. Au NP dissolution kinetics in soil were modeled using an empirical first-order dissolution kinetics model:

Equation 4-2

$$Y = (Y_0 - Y_{max})e^{-kt} + Y_{max}$$

where Y_0 is the dissolution (%) at time zero, Y_{max} is the maximum dissolution (%), or plateau, and k is the observed first-order rate constant (day^{-1}). For this we used Prism (Version 7.0c for Mac, GraphPad Software, www.graphpad.com).

Biotic dissolution. Next, the effect of a live culture and its supernatant (metabolites without cells) on Au NP dissolution was studied. *C. violaceum* was grown to 10^{10} CFU/mL (30°C, 200 rpm, LB media + 0.75 g/L of glycine, pH 7).¹⁸⁷ We centrifuged 80 mL of the culture (5000g for 10 minutes at 4°C). The supernatant was filtered (0.22 μm , PTFE) into sterile 50

mL tubes and used as the *Supernatant* exposure media. The pellets were then resuspended in equivalent volume of fresh growth medium to be used as the *Washed culture* treatment. Separately, sterile growth medium was used as the *Control* treatment. We added 1.9 ppm Au NPs to each treatment. Initial CN⁻ concentrations in the *Supernatant*, *Washed culture*, and *Control* samples were 41.87 ppm (standard deviation: 0.90), 4.05 ppm (standard deviation: 0.60), and 0 ppm, respectively. All samples were prepared in 10 mL volumes in sterile 15 mL centrifugal tubes and placed on an end-over-end rotator for 7 days. At the sampling time points of 0, 1, 2, and 7 days, 1.5 mL was removed and immediately filtered for dissolved fraction metal analysis. Samples were filtered through 10 kDa membranes (5,000g, 10 minutes). All samples were run in triplicate.

Abiotic dissolution. Finally, we studied Au NP dissolution in a simple aqueous buffer. Au NPs (1.9 ppm) were placed in autoclaved 20 mM ammonium acetate buffer (pH 7) in the presence of either 9.8 ppm NaCN (*NaCN*), or in the absence of a NaCN (*Control*). All samples were prepared in 10 mL volumes within sterile 15 mL centrifugal tubes and placed on an end-over-end rotator for 7 days. At the sampling time points of 0, 1, 2, and 7 days, 1.5 mL was removed and immediately filtered for dissolved fraction metal analysis through a 10 kDa membrane (5,000g, 10 minutes). All samples were run in triplicate.

Au detection. Samples were diluted and acidified with nitric acid (final concentration: 2% nitric acid) before being measured via inductively coupled plasma mass spectrometry (ICP-MS, Agilent 7700 Series) under Hydrogen and High Energy Helium (HEHe) acquisition mode.

Cyanide detection. Free cyanide concentration was determined by potentiometry with a cyanide-ion-selective electrode according to the manufacturer's protocol (Orion cyanide electrode, Thermo Scientific). All standards and samples were stabilized with alkaline ionic strength adjustor solution (Orion, Thermo Scientific).

Gold-cyanide. Detection of $\text{Au}(\text{CN})_2^-$ was determined via ESI-MS/MS, using a slightly modified version of a method described previously.¹⁹¹ Samples were filtered (0.22 μm) and analyzed on an LC-MS/MS (Agilent 6430 Triple Quad LC/MS/MS, Agilent 1100 Series). 10 μL of sample was delivered to the MS using a 1:1 isocratic mixture of H_2O (18 M Ωcm , Millipore):Methanol at a flow rate of 0.2 mL/min. The MS was run in negative polarity mode scanning (MS2 Scan) with a fragmentor energy of 80 V and cell accelerator voltage of 7 V. Nitrogen was used as the sheath gas. Identification of $\text{Au}(\text{CN})_2^-$ was determined by monitoring the product ion at m/z 26, derived from the parent ion at m/z 249 using Agilent MassHunter Qualitative Analysis Worskstation Software (Agilent Technologies).

Table 4-2. Au NP dissolution experimental matrix

Soil	Sample identification	Au NP, ppm	Initial CN^- , ppm	pH	Inoculum CFU/g soil
	<i>C. violaceum</i> , pH 7	1.9	41.8	7	1.5×10^9
	<i>C. violaceum</i> , pH 7.5	1.9	41.8	7.5	1.5×10^9
	Abiotic	1.9	0	7	0
	CV026	1.9	0	7	1.5×10^9
	Aged	1.9	<0.5	7	4×10^4
Biological growth medium	Sample identification	Au NP, ppm	Initial CN^- , ppm	pH	Inoculum, OD_{600}
	Supernatant of <i>C. violaceum</i>	1.9	41.9	7	0
	Washed <i>C. violaceum</i>	1.9	4.0	7	1.7
	Control	1.9	0	7	0
Abiotic buffer	Sample identification	Au NP, ppm	Initial CN^- , ppm	pH	
	NaCN	1.9	9.8	7	
	Control	1.9	0	7	

Results and Discussion

The dissolution of Au NPs in environmental systems is often considered to be negligible.^{153,154,159,192} Indeed, we did not detect Au dissolution while monitoring the dissolution of Au NPs in sterile soil (**Figure 4-2a**). However, when soil was supplemented with a culture of early stationary-phase *C. violaceum*, ~13% Au dissolved after 7 days. Our results support the expected oxidative-dissolution pathway (**Equation 4-1**). The expected dissolution pathway is also supported by the effect of pH: when the pH was raised by 0.5 from 7 to 7.5, in soil containing *C. violaceum*, there was a two-fold increase in dissolved Au, with a maximum dissolution plateau of 30% (**Figure 4-2a**). The increase in Au dissolution in

response to an increase in pH is explained by examining cyanide speciation at these two different pH values: HCN has a pKa value of 9.21, so higher pH would result in higher concentration of free CN⁻. Predicted cyanide speciation at pH 7 is 0.61% ionic form, CN⁻, which is required for the oxidative dissolution and mobility of Au. At pH 7.5, 1.91% of cyanide would exist as CN⁻, about a 3-fold increase (**Table 4-1**). The higher CN⁻ concentration would be expected to lead to higher dissolution. We observed higher initial dissolution and similar first-order rate constants (**Table 4-3**).

To study the relation between the growth of *C. violaceum* and Au NP dissolution, 1 gram of soil inoculated with *C. violaceum*, at pH 7 and aged 7 days, was mixed with 40 g of sterile, Au NP-containing soil (<0.05 mmol CN⁻/g soil and a cell concentration of 4 x 10⁴ CFU/g soil). The onset of dissolution was delayed by a day, but the maximum dissolution plateau reached after 7 days, ~13%, was nearly identical to the maximum dissolution plateau reached when soil was inoculated with the early stationary-phase liquid culture of *C. violaceum* (**Figure 4-2b**).

Quorum sensing regulates HCN production in *C. violaceum*, i.e., the cell concentration must reach a certain density before cyanide synthesis begins. The observation that both experimental designs resulted in about ~13% Au dissolution after 7 days at pH 7 is consistent with quorum sensing controlling CN⁻ production, but doesn't prove it. This association was strengthened, when we grew the QS-mutant CV026 in Au NP-containing soil (**Figure 4-2a**). No Au dissolution was detected.

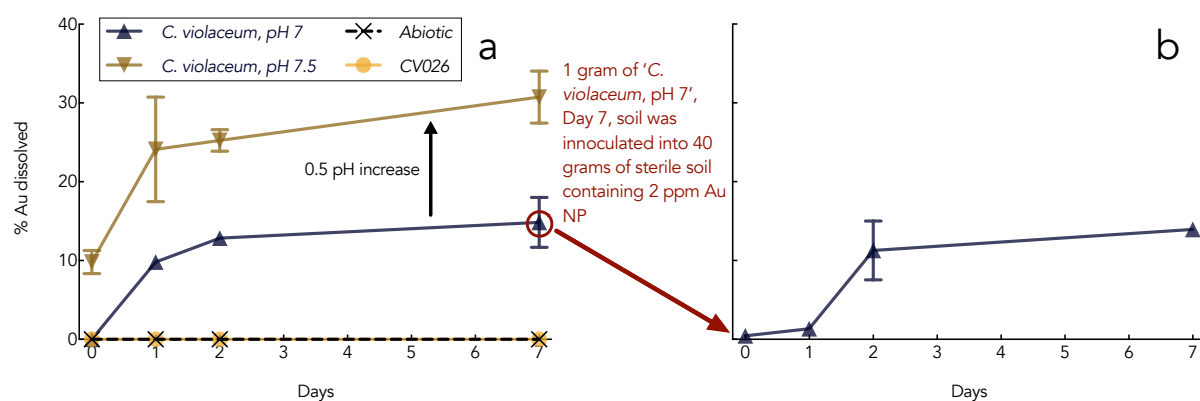


Figure 4-2. (a) Dissolution kinetics of Au NPs in sterile soil, soil supplemented with *C. violaceum*, and soil supplemented with CV026. (b) Dissolution kinetics of Au NPs in initially sterile soil that was supplemented with 2.5% (by weight) soil containing *C. violaceum*. The Y-axis is the same for both (a) and (b), representing the percentage of gold dissolved from a total concentration of 1.9 parts per million.

Table 4-3. The best fit values [average (standard errors)], and R-square values used to describe Au dissolution in the presence of *C. violaceum* at pH 7 and pH 7.5 are presented. The Abiotic control and CV026 presented in **Figure 4-2a** were not modeled.

Best-fit values	<i>C. violaceum</i> , pH 7	<i>C. violaceum</i> , pH 7.5
Dissolution (%) at time zero, Y_0	0.02 (0.21)	10.08 (2.62)
Maximum dissolution plateau (%), Y_{max}	14.78 (0.2)	29.97 (2.55)
First-order rate constant (day^{-1}), k	1.06 (0.05)	0.99 (0.43)
R square	0.99	0.97

Figure 4-3 compares Au NPs dissolution in sterile LB media (*Control*), early-stationary phase cultures of *C. violaceum* that had been washed in LB media (*Washed C. violaceum*), and the supernatant of an early-stationary phase culture of *C. violaceum* (*Supernatant of culture*): this was done to parse the effects of the metabolites (supernatant) from the cells themselves (washed culture). After one day of incubation, the supernatant dissolved ~20% of the Au NPs. Oxidized and soluble gold, dicyanogold $\text{Au}(\text{CN})_2^-$, was detected in the solution (**Figure 4-3b**). The washed culture induce ~1% Au NP dissolution after one day. However, over a 7-day period, *Washed C. violaceum* resulted in 28% dissolution (**Figure 4-4**). Cyanide production and Au dissolution were linearly related over time ($R^2=0.94$, **Figure 4-4a**). Cell growth and Au dissolution were related monotonically, but not linearly (Spearman's $\rho > R^2$, **Figure 4-4b**). Au dissolution increased after a cell density

threshold was achieved, around day 2, characteristic of the delay associated with a cell concentration-based quorum response.

In the abiotic buffer experiments (**Figure 4-5a**), 9.8 ppm of NaCN dissolved 80% of the Au NPs and dicyanogold complexes were measured in the sample (**Figure 4-5b**). No Au dissolution or dicyanogold was detected in the *Control*. In the *Abiotic* cyanide solutions, Au dissolution was fast—about 25% dissolution within seconds of starting the experiment (**Figure 4-6**). Thus, in biological systems, cyanide production is likely to be the rate-limiting step controlling the overall observed dissolution kinetics. This can explain the similar half-life observed for Au NP dissolution in soils with different pH units (**Table 4-3**), and supported by the one-day delay of Au-dissolution in the *Aged* treatment (**Figure 4-2a**).

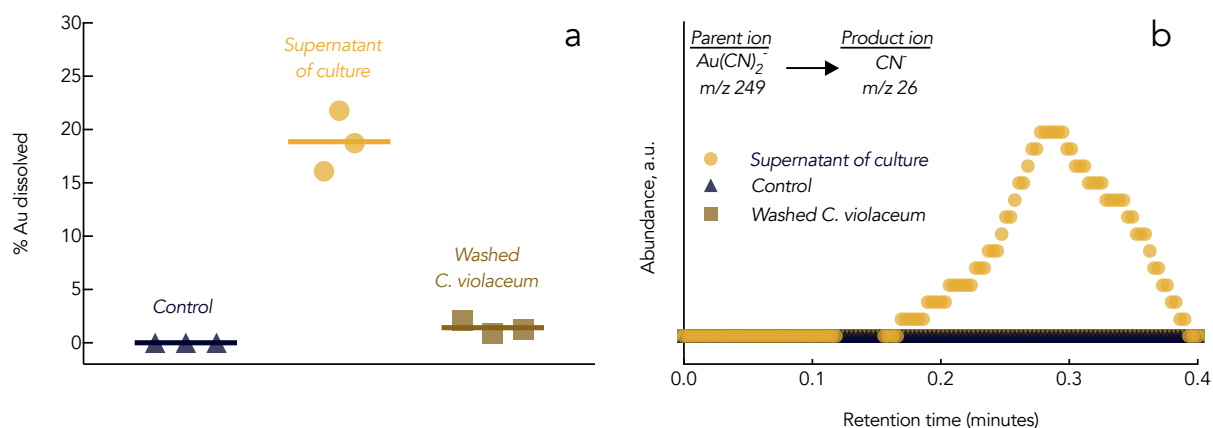


Figure 4-3. (a) Dissolution of Au NP after 24 hours in sterile LB media, early-stationary phase cultures of *C. violaceum* that had been washed in LB media, or the supernatant of an early-stationary stage culture of *C. violaceum*. Y-axis represents the percentage of gold dissolved from a total concentration of 1.9 parts per million. (b) Detection of dicyanogold, $\text{Au}(\text{CN})_2^-$ using an ESI-MS/MS procedure by monitoring the cyanide product ion, m/z 26, of the dicyanogold parent ion, m/z 249.

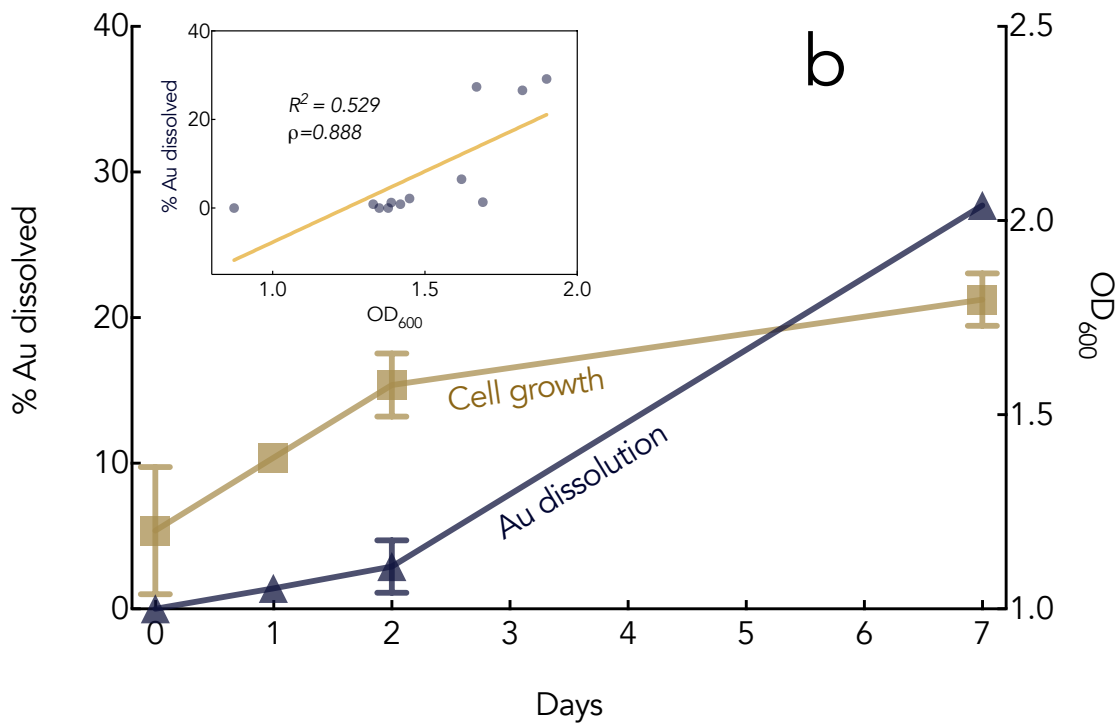
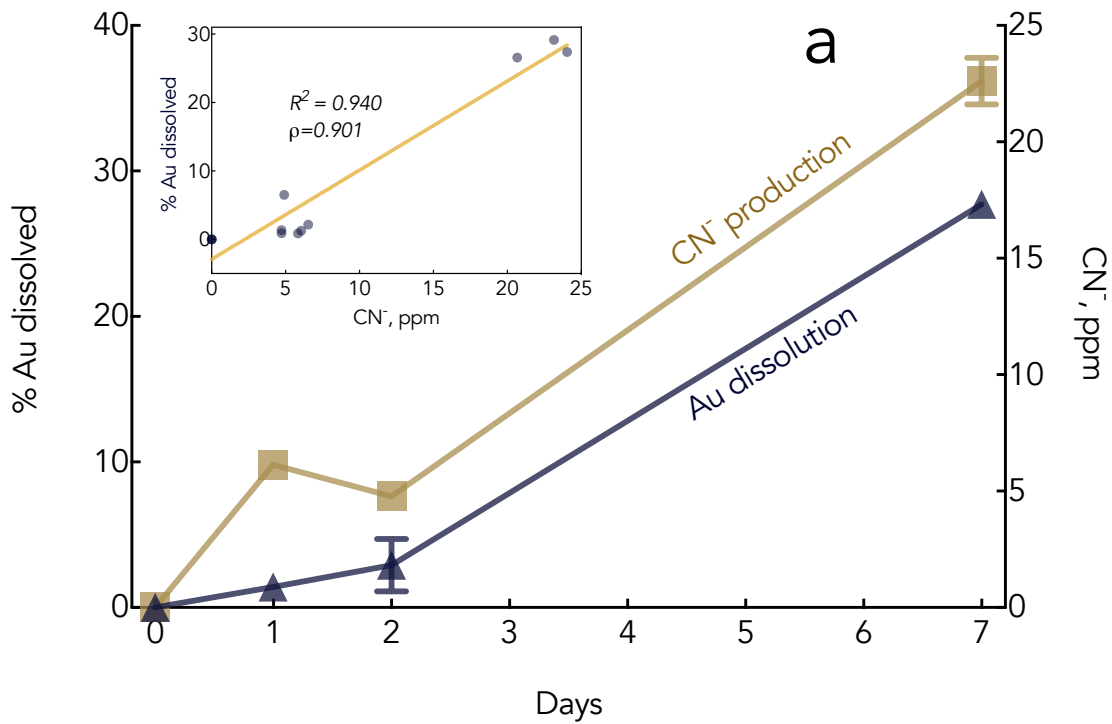


Figure 4-4. (a) Au NP dissolution (%) and cyanide production over time with an inlay that plots Au dissolution versus CN⁻. (b) Au dissolution (%) and cell growth over time with an inlay that plots Au dissolution versus OD₆₀₀. The values in the inlay represent the R² and Spearman's rho (ρ)

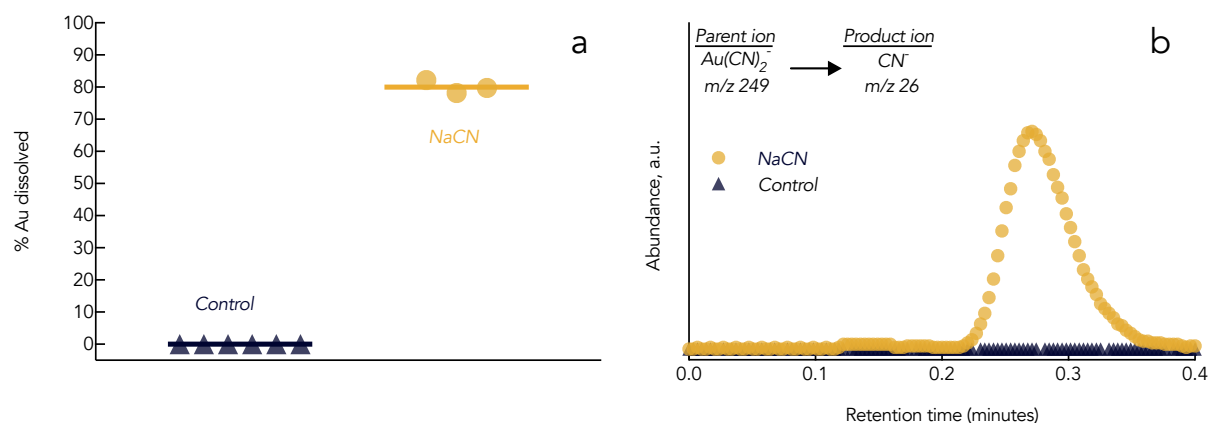


Figure 4-5. (a) Dissolution of Au NP after 24 hours in sterile buffer or NaCN solution. (b) Detection of dicyanogold, $\text{Au}(\text{CN})_2^-$. Y-axis for (a) represent the percentage of gold dissolved from a total concentration of 1.9 parts per million.

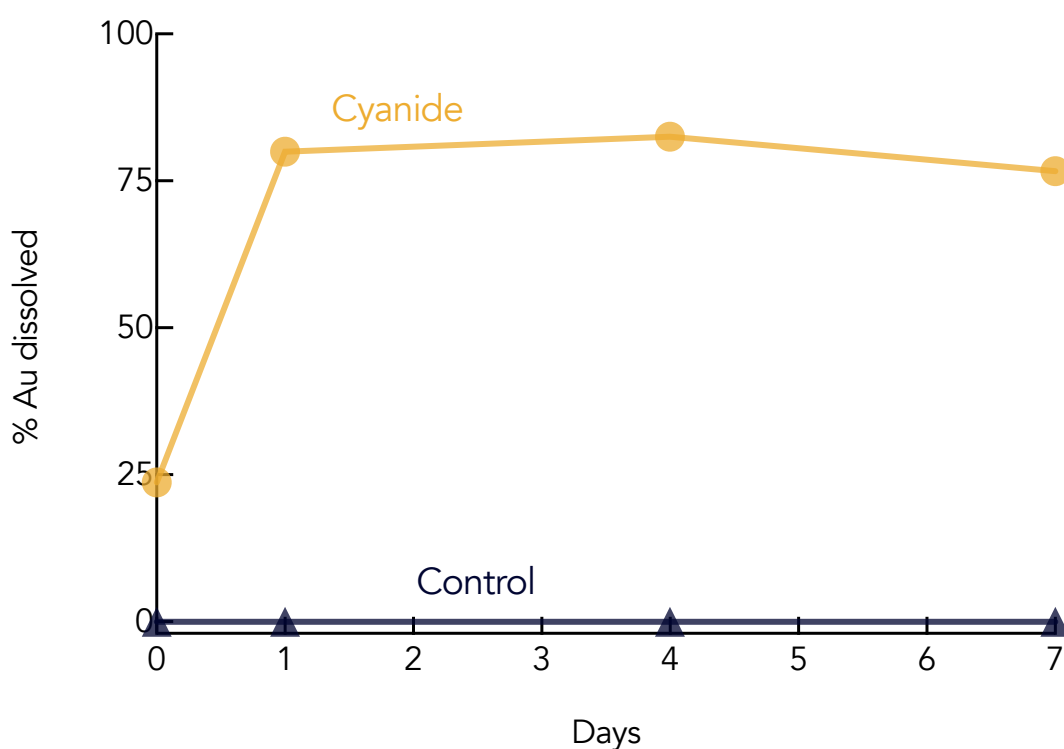


Figure 4-6. Au NP dissolution (%) over time in a sterile buffer (Control, pH 7) and a cyanide solution (9.8 ppm, pH 7).

Conclusions

Au NPs were oxidized and solubilized to $\text{Au}(\text{CN})_2^-$ by *C. violaceum* in soil. Au NP dissolution was limited by QS-regulated CN^- production. *C. violaceum* is just one cyanogenic organism. Species of *Pseudomonas*, *Rhizobium*, and several cyanobacteria are also

cyanogenetic¹⁷⁴, in addition to many plants¹⁹³, and some species of fungi.¹⁶⁴ Environmental cyanide concentrations are generally low in surface waters (ppb-level).¹⁶⁴ However, bacteria are capable of forming dense biofilms where cyanide concentrations can reach ppm-levels.¹⁷⁵ This is interesting because a study on NP distribution in estuarine environments found that uncharacterized biofilms were the major sink for Au nanorods.¹⁵³ This study also reported high pH values (7.9–8.5) and dissolved oxygen levels between 4–12 mg/L; these conditions are favorable to cyanide-induced oxidative dissolution. Another important environmental factor to consider is the presence of glycine. Glycine is a common amino acid and the direct metabolic precursor of cyanide production in bacteria and fungi.¹⁸⁷ In this work, we did not study the effects of glycine concentration, nor methyl-group donors that stimulate the oxidative decarboxylation of glycine, on Au NP dissolution. This could be a subject of future study.

Although extensive efforts have been made to standardize the methods to characterize engineered NP properties in the environment, including the dissolution of NPs in different environmental media, the role of bacteria on these properties has been overlooked.¹⁵¹ In light of the findings of this chapter, future studies that use Au NPs as a tracer to investigate aggregation behavior or NP uptake should rule out the possibility of cyanogenic organisms, or take this into account. Furthermore, the results presented here suggest that when Au NPs are used in environmental applications, they could solubilize and enter the biogeochemical cycle of Au.

5. Implications and remaining questions

Bacteria have evolved communication systems that enable coordinated behaviors that enhance survival. Communication among cells involves chemical signals or secondary metabolites that enter the environment, where they are detected through reactions with receptors on neighboring cells. These extracellular signaling molecules interact with the local biogeochemistry of the environment. Due to the ecological and human health implications of bacterial cell-to-cell communication, understanding the impacts that NPs have on these systems requires attention.

There are many challenges when trying to understand environmental implications of NP exposure.¹⁹⁴ Physiochemical transformations of NPs (homoaggregation, heteroaggregation, dissolution, chemical reactions, and adsorption of macromolecules) are especially important to consider in the context of the results presented in this dissertation. The aggregation of NPs to themselves (homoaggregation) or with naturally occurring materials (heteroaggregation) is often predicted by Derjaguin-Landau-Verwey-Overbeek models, which account for van der Waals, electrostatic, steric, and acid/base interactions. However, predicting behavior in complex systems, such as the heteroaggregation between TiO₂ NPs and lysing cells we observed in Chapter 2, is difficult due to the inhomogeneity of the macromolecule coatings that NPs will acquire in natural systems. The adsorption of natural macromolecules influences the macromolecules as well as the fate and toxicity of the NP. With the exception of the gold dissolution studies in soil (Chapter 4), the experiments presented in this dissertation were in simplified systems, lacking biological macromolecules that NPs would be exposed to in the environment (e.g., humic matter and proteins). The competitive stability constants and adsorption kinetics between NPs and biological molecules

requires further study to accurately predict the relevant transformations and biological impacts. Dissolution and chemical transformations are also an important to consider in biological NP studies. As we discussed in Chapters 3 and 4, the dissolution of a NP is responsible for its biological activity and environmental persistence. In the case of metal oxides (e.g., CuO NPs), dissolution is often accelerated in acidic pH conditions. For other NPs, such as Au, chemical transformations (e.g., oxidation) predict dissolution behavior. Due to the complexity of physiochemical transformations of NPs, accurately predicting biological impacts is complex, but the empirical evidence we present here provides novel insight into bacterial–NP interactions.

The overall goal of this thesis was to improve understanding of the relationship between NPs and cell-to-cell signaling behavior in bacteria. We approached this goal by focusing on two population-level behaviors: autolysis and quorum sensing. Specifically, we sought to: (1) improve our understanding of how metal-oxide NPs affect the autolytic process in *B. subtilis*, by elucidating the biological response of the interactions between TiO₂ NPs and biomolecules; (2) reveal the interactions between a QS signaling molecule and metal cations commonly used in antimicrobial NPs, silver (Ag⁺) and copper (Cu²⁺); and (3) demonstrate the potential of QS-regulated cyanide production to affect oxidation and dissolution of gold NPs an environmentally-relevant system. By addressing these objectives, this work demonstrated that:

1. **TiO₂ NPs disrupt the autolytic process by delaying the onset of autolysis, and intercepting released autolytic enzymes, preventing the enzymes from degrading the cell wall of neighboring cells.** Chapter 2 presents the first account of NPs disrupting autolysis. However, the observation that TiO₂ NPs increase cell survivability is not entirely novel. The protective role of TiO₂ NPs has been exploited for various bioencapsulation purposes (e.g., lymphocyte

delivery for cancer treatment¹⁹⁵ and delivering beneficial bacteria to plant roots for increased crop yield and stress management¹⁹⁶); however, none of these applications have linked survivability to the disruption of autolysis. Furthermore, our results present a novel mechanism: that TiO₂ NP deposition on cell walls/teichoic acids prevent the onset of autolysis. However, initial interest has focused on the observed affinity of NP aggregates to the surface of *B. subtilis*, and how this may promote the activity of rhizobacteria for plant growth.¹⁹⁷

- 2. QS signaling molecules form complexes with Ag⁺ and Cu²⁺, removing the most bioavailable form (free signal, Ag⁺, and Cu²⁺) from the cells environment.** This is the first account of unhydrolyzed QS signals complexing metal ions. The novel complex we describe in Chapter 3 suggests a need to consider QS signal-metal interactions in environmental studies (where metal concentrations are high), and in studies that investigate metals as potential quorum quenching agents. If QS signals, which are constitutively produced by many bacteria, act as chelating agents in the environment, QS may play a role more generally in metal cycling, bioavailability, toxicity, uptake, fate, and transport. Further research is needed to address the scope and implications of this observation in nature. Kaufmann et al. (2005) suggested that hydrolyzed AHLs might be “primordial siderophores”, but our work represents the first time unhydrolyzed AHLs have been shown to complex metal ions.
- 3. QS-regulated cyanide production induces oxidative dissolution in Au NPs, which were previously assumed to be inert in environmental systems.** In Chapter 4, the biodissolution of Au NPs was linked to QS-regulated CN⁻

production in *C. violaceum*. This demonstrates that Au NPs may not be inert environmental tracers, and that cyanogenic organisms may affect their ecological fate. Given these results, researchers should review prior work to determine whether the effects of cyanogenic organisms might explain observations in studies that assumed Au NPs were inert in biological systems. Furthermore, future work should consider cyanogenic organisms when using Au NPs in natural systems. There are other types of NPs that may be susceptible to biodissolution as well, either from cyanide or other released metabolites from bacteria (See Appendix B: CuO nanoparticle dissolution by a siderophore-emitting bacteria and a cyanogenic bacteria). For example, bacteria often produce siderophores¹⁹⁸, which can chelate iron or copper, potentially affecting the dissolution of Cu or Fe based NPs. Taking advantage of biodissolution could be explored as an application, e.g. dissolving nano-enabled agrochemicals^{2,199} can provide nutrients to plants, but in calcareous soils dissolution is limited.

Taken together, this body of work highlights the relationship between NPs and population-level behavior in bacteria. The presence of NPs can have significant impacts on population-level behaviors, and the activity of population-level behaviors can have significant impacts on NP behavior. This inter-connected relationship, where the NPs are both acted on and act upon their environment, must be considered in NP-based studies and applications.

Appendix A: Additional nanoparticle–bacteria interactions

The importance of quorum sensing in ecological and human health settings has been described in Chapter 1, as has the emergence of nanoparticles as a potential environmental contaminant. Most literature on the topic of QS-nano interactions has focused on NPs that release antibacterial ions (e.g., Ag- and Cu-based NPs^{128–130,146,200}) or NPs that have been functionalized with AHL-quenching compounds.¹²⁶ However, none of these works have investigated the interaction of AHLs with NP surfaces, even though there is significant evidence that similarly structured compounds adsorb to NPs. The chemical structure of AHLs contains a lactone-ring with a hydrocarbon –R group side chains (**Table 1-1**). AHL molecules also resemble surfactants, which are often employed to stabilize and disperse nanoparticles, especially NPs with hydrophobic surfaces, e.g., carbon nanotubes.^{201–203} Similarly structured amphipathic surfactant compounds have been shown to adsorb NPs and influence their surface chemistry.^{204–206} In general, the physiochemical interactions (influenced by London-Dispersion and electrostatic forces) and the hydrodynamic forces influence a particle's attachment to a surface. Depending on the chemistry of the surfactant molecule and the nanoparticle surface properties.^{202,207–209} One specific study noted that AHLs, which are nonionic amphipathic molecules, were retained on glass beads and organic plant material according to the length, and thus hydrophobicity, of the hydrocarbon –R group side chain.²¹⁰ However, neither adsorption isotherms nor rates were reported in this study, but a positive correlation was found between increasing hydrophobicity of AHL –R groups and mass retained on organic surfaces. This finding suggests that AHLs may also be retained on NPs due to hydrophobic interactions. However, there are no studies looking at the interactions between AHLs and NP surfaces. Thus, we initially studied the interactions between NPs that

do not release toxic ions: TiO₂, CeO₂, MWCNTs, and C₆₀, and how their adsorption may alter QS activity. The objectives of this early work were to assess the adsorptive properties, and subsequent biological activity, when AHLs are exposed to NPs. A few noteworthy observations were made:

1. MWCNTs had a higher absorption capacity for HHL compared to TiO₂ NPs;
2. when sonicated together, *N*-hexanoyl homoserine lactone stabilized MWCNTs in suspension;
3. when sonicated together, *N*-3-(oxododecanoyl) homoserine lactone (ODdHL) reduced the hydrodynamic radius of TiO₂ NPs suspensions;
4. MWCNTs *increased* QS-regulated violacein production in *C. violaceum*, and;
5. FeCl₃ induced violaceum synthesis in CV026.

MWCNTs had a higher absorption capacity for HHL compared to TiO₂ NPs

Adsorption isotherms were created for HHL on TiO₂ and MWCNTs (**Figure A-1**). Fit to a Langmuir isotherm, the adsorptive capacities, q_{max} , and equilibrium constants, K_L , were calculated (**Table A-1**) according to:

Equation A-1

$$q = \frac{q_{max} \times K_L \times C_{eq}}{1 + K_L \times C_{eq}}$$

where q is the adsorbed mass in mg/m² and C_{eq} is the dissolved mass in solutions.

MWCNT ($q_{max}=2.05$ mg/m²) have a higher adsorptive capacity for HHL than TiO₂ ($q_{max}=4.16 \times 10^{-3}$ mg/m²). The strong adsorption by MWCNTs is not surprising, as CNTs are often used to adsorb organic compounds due to their high hydrophobicity.²⁰¹ The adsorption is likely driven by van der Waal interactions between the MWCNT surface and hydrophobic tail of the HHL, which would leave the more hydrophilic end of the AHL exposed to the aqueous media. This is supported by the observation that when sonicated together, HHLs stabilized MWCNTs

in suspension (**Figure A-1** and **Movie A1**: <https://www.youtube.com/watch?v=TsTkVGT28cc>).

When sonicated together, the QS signal ODDHL reduced the hydrodynamic radius of TiO₂ NPs suspensions. TiO₂ dispersions formed smaller aggregations, 10.3 nm radius, when sonicated in ODDHL, compared to a bimodal distribution, 43.2 and 232 radii, when sonicated in the same buffer without ODDHL (**Figure A-2**).

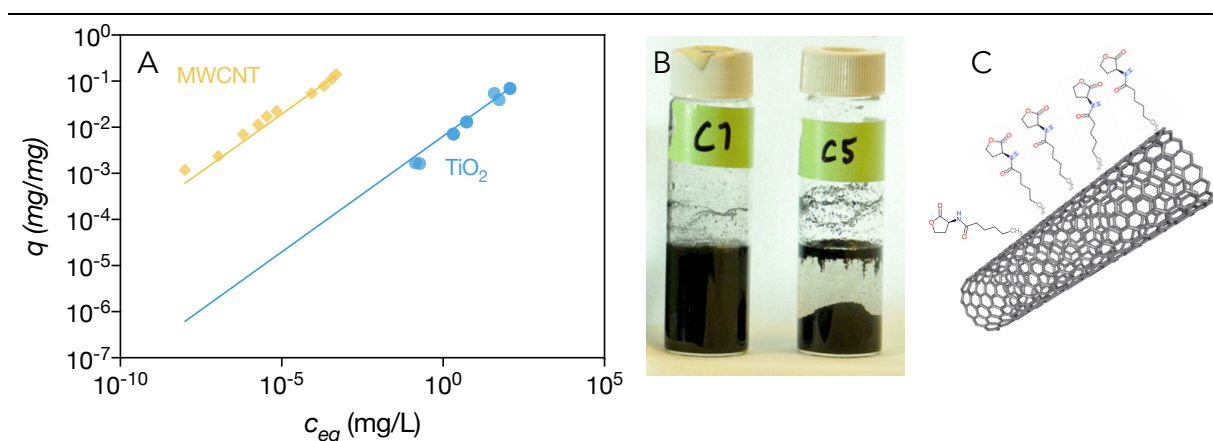


Figure A-1. (A) Adsorption isotherms of HHL to MWCNTs and TiO₂. (B) Suspensions of MWCNTs 10 minutes after sonication with HHL (C1) and without HHL (C5). (C) Proposed interaction between HHL and MWCNTs.

Table A-1. Best fit parameters used to describe HHL adsorption to MWCNTs and TiO₂.

Langmuir best-fit parameter	q_{max}	K_L	R^2
MWCNT	2.058	0.015	0.963
TiO ₂	0.004	0.031	0.961

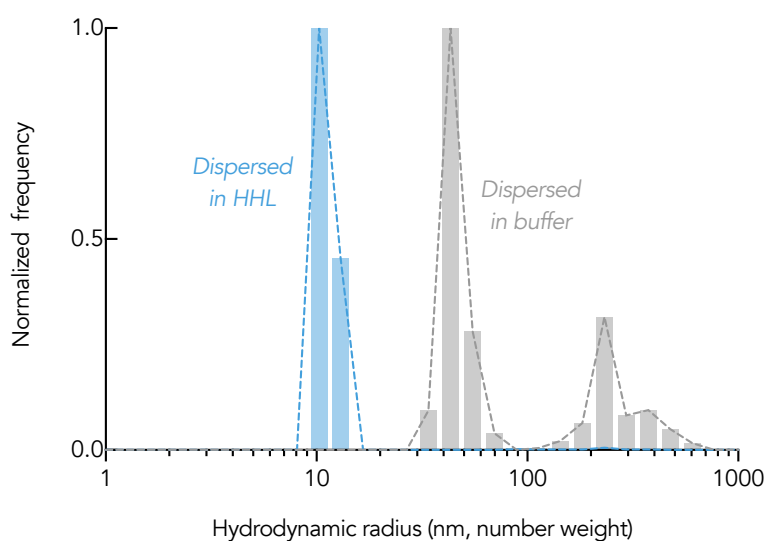


Figure A-2. Difference in hydrodynamic radius of TiO₂ NP suspensions after sonication with and without ODDHL.

Supernatant from MWCNT adsorption experiment were then aliquoted in CV026 well-diffusion plate assays. *C. violaceum* CV026 is a mutant strain that is unable to produce its own QS signaling molecules, therefore it does not produce violacein even when bacterial numbers exceed the quorum threshold. However, when added exogenously, HHL can induce violacein production. Supernatants of the HHL+NP adsorption samples were tested on an AHL reporter plate assay (**Figure A-3**). Briefly, LB agar was inoculated with *C. violaceum* CV026 and samples to be tested were added to a small hole that was bored in the center of the agar plate. After incubation, the formation of a purple ring around the added sample indicates the presence of QS-inducing AHLs in a diameter-dependent manner. Preliminary results using the AHL reporter plate assay showed that the degree of QS-induced violacein production was negatively correlated to the ratio of MWCNTs:HHL (**Figure A-4**). These results suggest that AHLs can adsorb to hydrophobic surfaces, and the decrease in free AHL concentration results in a decrease in QS activity.

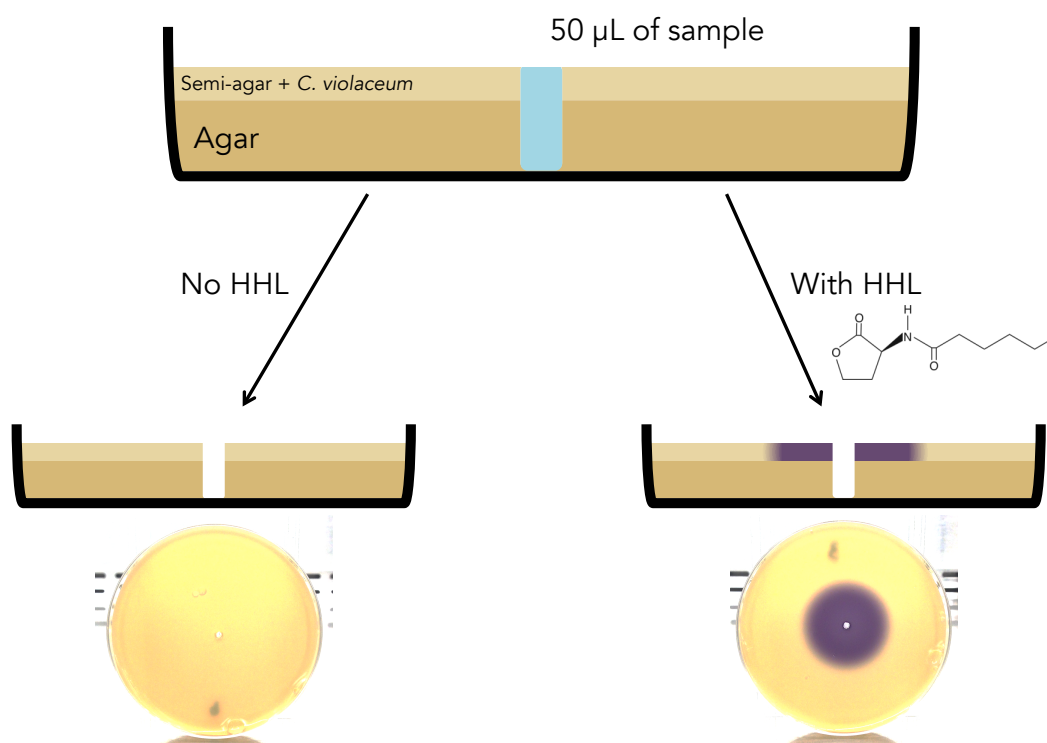


Figure A-3. HHL reporter plate assay. LB agar plates inoculated with CV026 turn purple around the added sample if HHL is present.

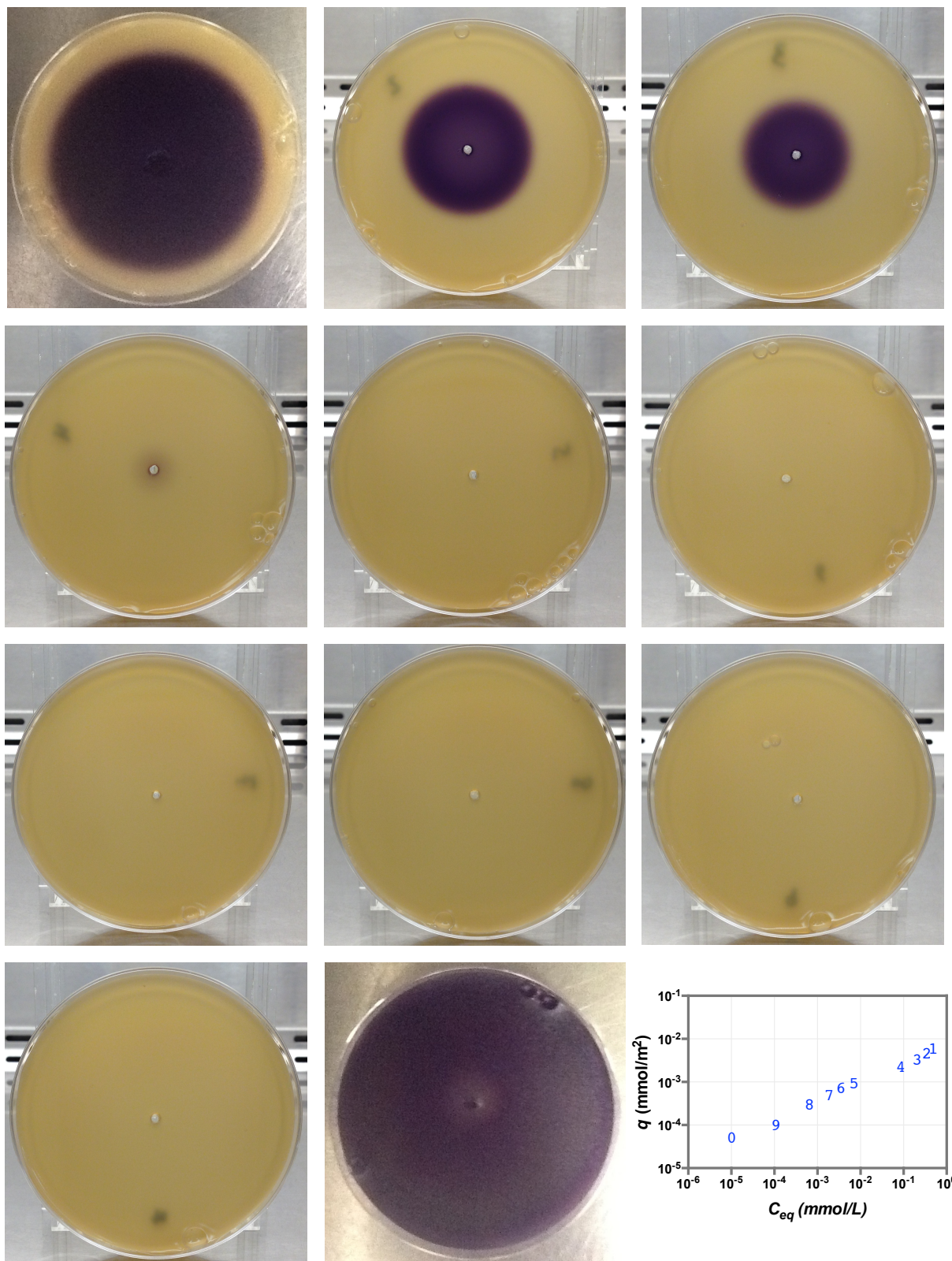


Figure A-4. HHL reporter plate assay. A purple ring indicates that HHL is present in the well. This is a semi-quantitative way to determine relative HHL concentrations and their biological activity.

MWCNTs increased QS-regulated violacein production in *C. violaceum*

NP toxicity and QS inhibition was studied in wild-type *C. violaceum*. In these liquid culture experiments, *C. violaceum* was dosed with 100 ppm NP and the change in cell viability and violacein production was measured after 24 hours (**Figure A-5**). None of the tested NPs had an impact on cell viability. Interestingly, the only NP that significantly affected violacein production was MWCNTs. However, the effect was the opposite of what was expected: MWCNTs resulted in an *increase* in QS activity. This contradicts the adsorption and CV026 results above. Controls show that MWCNTs did not interfere with the fluorescence assay (**Figure A-6**).

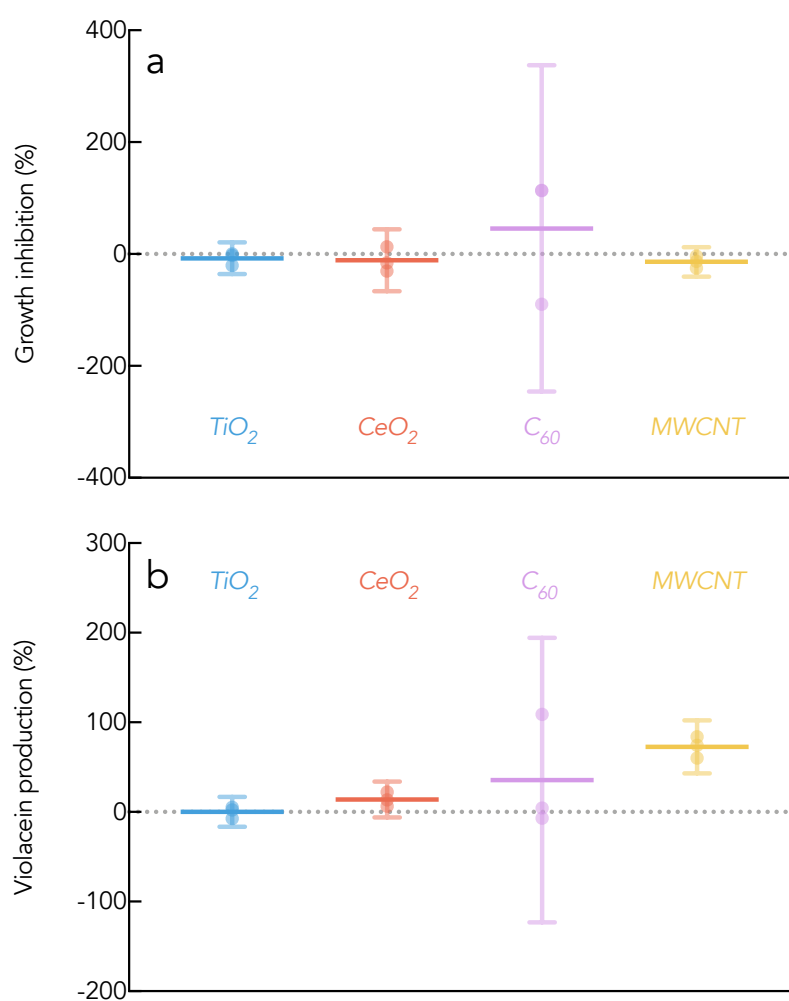


Figure A-5. (a) Growth inhibition of *C. violaceum* wild-type after being incubated for 24 hours in the presence of various NPs (100 ppm), relative to a no-NP control (dotted-line). Violacein production in of *C. violaceum* wild-type after being incubated for 24 hours in the presence of various NPs (100 ppm), relative to a no-NP control (dotted-line)

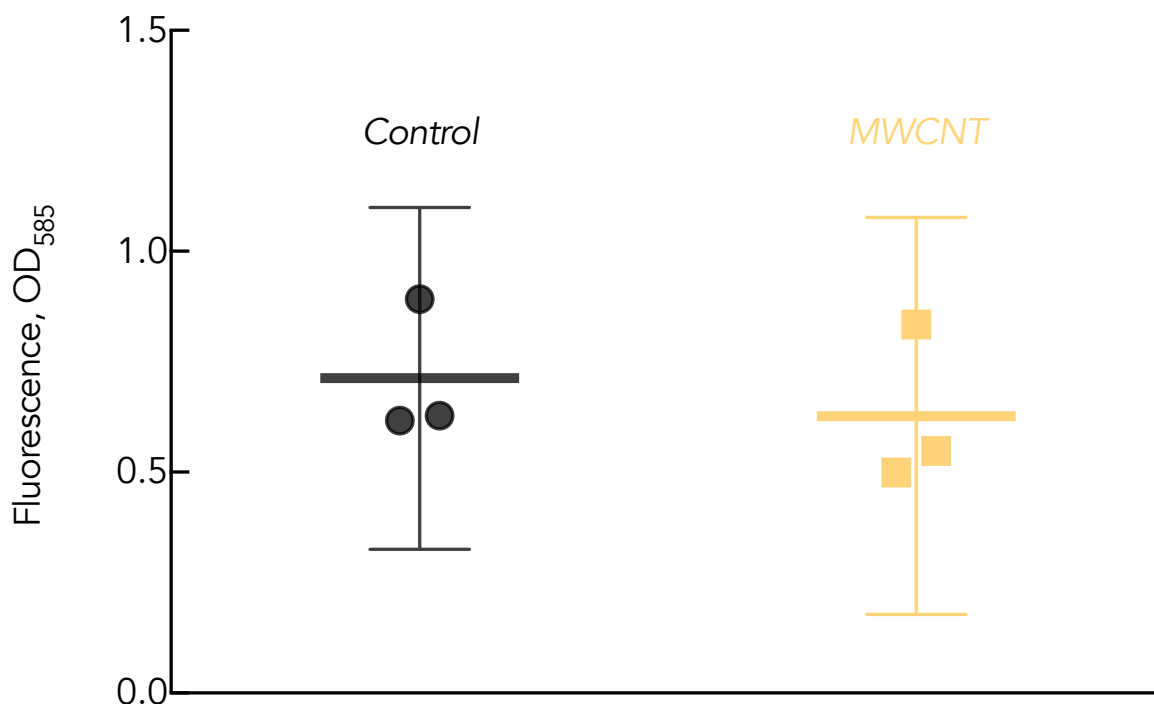


Figure A-6. Violaceum production is measured via fluorescence at nm=585. To verify that the increase in violacein production presented in **Figure A-5**, was not due to MWCNTs interference with fluorescence, we added 100 ppm of MWCNTs to extracted violaceum.

FeCl₃ induced violaceum synthesis in CV026

One hypothesis to explain the increase in violacein production in response to MWCNT exposure is that oxidative stress increases violacein production. MWCNTs were purchased from Cheaptubes.com and used *as received*. Several sources have found that Fe impurities are common in these materials^{211,212}, and that these Fe impurities result in cellular oxidative stress.²¹³ Interestingly, when CV026, the mutant strain that is unable to synthesize its own QS signals, was exposed to FeCl₃, violacein was synthesized (**Figure A-7**). In *C. violaceum*, violacein synthesis is regulated by the HHL CviI/R quorum sensing system. As far as we are aware, the only pathway to violacein synthesis in CV026 is via the addition of HHL to induce QS. There are two hypotheses to explain this observation: (1) The FeCl₃ contained HHL contamination, or (2) FeCl₃ is inducing violacein synthesis via an unknown pathway. The first hypothesis was ruled out once the experiment was repeated using a different batch of FeCl₃ salts. Fe-induced violacein production should be explored further. Fe³⁺ has been shown to

induce antioxidant production in *Saccharomyces cerevisiae* previously (not regulated by QS).²¹⁴

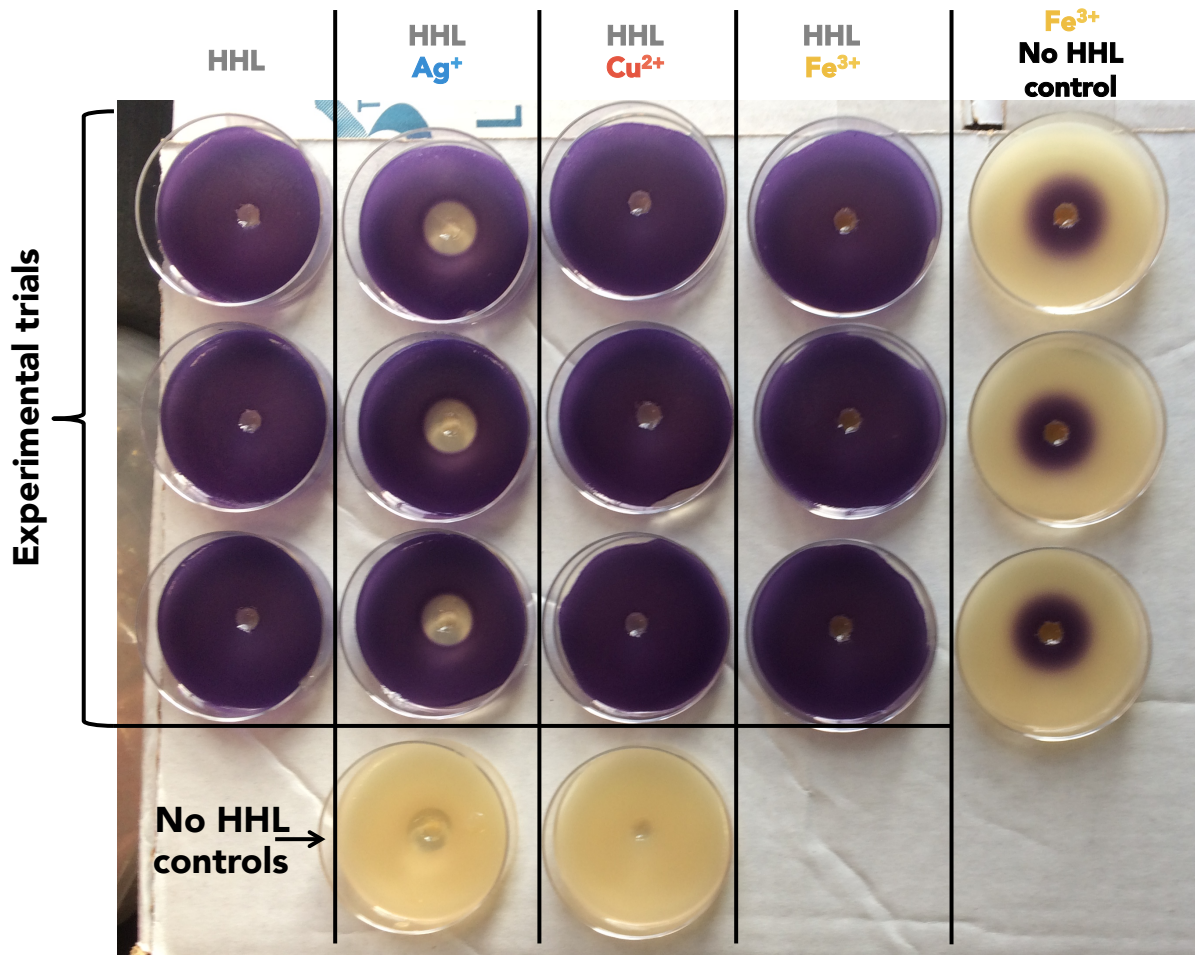


Figure A-7. Well diffuse assay demonstrating that FeCl₃ induced violacein synthesis in the QS-mutant CV026.

We evaluated the influence of surface charge on autolysis by exposing starving cultures of *B. subtilis* to CeO₂ NPs functionalized with positively charged, negatively charged, and neutral dextran coatings (described previously²¹⁵). These preliminary results suggest that negatively charged and neutral surface chemistry disrupts autolysis, whereas the positively charged surface had no impact (**Figure A-8**). This experiment was run identical to the experiment described in Chapter 2 Methods.

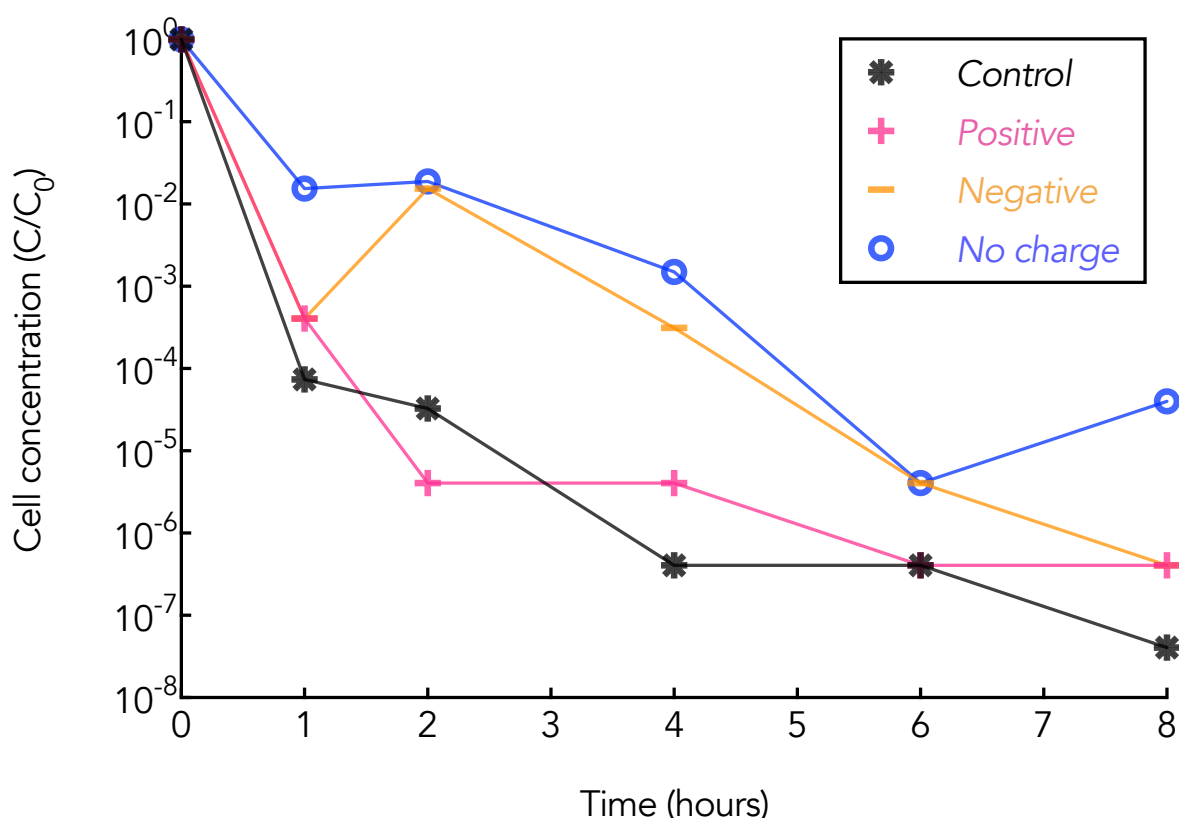


Figure A-8. Colony Forming Unit (C) over time normalized to the initial Colony Forming Unit of each series (C₀) of *B. subtilis* in 5 mM NaHCO₃ buffer (pH 7.7) with exposure to 50 ppm CeO₂ containing various coatings.

Appendix B: CuO nanoparticle dissolution by a siderophore-emitting bacteria and a cyanogenic bacteria

The dissolution of a metal nanoparticle (NP) in a given system is responsible for its fate, transport, and mode of action.^{2,20,149,150} For example, the perceived stability of a gold NPs is critical to its utility in biological imaging probes²¹⁶, drug delivery¹, and environmental tracer studies^{153–155} (Discussed in Chapter 4). Copper-based NPs, on the other hand, are effective pesticides²¹⁷, fertilizers^{199,218,219}, and antimicrobial agents¹²⁴ due to their dissolution, releasing the most bioavailable form of copper, Cu²⁺.

One major user of environmental nanotechnology is the agrochemical industry. Nano-scale agrochemicals are becoming popular because of their tunable nutrient release, targeted delivery, and concomitant decrease in applied loads.^{150,199,220} Copper-based NPs are used because Cu is a micronutrient and antimicrobial.²¹⁸ As a fertilizer, CuO NPs increased tomato and eggplant yields.²¹⁹ As a fungicide/bactericide, DuPont's copper-based Kocide 3000 is used globally. Regardless of its use, the success of copper-based NPs depends upon Cu²⁺ dissolution, which, in agricultural applications, is often limited by the soil pH. In calcareous soil regions (e.g., Australia, central Europe and western United States) high pH limits Cu dissolution and thus the efficacy of the nanoenabled product.²²¹ One study increased the fraction of labile Cu in a calcareous soil with the addition of pyoverdine (Pvd), a common siderophore²²², which led us to wonder—could Pvd-emitting bacterium increase CuO NP dissolution in high-pH soils to increase the efficiency of Cu-based agrochemicals?

Pseudomonas fluorescens

CuO NP dissolution was measured in the presence and absence of *P. fluorescens* at pH 7. These parameters were chosen because pyoverdine has a high stability constant with Cu

($10^{20.1}$)³¹, and high pH soils result in low solubility of Cu. For each treatment, 300 g of soil was supplemented with 26 mg CuO NPs supplemented in 32 mL of succinate media immediately after sonication (3 x 10s pulses at power level 3, **Figure 2-1**) and mixed for 10 minutes by hand. The CuO amended soil was then weighed into three different batches: 120 g, 120 g, and 80 g, to be further amended with 9.6 mL *P. fluorescens* (culture), 9.6 mL washed *P. fluorescens* (washed), or 6.4 mL of succinate media (control), respectively. Once thoroughly mixed, the samples were sealed with alcohol-sterilized parafilm and incubated for 21 days (at 30°C).

Two different extraction methods were used to quantify Cu dissolution and availability in CuO NP amended soil: a DTPA-extraction, and a CaCl₂-extraction. The DTPA method can measure the dissolution of CuO NP in soil because it can extract most of the Cu ions (free Cu ions, Cu bond to carbonate and organic matter) in soil.^{180,223} The DTPA-extraction results are presented in **Figure B-1**. Over a 21-day period, Cu in sterile soil (Abiotic) slightly rose from 5% to 10%; the “Washed *P. fluorescens*” treatment increased Cu dissolution to 27%; and the “*P. fluorescens*” treatment resulted in 9% CuO dissolution. Numerous researchers have shown that in calcareous soils, Cu phytoavailability is limited by strong sorption to the solid phase.^{222,224,225} We’ve shown here that *P. fluorescens* can increase the release of copper from CuO NPs in soils. Perhaps when the unwashed treatment is added to the soil, the existence of the siderophores prevents the cells from producing more, whereas in the washed culture, where siderophores are removed before the addition to soil, siderophore production is increased, resulting in higher Cu dissolution. Previous studies have shown that Pvd can increase phytoavailable Cu in calcareous soils²²².

The CaCl₂-extractable Cu is presented in **Figure B-1**. CaCl₂-extractions are commonly used to measure metal concentrations in soil pore water, referred to as the *readily-available* metal pool. Similar to the DTPA-extraction results, the “Washed *P. fluorescens*” treatment

resulted in the highest Cu dissolution, about 2.5% after 21 days. The *P. fluorescens* and Abiotic treatments reached 1% and 1.5% CuO dissolution, respectively. The combined results show that a washed culture of *P. fluorescens* can increase the fraction of copper that is phytoavailable and increase porewater concentration. Extractable Al, Mn, and Fe were also measured and are presented in **Figure B-2**.

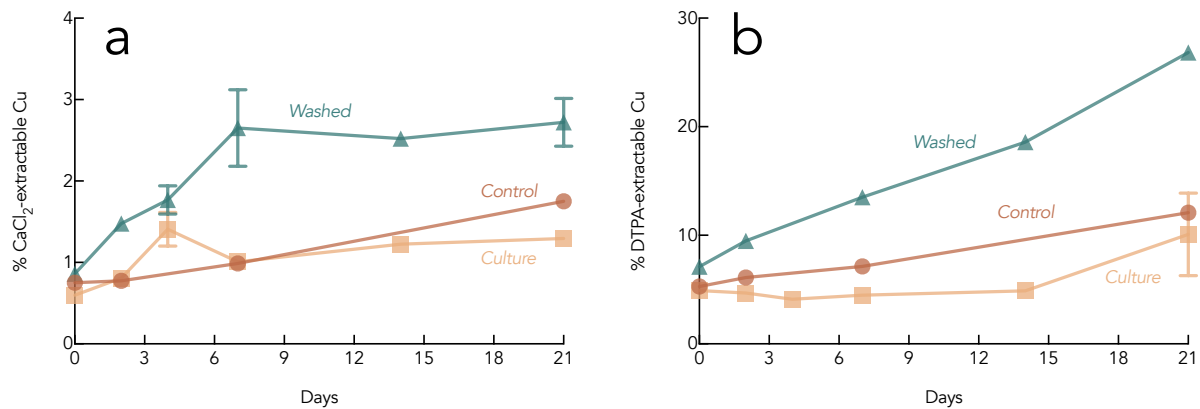


Figure B-1. Two different extraction methods were used to quantify Cu dissolution from CuO NPs in sterile soil (Abiotic, copper circle), soil supplemented with a 5-day culture of *Pseudomonas fluorescens* (green triangle), and soil supplemented with a washed 5-day culture of *P. fluorescens* (beige square). (a) Extractable Cu using 0.005 M diethylenetriaminepentaacetic acid (DTPA). (b) Extractable Cu using 0.01 M CaCl₂. The Y-axis is the same for both (a) and (b), representing the percentage of Cu dissolved from a total concentration of 11 parts per million as CuO NPs. The soil moisture content was maintained at 16% across all treatments.

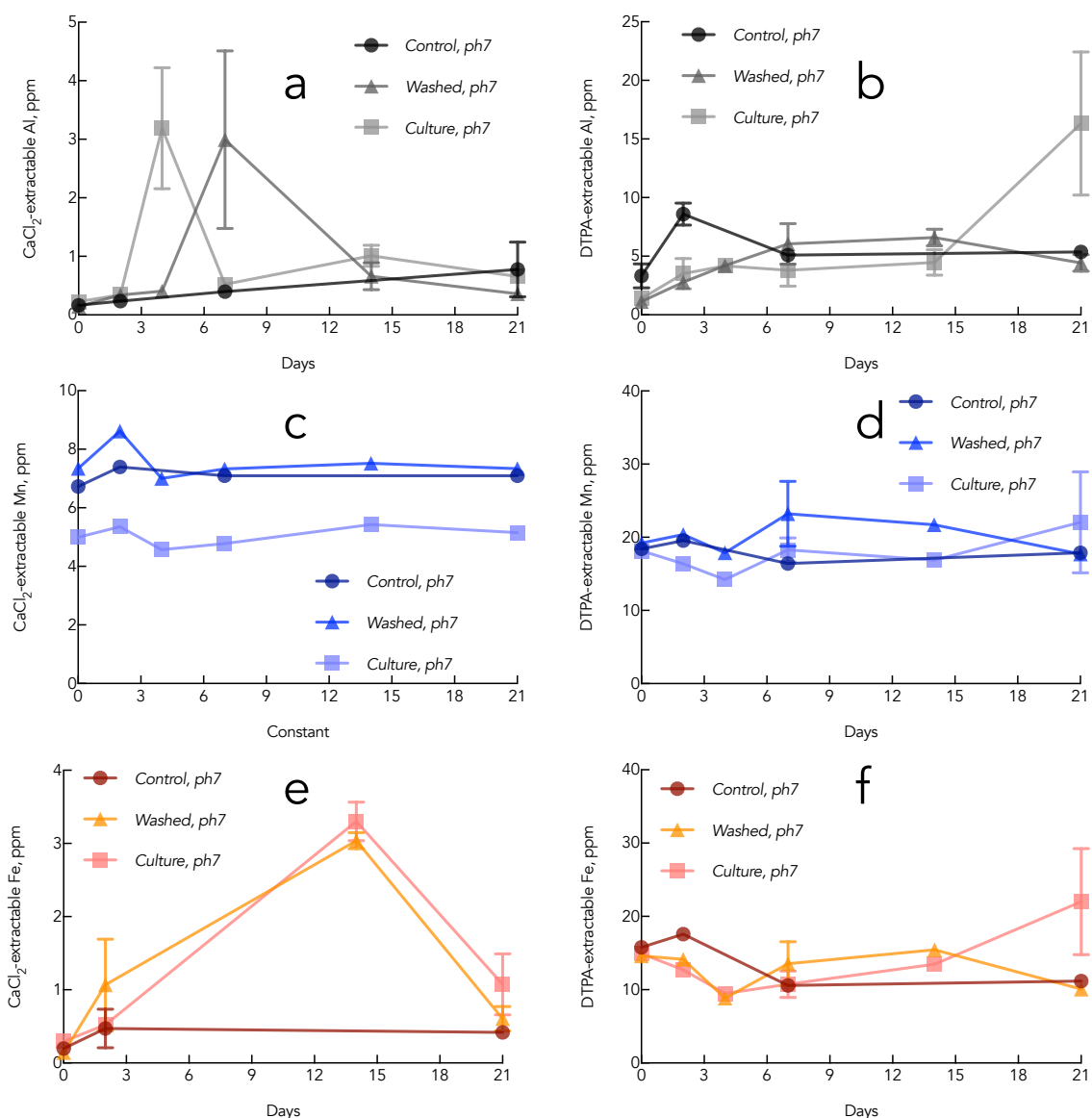


Figure B-2. Extractable Al, Mn, and Fe from soil after inoculation with *P. fluorescens*.

Chromobacterium violaceum

Next, we tested the influence of a cyanogenic organism on CuO NP dissolution. These experiments were carried out identically to the experiments described in Chapter 4 Methods. Briefly, a live culture of *C. violaceum* or its supernatant (metabolites without cells) on CuO NP dissolution was studied at pH 7. *C. violaceum* was grown to 10^{10} CFU/mL, centrifuged, and the supernatant was filtered (0.22 μ m, PTFE) into sterile 50 mL tubes and used as the *Supernatant* exposure media. The pellets were then resuspended in equivalent volume of fresh growth media to be used as the *Cells* treatment. Separately, sterile growth media was used as

the *Control* treatment. 7.9 ppm CuO NPs were added to each treatment. Initial CN⁻ concentrations in the *Supernatant*, *Cells*, and *Control* samples were 41.87 ppm (standard deviation: 0.90), 4.05 ppm (standard deviation: 0.60), and 0 ppm, respectively.

Incubating CuO NPs in the supernatant resulted in 100% dissolution after 2 days (**Figure B-3**), CuO NPs in the control LB media plateaued at 78% dissolution after 2 days, and the washed cells resulted in 42% dissolution after 7 days. The difference between the *Cells* and *Control* curves in **Figure B-3** may be attributed to CuO NP deposition on cell walls and toxicity to cells (not tested).

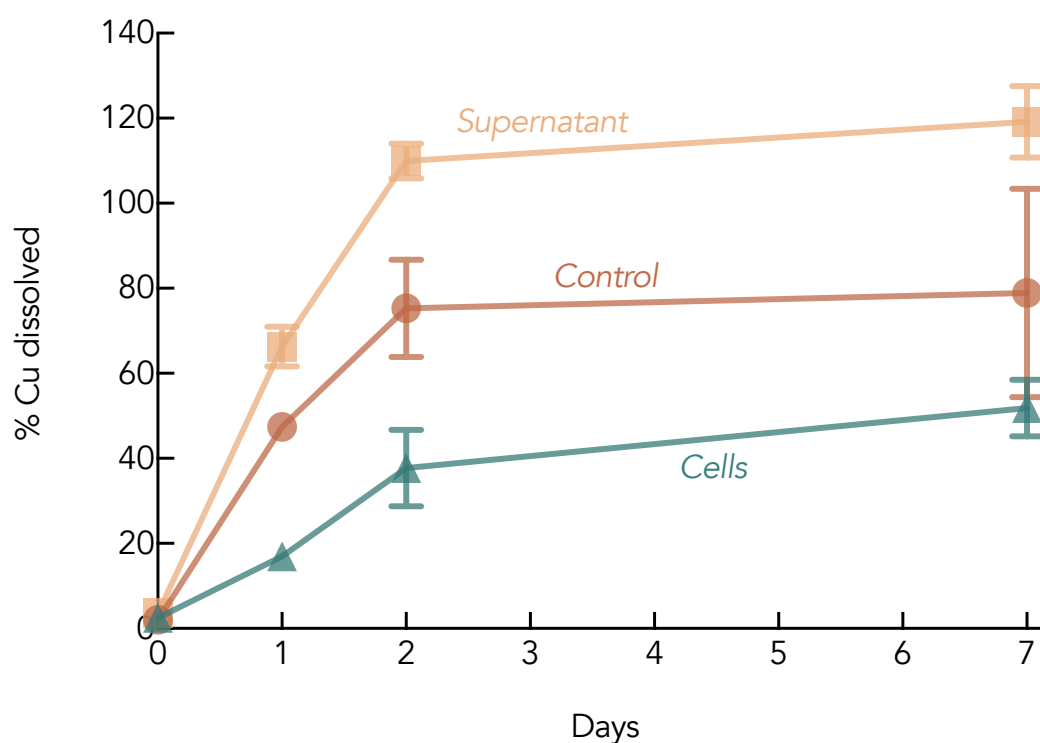


Figure B-3. CuO NP dissolution (%) over time exposed to a culture of *C. violaceum* (green triangles), the supernatant of a culture of *C. violaceum* (beige squares), or in LB media (control, red circles).

For the abiotic dissolution experiments, 7.9 ppm CuO NPs were placed in autoclaved 20 mM ammonium acetate buffer (pH 7) in the presence of either 9.8 ppm NaCN (*NaCN*), 200 μ M HHL signal (*HHL*), or a control (*Control*). NaCN dissolved 100% of the CuO NPs after 4 days. HHL increased CuO NP dissolution compared to the control. The influence of

HHL on CuO NP dissolution might be explained by the observation that HHLs complex Cu^{2+} ions (presented in Chapter 3), driving dissolution.

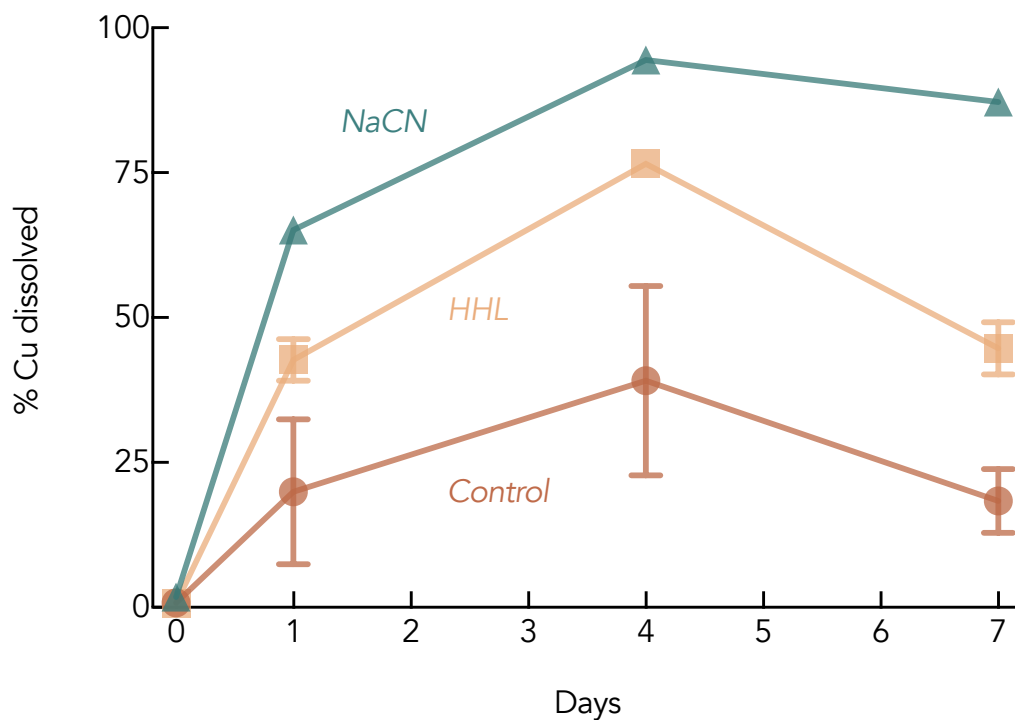


Figure B-4. CuO NP dissolution (%) over time in an abiotic buffer containing HHL (beige squares), NaCN (green triangles), or a control (red circles).

1. Wilhelm, S. *et al.* Analysis of nanoparticle delivery to tumours. *Nat. Rev. Mater.* **1**, 16014 (2016).
2. Rodrigues, S. M. *et al.* Nanotechnology for sustainable food production: promising opportunities and scientific challenges. *Environ. Sci. Nano* **4**, 767–781 (2017).
3. Lofrano, G., Libralato, G. & Brown, J. *Nanotechnologies for Environmental Remediation: Applications and Implications*. (Springer, 2017).
4. Gottschalk, F. & Nowack, B. The release of engineered nanomaterials to the environment. *J. Environ. Monit.* **13**, 1145–55 (2011).
5. Sun, T. Y., Gottschalk, F., Hungerbühler, K. & Nowack, B. Comprehensive probabilistic modelling of environmental emissions of engineered nanomaterials. *Environ. Pollut.* **185**, 69–76 (2014).
6. Sun, T. Y. *et al.* Envisioning Nano Release Dynamics in a Changing World: Using Dynamic Probabilistic Modeling to Assess Future Environmental Emissions of Engineered Nanomaterials. *Environ. Sci. Technol.* **51**, 2854–2863 (2017).
7. Roco, M. C. & Bainbridge, W. S. Societal implications of nanoscience and nanotechnology: Maximizing human benefit. *J. Nanoparticle Res.* **7**, 1–13 (2005).
8. Roco, M. C. Environmentally Responsible Development of Nanotechnology. *Environ. Sci. Technol.* **39**, 106A–112A (2005).
9. Runge, K. K. *et al.* Tweeting nano: How public discourses about nanotechnology develop in social media environments. *J. Nanoparticle Res.* **15**, (2013).
10. Macoubrie, J. Nanotechnology: public concerns, reasoning and trust in government. *Public Underst. Sci.* **15**, 221–241 (2006).
11. Daims, H., Nielsen, J. L., Nielsen, P. H., Schleifer, K. H. & Wagner, M. In Situ Characterization of Nitrospira-Like Nitrite-Oxidizing Bacteria Active in Wastewater Treatment Plants. *Appl. Environ. Microbiol.* **67**, 5273–5284 (2001).
12. Clemente, J. C., Ursell, L. K., Parfrey, L. W. & Knight, R. The impact of the gut microbiota on human health: An integrative view. *Cell* **148**, 1258–1270 (2012).
13. Baek, Y.-W. & An, Y.-J. Microbial toxicity of metal oxide nanoparticles (CuO, NiO, ZnO, and Sb₂O₃) to *Escherichia coli*, *Bacillus subtilis*, and *Streptococcus aureus*. *Sci. Total Environ.* **409**, 1603–8 (2011).
14. Adams, L. K., Lyon, D. Y. & Alvarez, P. J. J. Comparative eco-toxicity of nanoscale TiO₂, SiO₂, and ZnO water suspensions. *Water Res.* **40**, 3527–32 (2006).
15. Wang, J. *et al.* Soft interactions at nanoparticles alter protein function and conformation in a size dependent manner. *Nano Lett.* **11**, 4985–4991 (2011).
16. Neal, A. L. What can be inferred from bacterium-nanoparticle interactions about the potential consequences of environmental exposure to nanoparticles? *Ecotoxicology* **17**, 362–71 (2008).
17. Pelletier, D. A. *et al.* Effects of engineered cerium oxide nanoparticles on bacterial growth and viability. *Appl. Environ. Microbiol.* **76**, 7981–7989 (2010).
18. Poynton, H. C. *et al.* Differential gene expression in daphnia magna suggests distinct modes of action and bioavailability for ZnO nanoparticles and Zn ions. *Environ. Sci. Technol.* **45**, 762–768 (2011).
19. Kumar, A., Pandey, A. K., Singh, S. S., Shanker, R. & Dhawan, A. Engineered ZnO and TiO₂ nanoparticles induce oxidative stress and DNA damage leading to reduced viability of *Escherichia coli*. *Free Radic. Biol. Med.* **51**, 1872–81 (2011).
20. Lowry, G. V., Gregory, K. B., Apte, S. C. & Lead, J. R. Transformations of nanomaterials in the environment. *Environ. Sci. Technol.* **46**, 6893–9 (2012).
21. Simonin, M. & Richaume, A. Impact of engineered nanoparticles on the activity, abundance, and diversity of soil microbial communities: a review. *Environ. Sci. Pollut. Res.* **22**, 13710–13723 (2015).
22. Moore, J. D. *et al.* Impacts of Pristine and Transformed Ag and Cu Engineered

- Nanomaterials on Surficial Sediment Microbial Communities Appear Short-Lived. *Environ. Sci. Technol.* **50**, 2641–2651 (2016).
23. Levard, C., Hotze, E. M., Lowry, G. V & Brown, G. E. Environmental transformations of silver nanoparticles: impact on stability and toxicity. *Environ. Sci. Technol.* **46**, 6900–14 (2012).
 24. Parsek, M. R., Val, D. L., Hanzelka, B. L., Cronan, J. E. & Greenberg, E. P. Acyl homoserine-lactone quorum-sensing signal generation. *Proc. Natl. Acad. Sci. U. S. A.* **96**, 4360–5 (1999).
 25. Surette, M. G., Miller, M. B. & Bassler, B. L. Quorum sensing in *Escherichia coli*, *Salmonella typhimurium*, and *Vibrio harveyi*: a new family of genes responsible for autoinducer production. *Proc. Natl. Acad. Sci. U. S. A.* **96**, 1639–44 (1999).
 26. Bayles, K. W. The biological role of death and lysis in biofilm development. *Nat. Rev. Microbiol.* **5**, 721–6 (2007).
 27. Rice, K. C. & Bayles, K. W. Molecular control of bacterial death and lysis. *Microbiol. Mol. Biol. Rev.* **72**, 85–109, table of contents (2008).
 28. Zemke, A. C. & Bomberger, J. M. Microbiology: Social Suicide for a Good Cause. *Curr. Biol.* **26**, R80–R82 (2016).
 29. González-Pastor, J. E., Hobbs, E. C. & Losick, R. Cannibalism by sporulating bacteria. *Science* **301**, 510–3 (2003).
 30. Lamsa, A., Liu, W.-T., Dorrestein, P. C. & Pogliano, K. The *Bacillus subtilis* cannibalism toxin SDP collapses the proton motive force and induces autolysis. *Mol. Microbiol.* **84**, 486–500 (2012).
 31. Allocati, N., Masulli, M., Di Ilio, C. & De Laurenzi, V. Die for the community: an overview of programmed cell death in bacteria. *Cell Death Dis.* **6**, e1609 (2015).
 32. Lewis, K. Programmed Death in Bacteria Programmed Death in Bacteria. *Microbiol. Mol. Biol. Rev.* **64**, 503–514 (2000).
 33. Fein, J. E. & Rogers, H. J. Autolytic enzyme-deficient mutants of *Bacillus subtilis* 168. *J. Bacteriol.* **127**, 1427–42 (1976).
 34. DeAngelis, K. M., Lindow, S. E. & Firestone, M. K. Bacterial quorum sensing and nitrogen cycling in rhizosphere soil. *FEMS Microbiol. Ecol.* **66**, 197–207 (2008).
 35. Hazan, R. *et al.* Auto Poisoning of the Respiratory Chain by a Quorum-Sensing-Regulated Molecule Favors Biofilm Formation and Antibiotic Tolerance. *Curr. Biol.* **26**, 195–206 (2016).
 36. Hogan, D. a, Vik, A. & Kolter, R. A *Pseudomonas aeruginosa* quorum-sensing molecule influences *Candida albicans* morphology. *Mol. Microbiol.* **54**, 1212–23 (2004).
 37. Bassler, B. L. How bacteria talk to each other: Regulation of gene expression by quorum sensing. *Curr. Opin. Microbiol.* **2**, 582–587 (1999).
 38. McClean, K. H. *et al.* Quorum sensing and *Chromobacterium violaceum*: exploitation of violacein production and inhibition for the detection of N-acylhomoserine lactones. *Microbiology* **143**, 3703–11 (1997).
 39. Gao, J., Ma, A., Zhuang, X. & Zhuang, G. An N-Acyl Homoserine Lactone Synthase in the Ammonia-Oxidizing Bacterium *Nitrosospira multififormis*. *Appl. Environ. Microbiol.* **80**, 951–8 (2014).
 40. Hammer, B. K. & Bassler, B. L. Quorum sensing controls biofilm formation in *Vibrio cholerae*. *Mol. Microbiol.* **50**, 101–104 (2003).
 41. Pessi, G. & Haas, D. Transcriptional control of the hydrogen cyanide biosynthetic genes *hcnABC* by the anaerobic regulator ANR and the quorum-sensing regulators LasR and RhIR in *Pseudomonas aeruginosa*. *J. Bacteriol.* **182**, 6940–6949 (2000).
 42. Stintzi, a, Evans, K., Meyer, J. M. & Poole, K. Quorum-sensing and siderophore biosynthesis in *Pseudomonas aeruginosa*: *lasR/lasI* mutants exhibit reduced pyoverdine biosynthesis. *FEMS Microbiol. Lett.* **166**, 341–345 (1998).
 43. Patterson, A. G. *et al.* Quorum Sensing Controls Adaptive Immunity through the Regulation of Multiple CRISPR-Cas Systems. *Mol. Cell* **64**, 1–7 (2016).
 44. Wei, H. L. & Zhang, L. Q. Quorum-sensing system influences root colonization and biological control ability in *Pseudomonas fluorescens* 2P24. *Antonie van Leeuwenhoek, Int. J. Gen. Mol. Microbiol.* **89**, 267–280 (2006).
 45. Shrout, J. D. & Nerenberg, R. Monitoring bacterial twitter: Does quorum sensing

- determine the behavior of water and wastewater treatment biofilms? *Environmental Science and Technology* **46**, 1995–2005 (2012).
46. Flemming, H. C. Biofouling in water systems - Cases, causes and countermeasures. *Appl. Microbiol. Biotechnol.* **59**, 629–640 (2002).
 47. Suganthan Veerachamy, Tejasri Yarlagadda, Geetha Manivasagam, P. K. Y. Bacterial adherence and biofilm formation on medical implants: A review. *Proc. Inst. Mech. Eng. Part H J. Eng. Med.* **228**, Issue, 1083–1099 (2014).
 48. Kong, K. F., Vuong, C. & Otto, M. Staphylococcus quorum sensing in biofilm formation and infection. *International Journal of Medical Microbiology* **296**, 133–139 (2006).
 49. Singh, P. K. *et al.* Quorum-sensing signals indicate that cystic fibrosis lungs are infected with bacterial biofilms. *Nature* **407**, 762–764 (2000).
 50. Winstanley, C. & Fothergill, J. L. The role of quorum sensing in chronic cystic fibrosis Pseudomonas aeruginosa infections. *FEMS Microbiology Letters* **290**, 1–9 (2009).
 51. Bassler, B. L. & Losick, R. Bacterially Speaking. *Cell* **125**, 237–246 (2006).
 52. Fuqua, C., Parsek, M. R. & Greenberg, E. P. Regulation of gene expression by cell-to-cell communication: acyl-homoserine lactone quorum sensing. *Annu. Rev. Genet.* **35**, 439–68 (2001).
 53. Morohoshi, T., Kato, M., Fukamachi, K., Kato, N. & Ikeda, T. N-acylhomoserine lactone regulates violacein production in Chromobacterium violaceum type strain ATCC 12472. *FEMS Microbiol. Lett.* **279**, 124–30 (2008).
 54. Shaw, P. D. *et al.* Detecting and characterizing N-acyl-homoserine lactone signal molecules by thin-layer chromatography. *Proc. Natl. Acad. Sci. U. S. A.* **94**, 6036–41 (1997).
 55. Kawaguchi, T., Yung, P. C., Norman, R. S. & Decho, A. W. Rapid screening of quorum-sensing signal N-acyl homoserine lactones by an in vitro cell-free assay. *Appl. Environ. Microbiol.* **74**, 3667–3671 (2008).
 56. Li, Z. & Nair, S. K. Quorum sensing: how bacteria can coordinate activity and synchronize their response to external signals? *Protein Sci.* **21**, 1403–17 (2012).
 57. Case, R. J., Labbate, M. & Kjelleberg, S. AHL-driven quorum-sensing circuits: their frequency and function among the Proteobacteria. *ISME J.* **2**, 345–349 (2008).
 58. Stevens, A. M., Dolan, K. M. & Greenberg, E. P. Synergistic binding of the Vibrio fischeri LuxR transcriptional activator domain and RNA polymerase to the lux promoter region. *Proc. Natl. Acad. Sci. U. S. A.* **91**, 12619–12623 (1994).
 59. Swem, L. R. *et al.* A Quorum-Sensing Antagonist Targets Both Membrane-Bound and Cytoplasmic Receptors and Controls Bacterial Pathogenicity. *Mol. Cell* **35**, 143–153 (2009).
 60. Zhang, R. *et al.* Structure of a bacterial quorum-sensing transcription factor complexed with pheromone and DNA. *Nature* **417**, 971–974 (2002).
 61. Lee, J. H., Lequette, Y. & Greenberg, E. P. Activity of purified QscR, a Pseudomonas aeruginosa orphan quorum-sensing transcription factor. *Mol. Microbiol.* **59**, 602–609 (2006).
 62. Von Bodman, S. B., Willey, J. M. & Diggle, S. P. Cell-cell communication in bacteria: United we stand. in *Journal of Bacteriology* **190**, 4377–4391 (2008).
 63. Wang, Y. *et al.* Deleting multiple lytic genes enhances biomass yield and production of recombinant proteins by Bacillus subtilis. *Microb. Cell Fact.* **13**, 129 (2014).
 64. Ferris, F. G., Fyfe, W. S. & Beveridge, T. J. Metallic ion binding by Bacillus subtilis: Implications for the fossilization of microorganisms. *Geology* **16**, 149–152 (1988).
 65. Claverys, J.-P. & Håvarstein, L. S. Cannibalism and fratricide: mechanisms and raisons d'être. *Nat. Rev. Microbiol.* **5**, 219–29 (2007).
 66. Engelberg-Kulka, H. & Hazan, R. Microbiology. Cannibals defy starvation and avoid sporulation. *Science* **301**, 467–8 (2003).
 67. Mascher, T., Margulis, N. G., Wang, T., Ye, R. W. & Helmann, J. D. Cell wall stress responses in Bacillus subtilis: the regulatory network of the bacitracin stimulon. *Mol. Microbiol.* **50**, 1591–1604 (2003).
 68. Boyanov, M. I. *et al.* Adsorption of cadmium to Bacillus subtilis bacterial cell walls: a pH-dependent X-ray absorption fine structure spectroscopy study. *Geochim. Cosmochim. Acta* **67**, 3299–3311 (2003).

69. Kemper, M. A., Urrutia, M. M., Beveridge, T. J., Koch, A. L. & Doyle, R. J. Proton motive force may regulate cell wall-associated enzymes of *Bacillus subtilis*. *J. Bacteriol.* **175**, 5690–5696 (1993).
70. Urrutia Mera, M., Kemper, M., Doyle, R. & Beveridge, T. J. The membrane-induced proton motive force influences the metal binding ability of *Bacillus subtilis* cell walls. *Appl. Environ. Microbiol.* **58**, 3837–3844 (1992).
71. Neuhaus, F. C. & Baddiley, J. A Continuum of Anionic Charge: Structures and Functions of D-Alanyl-Teichoic Acids in Gram-Positive Bacteria. *Microbiol. Mol. Biol. Rev.* **67**, 686–723 (2003).
72. Millward, G. R. & Reaveley, D. A. Electron microscope observations on the cell walls of some gram-positive bacteria. *J. Ultrastruct. Res.* **46**, 309–326 (1974).
73. Jiang, W., Yang, K., Vachet, R. W. & Xing, B. Interaction between oxide nanoparticles and biomolecules of the bacterial cell envelope as examined by infrared spectroscopy. *Langmuir* **26**, 18071–7 (2010).
74. Xu, Z., Liu, X.-W., Ma, Y.-S. & Gao, H.-W. Interaction of nano-TiO₂ with lysozyme: insights into the enzyme toxicity of nanosized particles. *Environ. Sci. Pollut. Res. Int.* **17**, 798–806 (2010).
75. McGivney, E., Han, L., Avellan, A., VanBriesen, J. & Gregory, K. B. Disruption of Autolysis in *Bacillus subtilis* using TiO₂ Nanoparticles. *Sci. Rep.* **7**, 44308 (2017).
76. Kaufmann, G. F. *et al.* Revisiting quorum sensing: Discovery of additional chemical and biological functions for 3-oxo-N-acylhomoserine lactones. *Proc. Natl. Acad. Sci. U. S. A.* **102**, 309–314 (2005).
77. Jolliffe, L. K., Doyle, R. J. & Streips, U. N. The energized membrane and cellular autolysis in *Bacillus subtilis*. *Cell* **25**, 753–763 (1981).
78. Archibald, A. R., Baddiley, J. & Heckels, J. E. Molecular arrangement of teichoic acid in the cell wall of *Staphylococcus lactis*. *Nat. New Biol.* **241**, 29–31 (1973).
79. Doyle, R. J., McDannel, M. L., Helman, J. R. & Streips, U. N. Distribution of teichoic acid in the cell wall of *Bacillus subtilis*. *J. Bacteriol.* **122**, 152–158 (1975).
80. Birdsell, D. C., Doyle, R. J. & Morgenstern, M. Organization of teichoic acid in the cell wall of *Bacillus subtilis*. *J. Bacteriol.* **121**, 726–734 (1975).
81. Wickham, J. R. & Rice, C. V. Solid-state NMR studies of bacterial lipoteichoic acid adsorption on different surfaces. *Solid State Nucl. Magn. Reson.* **34**, 154–61 (2008).
82. Robichaud, C. O., Uyar, A. E., Darby, M. R., Zucker, L. G. & Wiesner, M. R. Estimates of Upper Bounds and Trends in Nano-TiO₂ Production As a Basis for Exposure Assessment. *Environ. Sci. Technol.* **43**, 4227–4233 (2009).
83. Maness, P.-C. *et al.* Bactericidal Activity of Photocatalytic TiO₂ Reaction: toward an Understanding of Its Killing Mechanism. *Appl. Environ. Microbiol.* **65**, 4094–4098 (1999).
84. Metzler, D. M., Li, M., Erdem, A. & Huang, C. P. Responses of algae to photocatalytic nano-TiO₂ particles with an emphasis on the effect of particle size. *Chem. Eng. J.* **170**, 538–546 (2011).
85. Maness, P. C. *et al.* Bactericidal activity of photocatalytic TiO₂ reaction: toward an understanding of its killing mechanism. *Appl. Environ. Microbiol.* **65**, 4094–8 (1999).
86. McGivney, E., Carlsson, M., Gustafsson, J. P. & Gorokhova, E. Effects of UV-C and Vacuum-UV TiO₂ Advanced Oxidation Processes on the Acute Mortality of Microalgae. *Photochem. Photobiol.* **91**, 1142–1149 (2015).
87. Taurozzi, J. S., Hackley, V. a & Wiesner, M. R. Ultrasonic dispersion of nanoparticles for environmental, health and safety assessment--issues and recommendations. *Nanotoxicology* **5**, 711–29 (2011).
88. Sze, A., Erickson, D., Ren, L. & Li, D. Zeta-potential measurement using the Smoluchowski equation and the slope of the current-time relationship in electroosmotic flow. *J. Colloid Interface Sci.* **261**, 402–410 (2003).
89. Salzberg, L. I. & Helmann, J. D. An antibiotic-inducible cell wall-associated protein that protects *Bacillus subtilis* from autolysis. *J. Bacteriol.* **189**, 4671–80 (2007).
90. Falk, S. P., Noah, J. W. & Weisblum, B. Screen for inducers of autolysis in *Bacillus subtilis*. *Antimicrob. Agents Chemother.* **54**, 3723–9 (2010).
91. Wecke, J., Madela, K. & Fischer, W. The absence of D-alanine from lipoteichoic acid and wall teichoic acid alters surface charge, enhances autolysis and increases

- susceptibility to methicillin in *Bacillus subtilis*. *Microbiology* **143**, 2953–2960 (1997).
92. Hamon, M. A. & Lazizzera, B. A. The sporulation transcription factor Spo0A is required for biofilm development in *Bacillus subtilis*. *Mol. Microbiol.* **42**, 1199–1209 (2002).
 93. Msadek, T. When the going gets tough: survival strategies and environmental signaling networks in *Bacillus subtilis*. *Trends Microbiol.* **7**, 201–207 (1999).
 94. Schallmey, M., Singh, A. & Ward, O. P. Developments in the use of *Bacillus* species for industrial production. *Can. J. Microbiol.* **50**, 1–17 (2004).
 95. Breeuwer, P. & Abee, T. in *Molecular Microbial Ecology Manual* (eds. Kowalchuk, G. A., de Bruijn, F. J., Head, I. M., Akkermans, A. D. & van Elsas, J. D.) 3465–3481 (Springer Netherlands, 2004). doi:10.1007/978-1-4020-2177-0
 96. Farha, M. A., Verschoor, C. P., Bowdish, D. & Brown, E. D. Collapsing the proton motive force to identify synergistic combinations against *Staphylococcus aureus*. *Chem. Biol.* **20**, 1168–78 (2013).
 97. Badireddy, A. R., Wiesner, M. R. & Liu, J. Detection, characterization, and abundance of engineered nanoparticles in complex waters by hyperspectral imagery with enhanced Darkfield microscopy. *Environ. Sci. Technol.* **46**, 10081–8 (2012).
 98. Avellan, A. *et al.* Remote biodegradation of Ge-igmogolite nanotubes controlled by the iron homeostasis of *Pseudomonas brassicacearum*. *Environ. Sci. Technol.* **50**, 7791–7798 (2016).
 99. Brown, W. C. Rapid Methods for Extracting Autolysins from *Bacillus subtilis*. *Appl. Environ. Microbiol.* **25**, 295–300 (1973).
 100. Hlady, V., Buijs, J. & Jennissen, H. P. Methods for studying protein adsorption. *Methods Enzymol.* **309**, 402–29 (1999).
 101. Hyyrylainen, H. L. *et al.* D-Alanine substitution of teichoic acids as a modulator of protein folding and stability at the cytoplasmic membrane/cell wall interface of *Bacillus subtilis*. *J. Biol. Chem.* **275**, 26696–703 (2000).
 102. Chambert, R. & Petit-Glatron, M. F. Anionic polymers of *Bacillus subtilis* cell wall modulate the folding rate of secreted proteins. *FEMS Microbiol. Lett.* **179**, 43–7 (1999).
 103. Cedervall, T. *et al.* Understanding the nanoparticle-protein corona using methods to quantify exchange rates and affinities of proteins for nanoparticles. *Proc. Natl. Acad. Sci. U. S. A.* **104**, 2050–5 (2007).
 104. Lundqvist, M., Sethson, I. & Jonsson, B.-H. Protein adsorption onto silica nanoparticles: conformational changes depend on the particles' curvature and the protein stability. *Langmuir* **20**, 10639–47 (2004).
 105. Deng, Z. J., Liang, M., Monteiro, M., Toth, I. & Minchin, R. F. Nanoparticle-induced unfolding of fibrinogen promotes Mac-1 receptor activation and inflammation. *Nat. Nanotechnol.* **6**, 39–44 (2011).
 106. Giacomelli, C. E., Avena, M. J. & De Pauli, C. P. Adsorption of Bovine Serum Albumin onto TiO₂ Particles. *J. Colloid Interface Sci.* **188**, 387–395 (1997).
 107. Etienne Dako, A.-M. B. A. T. D. and C. K. J. *Chemical Biology*. (InTech, 2012). doi:10.5772/2625
 108. Paidhungat, M. & Setlow, P. Role of Ger Proteins in Nutrient and Nonnutrient Triggering of Spore Germination in *Bacillus subtilis*. *J. Bacteriol.* **182**, 2513–2519 (2000).
 109. Driks, A. Overview: development in bacteria: spore formation in *Bacillus subtilis*. *Cell. Mol. Life Sci.* **59**, 389–391 (2002).
 110. Young, F. E. Autolytic enzyme associated with cell walls of *Bacillus subtilis*. *J. Biol. Chem.* **241**, 3462–7 (1966).
 111. Engelberg-Kulka, H., Amitai, S., Kolodkin-Gal, I. & Hazan, R. Bacterial programmed cell death and multicellular behavior in bacteria. *PLoS Genet.* **2**, e135 (2006).
 112. Yamamoto, H., Kurosawa, S. -i. & Sekiguchi, J. Localization of the Vegetative Cell Wall Hydrolases LytC, LytE, and LytF on the *Bacillus subtilis* Cell Surface and Stability of These Enzymes to Cell Wall-Bound or Extracellular Proteases. *J. Bacteriol.* **185**, 6666–6677 (2003).
 113. Blackman, S. A., Smith, T. J. & Foster, S. J. The role of autolysins during vegetative growth of *Bacillus subtilis* 168. *Microbiology* **144** (Pt 1, 73–82 (1998).

114. Zhu, J. *et al.* Quorum-sensing regulators control virulence gene expression in *Vibrio cholerae*. *Proc. Natl. Acad. Sci. U. S. A.* **99**, 3129–34 (2002).
115. Fuqua, C. & Greenberg, E. P. Listening in on bacteria: acyl-homoserine lactone signalling. *Nat. Rev. Mol. cell Biol.* **3**, 685–695 (2002).
116. Decho, A. W., Frey, R. L. & Ferry, J. L. Chemical challenges to bacterial AHL signaling in the environment. *Chem. Rev.* **111**, 86–99 (2011).
117. Whiteley, M., Diggle, S. P. & Greenberg, E. P. Progress in and promise of bacterial quorum sensing research. *Nature* **551**, 313–320 (2017).
118. Frommberger, M. *et al.* Analysis of N-acylhomoserine lactones after alkaline hydrolysis and anion-exchange solid-phase extraction by capillary zone electrophoresis-mass spectrometry. *Electrophoresis* **26**, 1523–1532 (2005).
119. Liu, P., Chen, X. & Chen, W. Adsorption of N-acyl-Homoserine Lactone onto Colloidal Minerals Presents Potential Challenges for Quorum Sensing in the Soil Environment. *Geomicrobiol. J.* **32**, 602–608 (2015).
120. Dong, Y. H. *et al.* Quenching quorum-sensing-dependent bacterial infection by an N-acyl homoserine lactonase. *Nature* **411**, 813–7 (2001).
121. Borchardt, S. A. *et al.* Reaction of acylated homoserine lactone bacterial signaling molecules with oxidized halogen antimicrobials. *Appl. Environ. Microbiol.* **67**, 3174–3179 (2001).
122. Cui, Y., Frey, R. L., Ferry, J. L. & Ferguson, P. L. Identification of hydroxyl radical oxidation products of N-hexanoyl-homoserine lactone by reversed-phase high-performance liquid chromatography coupled with electrospray ionization tandem mass spectrometry. *Rapid Commun Mass Spectrom* **23**, 1212–1220 (2009).
123. Wang, Y. *et al.* The influence of soil heavy metals pollution on soil microbial biomass, enzyme activity, and community composition near a copper smelter. *Ecotoxicol. Environ. Saf.* **67**, 75–81 (2007).
124. Grass, G., Rensing, C. & Solioz, M. Metallic copper as an antimicrobial surface. *Appl. Environ. Microbiol.* **77**, 1541–1547 (2011).
125. Rhoads, W. J., Pruden, A. & Edwards, M. A. Interactive Effects of Corrosion, Copper, and Chloramines on *Legionella* and *Mycobacteria* in Hot Water Plumbing. *Environ. Sci. Technol.* **51**, 7065–7075 (2017).
126. Miller, K. P. *et al.* Engineering nanoparticles to silence bacterial communication. *Front. Microbiol.* **6**, 189 (2015).
127. Mohanty, A., Tan, C. H. & Cao, B. Impacts of nanomaterials on bacterial quorum sensing: differential effects on different signals. *Environ. Sci. Nano* **3**, 351–356 (2016).
128. Singh, B. R. *et al.* Mycofabricated biosilver nanoparticles interrupt *Pseudomonas aeruginosa* quorum sensing systems. *Sci. Rep.* **5**, 13719 (2015).
129. Naik, K. & Kowshik, M. Anti-quorum sensing activity of AgCl-TiO₂ nanoparticles with potential use as active food packaging material. *J. Appl. Microbiol.* **117**, 972–983 (2014).
130. Yang, Y. & Alvarez, P. J. J. Sublethal Concentrations of Silver Nanoparticles Stimulate Biofilm Development. *Environ. Sci. Technol. Lett.* **2**, 221–226 (2015).
131. Xiao, X. *et al.* Impairment of Biofilm Formation by TiO₂ Photocatalysis through Quorum Quenching. *Environ. Sci. Technol.* **50**, 11895–11902 (2016).
132. Kamnev, A. A. *et al.* Cobalt(II) complexation with small biomolecules as studied by 57 Co emission Mossbauer spectroscopy. *Spectrochim. Acta - Part A Mol. Biomol. Spectrosc.* **172**, 77–82 (2015).
133. Lansdown, A. Silver in Health Care: Antimicrobial Effects and Safety in Use. *Curr. Probl. Dermatol.* **33**, 17–34 (2006).
134. Gustafsson, J. P. Visual MINTEQ. (2014).
135. Frisch, M. J. *et al.* Gaussian 03. (2004).
136. Martinelli, D., Grossmann, G., Séquin, U., Brandl, H. & Bachofen, R. Effects of natural and chemically synthesized furanones on quorum sensing in *Chromobacterium violaceum*. *BMC Microbiol.* **4**, 25 (2004).
137. Franski, R. Electrospray ionization mass spectrometric study of 1,3,4-oxadiazole–copper complexes. *J. Mass Spectrom.* **39**, 272–276 (2004).
138. Di Marco, V. B. & Bombi, G. G. Electrospray mass spectrometry (ESI-MS) in the study of metal-ligand solution equilibria. *Mass Spectrom. Rev.* **25**, 347–379 (2006).

139. Gianelli, L., Amendola, V., Fabbrizzi, L., Pallavicini, P. & Mellerio, G. G. Investigation of reduction of Cu(II) complexes in positive-ion mode electrospray mass spectrometry. *Rapid Commun. Mass Spectrom.* **15**, 2347–2353 (2001).
140. Schobert, R. & Schlenk, A. Tetramic and tetronic acids: An update on new derivatives and biological aspects. *Bioorganic and Medicinal Chemistry* **16**, 4203–4221 (2008).
141. Hawver, L. A., Jung, S. A. & Ng, W. L. Specificity and complexity in bacterial quorum-sensing systems. *FEMS Microbiol. Rev.* **40**, 738–752 (2016).
142. Braud, A., Geoffroy, V., Hoegy, F., Mislin, G. & Schalk, I. Presence of the siderophores pyoverdine and pyochelin in the extracellular medium reduces toxic metal accumulation in *Pseudomonas aeruginosa* and increases bacterial metal tolerance. *Environ. Microbiol. Rep.* **2**, (2010).
143. Hoshino, T. & Yamamoto, M. Conversion from Tryptophan Precursor into Violacein Pigments by a Cell-free System from *Chromobacterium violaceum*. *Biosci. Biotechnol. Biochem.* **61**, 2134–2136 (1997).
144. Duran, N., Antonio, R. V., Haun, M. & Pilli, R. A. Biosynthesis of a trypanocide by *Chromobacterium violaceum*. *World J. Microbiol. Biotechnol.* **10**, 686–690 (1994).
145. Ahmad, W. A., Yusof, N. Z., Nordin, N., Zakaria, Z. A. & Rezali, M. F. Production and characterization of violacein by locally isolated *chromobacterium violaceum* grown in agricultural wastes. *Appl. Biochem. Biotechnol.* **167**, 1220–1234 (2012).
146. Glišić, B. Đ. *et al.* Copper(II) complexes with aromatic nitrogen-containing heterocycles as effective inhibitors of quorum sensing activity in *Pseudomonas aeruginosa*. *RSC Adv.* **6**, 86695–86709 (2016).
147. Käkinen, A., Bondarenko, O., Ivask, A. & Kahru, A. The effect of composition of different ecotoxicological test media on free and bioavailable copper from CuSO₄ and CuO nanoparticles: Comparative evidence from a Cu-selective electrode and a Cu-biosensor. *Sensors* **11**, 10502–10521 (2011).
148. Lambert, R. J. . & Pearson, J. Susceptibility testing : accurate and reproducible minimum inhibitory concentration (MIC) and non-inhibitory concentration (NIC) values. *J. Appl. Microbiol.* **88**, 784–790 (2000).
149. Misra, S. K., Dybowska, A., Berhanu, D., Luoma, S. N. & Valsami-Jones, E. The complexity of nanoparticle dissolution and its importance in nanotoxicological studies. *Sci. Total Environ.* **438**, 225–232 (2012).
150. Iavicoli, I., Leso, V., Beezhold, D. H. & Shvedova, A. A. Nanotechnology in agriculture: Opportunities, toxicological implications, and occupational risks. *Toxicol. Appl. Pharmacol.* (2017).
151. Gao, X. & Lowry, G. V. Progress towards standardized and validated characterizations for measuring physicochemical properties of manufactured nanomaterials relevant to nano health and safety risks. *NanoImpact* (2017).
152. Markus, A. A., Parsons, J. R., Roex, E. W. M., de Voogt, P. & Laane, R. W. P. M. Modelling the Release, Transport and Fate of Engineered Nanoparticles in the Aquatic Environment—A Review. (2017).
153. Ferry, J. L. *et al.* Transfer of gold nanoparticles from the water column to the estuarine food web. *Nat. Nanotechnol.* **4**, 441–444 (2009).
154. Burns, J. M. *et al.* Surface charge controls the fate of Au nanorods in saline estuaries. *Environ. Sci. Technol.* **47**, 12844–12851 (2013).
155. Glenn, J. B. & Klaine, S. J. Abiotic and biotic factors that influence the bioavailability of gold nanoparticles to aquatic macrophytes. *Environ. Sci. Technol.* **47**, 10223–30 (2013).
156. Glenn, J. B., White, S. A. & Klaine, S. J. Interactions of gold nanoparticles with freshwater aquatic macrophytes are size and species dependent. *Environ. Toxicol. Chem.* **31**, 194–201 (2012).
157. Thwala, M., Klaine, S. J. & Musee, N. Interactions of metal-based engineered nanoparticles with aquatic higher plants: A review of the state of current knowledge. *Environ. Toxicol. Chem.* **35**, 1677–1694 (2016).
158. Wray, A. T. & Klaine, S. J. Modeling the influence of physicochemical properties on gold nanoparticle uptake and elimination by *Daphnia magna*. *Environ. Toxicol. Chem.* **34**, 860–872 (2015).
159. Lohse, S. E. *et al.* Nanomaterial Probes in the Environment: Gold Nanoparticle Soil

- Retention and Environmental Stability as a Function of Surface Chemistry. *ACS Sustain. Chem. Eng.* *accsuschemeng.7b02622* (2017). doi:10.1021/acssuschemeng.7b02622
160. Li, T. *et al.* Comparative toxicity study of Ag, Au, and Ag-Au bimetallic nanoparticles on *Daphnia magna*. *Anal. Bioanal. Chem.* **398**, 689–700 (2010).
 161. Mahapatra, I. *et al.* Probabilistic modelling of prospective environmental concentrations of gold nanoparticles from medical applications as a basis for risk assessment. *J. Nanobiotechnology* **13**, 93 (2015).
 162. Wadsworth, M. E., Zhu, X., Thompson, J. S. & Pereira, C. J. Gold dissolution and activation in cyanide solution: Kinetics and mechanism. *Hydrometallurgy* **57**, 1–11 (2000).
 163. Bek, R. Y., Kosolapov, G. V & Shuraeva, L. I. Anodic Dissolution of Gold in Cyanide Solutions : Effect of Temperature. *Russ. J. Electrochem.* **37**, 256–260 (2001).
 164. Dzombak, D. A., Ghosh, R. S. & Wong-Chong, G. M. *Cyanide in Water and Soil: Chemistry, Risk, and Management*. (CRC Press, 2005). doi:10.1002/9781118618974
 165. McCarthy, A. J., Coleman, R. G. & J., N. M. The Mechanism of the Oxidative Dissolution of Colloidal Gold in Cyanide Media. *J. Electrochem. Soc.* **145**, 408 (1998).
 166. Jana, N. R., Gearheart, L., Obare, S. O. & Murphy, C. J. Anisotropic chemical reactivity of gold spheroids and nanorods. *Langmuir* **18**, 922–927 (2002).
 167. Vennesland, B., Pistorius, E. K. & Gewitz, H. S. *HCN production by microalgae*. (1981).
 168. Knowles, C. J. Microorganisms and cyanide. *Bacteriol. Rev.* **40**, 652–680 (1976).
 169. Blom, D., Fabbri, C., Eberl, L. & Weisskopf, L. Volatile-mediated killing of *Arabidopsis thaliana* by bacteria is mainly due to hydrogen cyanide. *Appl. Environ. Microbiol.* **77**, 1000–1008 (2011).
 170. Lee, J. H. *et al.* Nematicidal activity of a nonpathogenic biocontrol bacterium, *Pseudomonas chlororaphis* O6. *Curr. Microbiol.* **62**, 746–751 (2011).
 171. Spence, C. *et al.* Natural rice rhizospheric microbes suppress rice blast infections. *BMC Plant Biol.* **14**, 130 (2014).
 172. Karthikeyan, O. P., Rajasekar, A. & Balasubramanian, R. Bio-oxidation and biocyanidation of refractory mineral ores for gold extraction: A review. *Critical Reviews in Environmental Science and Technology* **45**, 1611–1643 (2015).
 173. Tay, S. B. *et al.* Enhancing gold recovery from electronic waste via lixiviant metabolic engineering in *Chromobacterium violaceum*. *Sci. Rep.* **3**, 2236 (2013).
 174. Zdor, R. E. Bacterial cyanogenesis: Impact on biotic interactions. *J. Appl. Microbiol.* **118**, 267–274 (2015).
 175. Ryall, B., Lee, X., Zlosnik, J. E. A., Hoshino, S. & Williams, H. D. Bacteria of the *Burkholderia cepacia* complex are cyanogenic under biofilm and colonial growth conditions. *BMC Microbiol.* **8**, 108 (2008).
 176. Vencalek, B. E. *et al.* In Situ Measurement of CuO and Cu (OH) 2 Nanoparticle Dissolution Rates in Quiescent Freshwater Mesocosms. *Environ. Sci. Technol. Lett.* **3**, 375–380 (2016).
 177. Ma, R. *et al.* Size-controlled dissolution of organic-coated silver nanoparticles. *Env. Sci Technol* **46**, 752–759 (2011).
 178. Bian, S.-W. W., Mudunkotuwa, I. A., Rupasinghe, T. & Grassian, V. H. Aggregation and dissolution of 4 nm ZnO nanoparticles in aqueous environments: influence of pH, ionic strength, size, and adsorption of humic acid. *Langmuir* **27**, 6059–6068 (2011).
 179. McShane, H. V. A., Sunahara, G. I., Whalen, J. K. & Hendershot, W. H. Differences in soil solution chemistry between soils amended with nanosized CuO or Cu reference materials: implications for nanotoxicity tests. *Env. Sci Technol* **48**, 8135–8142 (2014).
 180. Gao, X., Spielman-Sun, E., Rodrigues, S. M., Casman, E. A. & Lowry, G. V. Time and nanoparticle concentration affect the extractability of Cu from CuO NP amended soil. *Environ. Sci. Technol.* **51**, 2226–2234 (2017).
 181. Judy, J. D., Unrine, J. M., Rao, W., Wirick, S. & Bertsch, P. M. Bioavailability of gold nanomaterials to plants: Importance of particle size and surface coating. *Environ. Sci. Technol.* **46**, 8467–8474 (2012).
 182. Zhai, G., Walters, K. S., Peate, D. W., Alvarez, P. J. J. & Schnoor, J. L. Transport of

- Gold Nanoparticles through Plasmodesmata and Precipitation of Gold Ions in Woody Poplar. *Environ. Sci. Technol. Lett.* **1**, 146–151 (2014).
183. Zhu, Z.-J. *et al.* Effect of Surface Charge on the Uptake and Distribution of Gold Nanoparticles in Four Plant Species. *Environ. Sci. Technol.* **46**, 12391–12398 (2012).
 184. Taylor, A. F., Rylott, E. L., Anderson, C. W. N. & Bruce, N. C. Investigating the toxicity, uptake, nanoparticle formation and genetic response of plants to gold. *PLoS One* **9**, (2014).
 185. Campbell, S. C., Olson, G. J., Clark, T. R. & McFeters, G. Biogenic production of cyanide and its application to gold recovery. *J. Ind. Microbiol. Biotechnol.* **26**, 134–139 (2001).
 186. Turkevich, J., Stevenson, P. C. & Hillier, J. A study of the nucleation and growth processes in the synthesis of colloidal gold. *Discuss. Faraday Soc.* **11**, 55–75 (1951).
 187. Michaels, R., Hankes, L. V. & Corpe, W. A. Cyanide formation from glycine by nonproliferating cells of *Chromobacterium violaceum*. *Arch. Biochem. Biophys.* **111**, 121–125 (1965).
 188. Kothari, V., Sharma, S. & Padia, D. Recent research advances on *Chromobacterium violaceum*. *Asian Pacific Journal of Tropical Medicine* (2017). doi:10.1016/j.apjtm.2017.07.022
 189. Rao, C. R. M., Sahuquillo, A. & Lopez Sanchez, J. F. A Review of the Different Methods Applied in Environmental Geochemistry For Single and Sequential Extraction of Trace Elements in Soils and Related Materials. *Water. Air. Soil Pollut.* **189**, 291–333 (2008).
 190. Kashem, M. A., Singh, B. R., Kondo, T., Imamul Huq, S. M. & Kawai, S. Comparison of extractability of Cd, Cu, Pb and Zn with sequential extraction in contaminated and non-contaminated soils. *Int. J. Environ. Sci. Tech* **4**, 169–176 (2007).
 191. Minakata, K., Nozawa, H., Gonmori, K., Suzuki, M. & Suzuki, O. Determination of cyanide, in urine and gastric content, by electrospray ionization tandem mass spectrometry after direct flow injection of dicyanogold. *Anal. Chim. Acta* **651**, 81–84 (2009).
 192. Glenn, J. B. & Klaine, S. J. Abiotic and Biotic Factors That Influence the Bioavailability of Gold Nanoparticles to Aquatic Macrophytes. *Environ. Sci. Technol.* 130828135943006 (2013). doi:10.1021/es4020508
 193. Robinson, M. E. Cyanogenesis in Plants. *Biol. Rev.* **5**, 126–141 (1930).
 194. Xing, B., Vecitis, C. D. & Senesi, N. *Engineered Nanoparticles and the Environment: Biophysicochemical Processes and Toxicity. Engineered Nanoparticles and the Environment: Biophysicochemical Processes and Toxicity* (2016). doi:10.1002/9781119275855
 195. Youn, W. *et al.* Cytoprotective Encapsulation of Individual Jurkat T Cells within Durable TiO₂ Shells for T-Cell Therapy. *Angew. Chemie - Int. Ed.* **56**, 10702–10706 (2017).
 196. Palmqvist, N. G. M., Bejai, S., Meijer, J., Seisenbaeva, G. A. & Kessler, V. G. Nanotitania aided clustering and adhesion of beneficial bacteria to plant roots to enhance crop growth and stress management. *Sci. Rep.* **5**, 10146 (2015).
 197. Palmqvist, N. G. M. Nanoparticles: Case studies of their synthesis, properties and biological interaction. (Swedish University of Agricultural Sciences, 2017).
 198. Rajkumar, M., Ae, N., Prasad, M. N. V. & Freitas, H. Potential of siderophore-producing bacteria for improving heavy metal phytoextraction. *Trends Biotechnol.* **28**, 142–149 (2010).
 199. Aouada, F. A. & de Moura, M. R. in *Nanotechnologies in Food and Agriculture* 103–118 (Springer, 2015).
 200. Wagh Nee Jagtap, M. S. *et al.* Evaluation of anti-quorum sensing activity of silver nanowires. *Appl. Microbiol. Biotechnol.* **97**, 3593–601 (2013).
 201. Islam, M. F., Rojas, E., Bergey, D. M., Johnson, A. T. & Yodh, A. G. High Weight Fraction Surfactant Solubilization of Single-Wall Carbon Nanotubes in Water. *Nano Lett.* **3**, 269–273 (2003).
 202. Guardia, P. *et al.* Surfactant effects in magnetite nanoparticles of controlled size. *J. Magn. Magn. Mater.* **316**, e756–e759 (2007).
 203. Dutta, D. *et al.* Adsorbed proteins influence the biological activity and molecular

- targeting of nanomaterials. *Toxicol. Sci.* **100**, 303–15 (2007).
204. Cherukuri, P. *et al.* Mammalian pharmacokinetics of carbon nanotubes using intrinsic near-infrared fluorescence. *Proc. Natl. Acad. Sci. U. S. A.* **103**, 18882–6 (2006).
 205. Liz-Marzan, L. M. & Lado-Tourin, I. Reduction and Stabilization of Silver Nanoparticles in Ethanol by Nonionic Surfactants. **7463**, 3585–3589 (1996).
 206. Mukherji, R. *et al.* Selective imaging of quorum sensing receptors in bacteria using fluorescent au nanocluster probes surface functionalized with signal molecules. *ACS Appl. Mater. Interfaces* **5**, 13076–81 (2013).
 207. Hunter, T. N., Wanless, E. J., Jameson, G. J. & Pugh, R. J. Non-ionic surfactant interactions with hydrophobic nanoparticles: Impact on foam stability. *Colloids Surfaces A Physicochem. Eng. Asp.* **347**, 81–89 (2009).
 208. Zhang, L., He, R. & Gu, H.-C. Oleic acid coating on the monodisperse magnetite nanoparticles. *Appl. Surf. Sci.* **253**, 2611–2617 (2006).
 209. Min, Y., Akbulut, M., Kristiansen, K., Golan, Y. & Israelachvili, J. The role of interparticle and external forces in nanoparticle assembly. *Nat. Mater.* **7**, 527–38 (2008).
 210. Götz, C. *et al.* Uptake, degradation and chiral discrimination of N-acyl-D/L-homoserine lactones by barley (*Hordeum vulgare*) and yam bean (*Pachyrhizus erosus*) plants. *Anal. Bioanal. Chem.* **389**, 1447–1457 (2007).
 211. Luanpitpong, S. *et al.* Induction of cancer-associated fibroblast-like cells by carbon nanotubes dictates its tumorigenicity. *Sci. Rep.* **6**, 39558 (2016).
 212. Wang, X. *et al.* Pluronic F108 coating decreases the lung fibrosis potential of multiwall carbon nanotubes by reducing lysosomal injury. *Nano Lett.* **12**, 3050–3061 (2012).
 213. Aldieri, E. *et al.* The role of iron impurities in the toxic effects exerted by short multiwalled carbon nanotubes (MWCNT) in murine alveolar macrophages. *J. Toxicol. Environ. Heal. - Part A Curr. Issues* **76**, 1056–1071 (2013).
 214. Kim, I. H., Kim, K. & Rhee, S. G. Induction of an antioxidant protein of *Saccharomyces cerevisiae* by O₂, Fe³⁺, or 2-mercaptoethanol. *Proc. Natl. Acad. Sci. U. S. A.* **86**, 6018–22 (1989).
 215. Spielman-Sun, E. *et al.* Impact of surface charge on cerium oxide nanoparticle uptake and translocation by wheat (*Triticum aestivum*). *Environ. Sci. Technol.* [acs.est.7b00813](https://doi.org/10.1021/acs.est.7b00813) (2017). doi:10.1021/acs.est.7b00813
 216. Sperling RA, Gil PR, Zhang F, Zanella M, P. W. Biological Applications of Gold Nanoparticles. *Chem. Soc. Rev.* **37**, 1896–1908 (2008).
 217. Tegenaw, A. *et al.* Characterization and potential environmental implications of select Cu-based fungicides and bactericides employed in U.S. markets. *Env. Sci Technol* **49**, 1294–1302 (2015).
 218. Liu, R. & Lal, R. Potentials of engineered nanoparticles as fertilizers for increasing agronomic productions. *Sci. Total Environ.* **514**, 131–139 (2015).
 219. Elmer, W. H. & White, J. C. The use of metallic oxide nanoparticles to enhance growth of tomatoes and eggplants in disease infested soil or soilless medium. *Environ. Sci. Nano* **3**, 1072–1079 (2016).
 220. Liu, R. & Lal, R. Potentials of engineered nanoparticles as fertilizers for increasing agronomic productions. *Sci Total Env.* **514**, 131–139 (2015).
 221. Sekine, R. *et al.* Aging of Dissolved Copper and Copper-based Nanoparticles in Five Different Soils: Short-term Kinetics vs. Long-term Fate. *J. Environ. Qual.* (2017).
 222. Cornu, J. Y. *et al.* Contrasting effects of pyoverdine on the phytoextraction of Cu and Cd in a calcareous soil. *Chemosphere* **103**, 212–219 (2014).
 223. Menzies, N. W., Donn, M. J. & Kopittke, P. M. Evaluation of extractants for estimation of the phytoavailable trace metals in soils. *Environ. Pollut.* **145**, 121–130 (2007).
 224. Bravin, M. N., Le Merrer, B., Denaix, L., Schneider, A. & Hinsinger, P. Copper uptake kinetics in hydroponically-grown durum wheat (*Triticum turgidum durum* L.) as compared with soil's ability to supply copper. *Plant Soil* **331**, 91–104 (2010).
 225. Ponizovsky, A. A., Allen, H. E. & Ackerman, A. J. Copper activity in soil solutions of calcareous soils. *Environ. Pollut.* **145**, 1–6 (2007).
 226. Maynard, A. D. Don't define nanomaterials. *Nature* **475**, 31 (2011).